THE UNIVERSITY OF CHICAGO

GEOMETRY OF COLLOIDAL MATERIALS

A DISSERTATION SUBMITTED TO
THE FACULTY OF THE DIVISION OF THE PHYSICAL SCIENCES
IN CANDIDACY FOR THE DEGREE OF
DOCTOR OF PHILOSOPHY

DEPARTMENT OF PHYSICS

BY
VISHAL HASMUKH SONI

CHICAGO, ILLINOIS
MARCH 2019

To my parents.

TABLE OF CONTENTS

LIST OF FIGURES

ACKNOWLEDGMENTS

I spent the last 8 years studying systems of microscopic particles whose behaviors can seem erratic and without clear direction when observed at the wrong scales. When you zoom out, though, in time and space, something different always emerges. You start to see patterns and remarkable collective behavior. Something about this process drew me to this research, and brought me to the University of Chicago to study soft matter, and I think it all started with my family.

Describing my family as erratic is probably an understatement. It's hard for me to think about my mom's trajectory through life without having to pause in awe. Every step she's taken seems to be wrapped up in a kind of courage that I don't think I've seen matched in anyone else I've ever encountered. That courage brought her to this country when she was only 19, and, together with my father, she started a chain of seemingly random processes that, over the course of 40 years, built up an entire world for me and my siblings to come up in. There's no way we would have become who we became if they hadn't channeled such an insane energy into building that world.

Their courage and deeply unconventional nature is especially embedded into who my sister became. I've watched her change her path in life, both personally and in her career, too many times to count. That's always been an inspiration for me in how I moved through the world. It's exactly what drew me to the type of personalities have aggregated at the University of Chicago. The careers of two of those personalities that I've admired since I was in undergrad, Sid Nagel and Tom Witten, convinced me that the Chicago was the right place for me. When I got my acceptance, I knew immediately that I would go there to study soft condensed matter. Still, I had no idea I would end up working in the lab I ended up choosing. When William sent me an email asking me to consider his group, though, and sent pictures of a lab that was completely empty, for some reason I was sold.

I started in his lab the summer before my first quarter. During that summer, I moved in with my best friend and brother, Vimal, and we shared a home for the first several years

of my PhD. I don't think I would have been able to adjust so seamlessly without him, and I'm extremely grateful for those years. We would start every morning together, and I'd take him to work before heading into the basement of GCIS.

In that basement, I met some of the strangest and most influential people of my life. I'm going to tell you about some of those people, and there's no more natural person to start with than Martin. There's no one I met in my visiting weekend that stood out more than Martin. When I learned that he accepted Chicago, and eventually joined our lab, I was relieved that I'd be able to share the office with someone who was simultaneously so down to earth and so odd. I'm certain that the office would have turned out a lot more boring if our two personalities weren't paired inside of it.

Another personality undeniably shaped the culture of our office was Dustin, who, along with William, was really our scientific co-parent. I think it's really lucky we had someone like him as a co-parent. He really taught us how to think creatively to get an experiment to work and he played his part in keeping the office interesting as well.

If there was anyone who tried to take on the job of curbing the insanity of our office, it was Noah. If you spend a little time learning about his strange and interesting path through life, though, you quickly realize he isn't cut out for that job. It's hard to imagine how the office would have turned out without his balance.

One of my favorite pastimes, when I'm bored with distracting people in our office, is to go to distract people in our second office. The person whose attention I most enjoyed stealing was Hridesh, who would become like a brother to me. I'm lucky to have had Hridesh to lend an ear when I needed to talk about some of the hardest times I went through in grad school, both in my academic and personal life. I'm grateful to still have conversations with him that wander around for hours to this day.

Over the course of my PhD, people flowed in and out of that other office. There are a few people that flowed in who I really need to thank. The first is Lisa, who brought a new perspective to the lab that I really admired. It's what drew me into becoming such good

friends with her over the years. I'm really really happy that our friendship is still growing to this day. I can't begin to explain how grateful I am for all of her support.

Two special people that flowed in after Lisa are Sofia and Stephane. Sofia was my partner in crime in the study of chiral fluids. We've been through so many stressful nights, and I'm happy we both made it out alive. I'm grateful for her patience, especially with me. It's something I really tried to learn from. Stephane joined around the same time as Sofia, and he brought a new type of emphasis on community to the lab. He really helped elevate the fun we had.

Sadly, the other office, doesn't have many occupants as I'm writing this, but I'm glad Takumi is holding down the fort. From managing last minute birthday planning, to last minute group meeting changes, he's proven to be a really reliable and caring friend.

I've seen so many iterations of the group over the years, and I really am grateful that it evolved the way it did. Just as Martin, Lisa, and Hridesh were leaving, Bob joined the lab. I'm really happy that happened because, him being my age and also from Illinois, it's been really helpful to have someone that could relate to parts of my background that no one else could. We've become great friends outside the lab, and I know we'll continue to be.

I'm also grateful to have had Jiayi flow through our lab. Even though our backgrounds are very different, I often also feel that she could relate to parts of me that other people couldn't. For as long as she's been in our lab, I knew she was smart, strange, and hilarious. I honestly never expected, though, that she would end up influencing my thinking as much as she did in my final months. I'm truly thankful to have her as a friend.

Over the years, I really do feel lucky to have had the privilege to have hilarious and interesting conversations everywhere I turned in that basement, even with undergrads, like Watee, Sophie, and Sattvic. It's interesting to go on this transitional period at the same time as Sattvic, who is currently deciding on grad schools. I know we'll both stay in touch after we leave the lab.

These interesting conversations continue outside our lab, all throughout the JFI. It's been

really great to be a part of the soft matter community at Chicago. There have been too many interesting people that I'm glad to have interacted with to list them all, but I'll name a few: Yifan Wang, Thomas Videbaek, Kieran Murphy, Endao Han, Nick Schade, Nidhi Pashine, Michelle Driscoll, Ivo Peters, Ed Barry, Daniel Hexner, Arvind Murugan, Heinrich Jaeger, and Suri Vaikuntanathan. I want to give a special thank you to Jelani, who gave me little treats just when I needed them the most. I'm grateful for all the friends I've met all over the physics department, too, especially Mark and Gautam. I'd also like to thank Yau Wah, who always let me know he was available to talk.

All the work in this thesis could not have been possible without William and all of my collaborators, who really deserve a special thanks. William was the crucial ingredient in all of the projects I've worked on. I especially admire how he channeled so many different talents, including his own, into sculpting our work on chiral fluids. Observing him over the last 8 years has deeply shaped the kind of scientist I've become. He's also played a crucial role in developing our interesting lab traditions. In addition to William, I want to specially thank Leo Gomez, Stefano Sacanna, and Denis Bartolo.

It seems appropriate to end on one collaborator in particular: Ephraim. As I put this thesis together, Ephraim not only helped me by hearing my thoughts and providing edits, but he stayed up at night with me and kept my spirits up. I'll never forget that. I'm glad that he is going to be the one that carries on my work in the lab. He has a perfect balance of my skills, while minimizing my flaws. What makes me most sure, though, that he's going to a do a great job, oddly enough, is that he has a great sense of humor.

ABSTRACT

Geometry has become a primary language for physicists to describe condensed matter, stemming from our natural inclination to think visually. The development of colloidal model systems has created new possibilities for visualizing complex geometries and dynamics in a vast range of material phases. In this thesis, we will use colloidal model systems and geometry as tools for making sense of the underlying physics of material phases.

We begin by investigating the use of geometry for guiding the assembly of shaped colloids interacting with depletion forces. Here the shape of the colloids, called superballs, interpolate between two familiar forms: spheres and cubes. We find an interplay between depletant size and colloid shape determines the assembly. In one regime of depletant size, we observe the transition from hexagonal to rhombic crystals consistent with the densest packings. As we tune the size, however, the particles assemble into square lattice structures instead of such dense packings. We explain the assembly with simple geometric considerations. By using a mixture of depletants, one of which is size tunable, we then induce solid-to-solid phase transitions between these phases. Our results introduce a general scenario where particle building blocks are designed to assemble not only into their maximum density states, but also into depletion-tunable interaction-dependent structures.

We then move to investigate the influence of crystal assembly from the geometry not of the particles themselves, but of the underlying environment. In particular, we immerse interacting particles which would otherwise form a perfect crystal into spatially varying potentials, where they arrange into fascinating distorted structures. Using colloidal experiments and molecular dynamics simulations, we show the external fields have the effect of placing the lattice on a surface with Gaussian curvature, in which it is structurally frustrated. Using this curvature, we are able to predict the distribution of topological defects that emerge to resolve this frustration. Our results show that when repulsive particles are confined by external fields, topological defects are an almost inevitable feature of the ground state.

Finally, we establish a new material by driving the individual component building blocks.

We achieve this by spinning a system of colloidal magnets in an external magnetic field, forming a cohesive material that behaves like a liquid. Here, we utilize the geometry of the fluid at large, namely the shape of its surface. By understanding how this surface evolves in time, we are able to unlock the physics of the underlying flows. We find that the driving of the particles results in the breaking of time-reversal and parity symmetries, giving way to the emergence of two key features. The first is an odd stress which drives driving uni-directional surface waves and instabilities, with no counterpart in conventional fluids. The second is an anomalous transport coefficient known as odd (or Hall) viscosity, an experimentally long sought property of chiral fluids.

CHAPTER 1

INTRODUCTION

Euclid, often referred to as the "founder of geometry" [1], began his study of the subject while developing a propositional framework for understanding the physics of light in the 3rd century BC. Since that time, the histories of physics and geometry have been inextricably intertwined. Their co-development has progressed from Euclid's original axioms and postulates, through the establishment of differential geometry and classical mechanics, and into the modern era. Given this relationship, geometry has evidently proven to be a natural language through which humans understand the physical world. It is no surprise then, that many of the most significant advances of modern physics can be attributed to deeply geometric insights. Famously, for instance, our current understanding of the universe at astronomical scales is largely indebted to the formulation of a geometric picture of gravity.

For condensed matter physics, the transformative impact of geometric insights is perhaps most apparent in the realization that the properties of many materials, such as crystals, amorphous solids, and liquid crystals, could be understood by visualizing the geometric arrangement of their building blocks [2, 3]. As early as the beginning of the 17th century, it was hypothesized that the symmetric patterns of snowflakes stemmed from the packing of spherical water particles [4]. By the beginning of the 20th century, the advent of x-ray diffraction allowed physicists, for the first time, to peer into structure of crystals at the smallest length scales, allowing the visualization of ordered geometric arrangements of atoms and molecules [5].

Using x-ray diffraction, it was soon shown that the same arrangements could emerge from the self assembly of "atomic" components that were not atoms or molecules, but objects on the scale of a micron, as is the case in opals [6] and aggregated viruses [7]. These observations laid the groundwork for studying the formation of these geometries in general, with appropriate scaling, at larger scales and with simpler instruments. Among the earliest influential examples were the studies of Bragg and Nye, in which millimeter-scale bubble

rafts were used as a model for investigating the dynamics of closed-pack crystals [8]. While the geometric arrangements of large collections of particles can be difficult to conceptualize without visualization, studying their physics adds an extra layer of complexity, as one needs to understand how structural elements may evolve in time. Using a table top experiment, however, the scientists were able to visualize complex dynamics, such as the motion of crystal dislocations, which were at the time inaccessible through other methods. For a condensed matter experimentalist, the natural inclination to think visually and geometrically is the core appeal of using such model systems.

1.1 Colloids as model systems

The spirit of the experiments of Bragg and Nye lived on into the later part of the twentieth century, where advances in chemical synthesis brought upon the development of new model "atoms": colloidal particles. A colloid is a mixture in which particles of one substance are suspended throughout a medium made of another substance. Throughout this thesis, the medium will be liquid, and the particles, themselves often referred to as "colloids," will be solid. These colloids are separated by several orders of magnitude in scale from both bubble rafts and actual atoms. This size range, on the order of a micrometer, is crucial as the particles are often large enough to be observed with a basic optical microscope. They are small enough, however, to undergo Brownian motion [9, 10], endowing them with a thermal energy and driving them to constantly explore vast configuration spaces. By controlling the chemistry of the particles, or simply by modifying the fluid in which they are suspended, inter-particle interactions can easily be tuned in relation to this thermal energy. As a result, a mixture of billions of colloids can readily form a system that can not only mimic the structure of crystalline materials, but be used to explore the complex phase spaces in both ordered and disordered systems, as well as transitions between phases [11, 12, 13, 14, 15, 16, 17].

In recent decades, advances in colloidal synthesis [18, 19], together with innovations in methods for manipulating and visualizing these microscopic particles [20, 21, 22, 23, 24], have

given rise to exciting studies on the assembly and dynamics of condensed matter systems. More recently, these studies have expanded to the exploration of so-called active and driven systems, where the colloidal building blocks are no longer stationary, but are injected with energy. Such systems give rise to the exploration of new and inherently dynamic collective states [25, 26, 27, 28].

1.2 Overview of this thesis

In this thesis, we utilize colloidal model systems as tool to visualize and understand the geometric principles that underly the physics of novel materials. We begin by exploring the connection between particle geometry and the assembly and structure of matter. Assembly mechanisms which rely on geometric aspects of the system, in this case the shape of the constituent particles, often lead to more robust ways of influencing a material structure because they are independent of the chemical details. A simple, but familiar example of this connection comes from dense packings, such as spheres arranged in a face-centered cubic lattice. Such arrangements are perhaps the most commonly studied in colloidal model systems. Here, we will explore the effects of perturbing away from this familiar shape, using using micron sized 'superballs', shapes which interpolate between spheres and cubes. The thermal fluctuations inherent in colloidal systems gives rise to entropic forces, which we use to guide these particles into lattices that can be predicted using the particles' shapes.

The underlying physics of a material can be influenced not only by the geometry of the particles, but by their underlying environment, for example through the curvature of the landscape on which they assemble. In many cases, however, the geometry of the underlying environment is not as readily apparent as in the shape of the substrate. An example of such a situation is investigated in chapter 3, where we explore the 2-D assembly of repulsive spheres inside spatially varying external fields. We see a that non-trivial inherent geometry emerges as a result of the interplay between the inter-particle interactions and the external confinement fields. In this case, we will see that geometry can play a role in disrupting

symmetry in a material through the excitation of topological defects.

In the final part of the thesis, we present a system whose components are no longer passive, but are driven out of equilibrium. By driving magnetically interacting particles to spin, we will form an 'odd' material known as a chiral fluid. The result of driving the individual particles is not only to create interesting particle-level dynamics, but to evolve the overall geometry of the material, namely the shape of its boundary. By studying these surface dynamics, we infer the interesting hydrodynamics in the fluid. In simple fluids, such as water, invariance under parity and time-reversal symmetry imposes that the rotation of constituent 'atoms' is determined by the flow and that viscous stresses damp motion. However, activation of the rotational degrees of freedom of a fluid by spinning its atomic building blocks breaks these constraints and drives lively surface dynamics. We leverage the fact that a single image – the power spectrum – encodes the key features of these dynamics, and we use it to reveal the presence of Hall viscosity, an experimentally long sought property of chiral fluids.

CHAPTER 2

SHAPE-SENSITIVE ASSEMBLY OF COLLOIDAL SUPERBALLS

Guiding the self-assembly of materials by controlling the shape of the individual particle constituents is a powerful approach to material design. In this chapter, we explore how colloidal silica superballs crystallize into canted phases in the presence of depletants. Some of these phases are consistent with the so-called 'Λ_1' lattice that was recently predicted as the densest packings of superdisks. As the size of the depletant is reduced, however, we observe a transition to a square phase. The differences in these entropically-stabilized phases result from an interplay between the size of the depletants and the fine structure of the superball shape. We find qualitative agreement of our experimental results both with a phase diagram computed on the basis of the volume accessible to the depletants and with simulations. By using a mixture of depletants, one of which is thermo-sensitive, we induce solid-to-solid phase transitions between square and canted structures. Depletant size is utilized to leverage the shapes of particles in driving their self-assembly, demonstrating a general and powerful mechanism for engineering novel materials.

2.1 Introduction

Determining the relationship between the macroscopic structure of a material and the properties of its microscopic constituents is a fundamental problem in condensed matter science. A particularly interesting aspect of this problem is to understand how the self-assembly of a collection of particles is determined by their shape. These so-called 'packing problems' have long interested physicists, mathematicians, and chemists alike and have been used to understand the structures of many condensed phases of matter [29, 2, 30]. Computational and experimental advances continue to enable new explorations into fundamental aspects of these problems today [31, 32, 33, 34, 35, 36, 37, 38, 39, 40]. Recent discoveries include dense

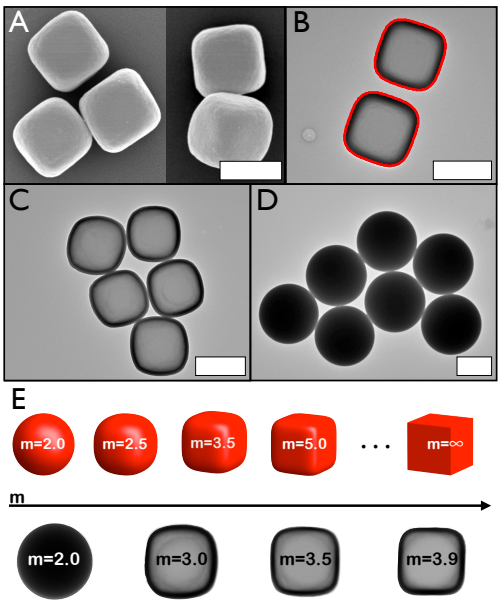

Figure 2.1: (a) SEM images of sample $m = 3.9$. The particles have a cubic shape with rounded edges. (b-d) TEM micrographs of samples with $m = 3.5$, $m = 3.0$ and $m = 2.0$, respectively. All samples are uniform with a size polydispersity as low as 3%. Scale bars: 1 μm for all panels. In (b) the particles are shown with their corresponding superball fit highlighted in red. (e) computer generated models of colloidal superballs with different shape parameters m. A gradual increase of the absolute value of the shape parameter from $m = 2$ (spheres) results in a gradual alteration of the particle shape to resemble more cube-like particles. TEM images of silica superballs with different m-values are shown at the bottom of the panel.

packings of tetrahedra into disordered, crystalline, and quasi-crystalline structures [41, 42], as well as the singular dense packings of ellipsoids [43].

Technologically speaking, these discoveries are becoming increasingly crucial as new synthesis techniques are allowing for the creation of more and more complex shaped nanoscopic and microscopic particles [18, 19]. The self-assembly of these particles into ordered structures creates new possibilities for the fabrication of novel materials [44, 45, 46, 47, 48]. Moreover, advances in synthesis techniques have created new capabilities for experimentally investigating how the shapes of particles can be exploited in their self-assembly [49, 50, 51].

Here, we experimentally and computationally explore the self-assembly of colloidal superballs interacting with depletion forces. We find that monolayers of superballs can be tuned to equilibrate into both their densest known packings–so called 'Λ_0' and 'Λ_1' lattices [39]–as

well as into less dense structures of different symmetries depending on an interplay between the subtle features of the particle shapes and the size of the depletants.

2.2 Colloidal Superballs

The family of superballs can smoothly interpolate shapes between spheres and cubes (see Fig. 2.1e), and are modeled as:

$$(x)^m + (y)^m + (z)^m \leq 1, \tag{2.1}$$

where m is the shape parameter. For $m = 2$, this parametrization describes a purely isotropic sphere. As m is increased, the shape increasingly resembles a cube, as shown in Fig. 2.1. The amorphous colloidal superballs were prepared via controlled deposition of silica on the surface of hematite templates, using a synthetic technique [52] that yields high amounts of monodisperse (3% polydispersity) particles. Each batch of particles, which were made from the same initial hematite cores, contains superballs of comparable sizes ($\sim$ 1.3 μm), but differing shape parameters as a result of differing amounts of silica precipitated on the surface. The size and shape of superballs were analyzed using Scanning (SEM) and Transmission Electron Microscopy (TEM) micrographs (Fig. 2.1). Analyzing the particle shape from TEM images, we find agreement between the contour of the particle and the superball shape as shown in Figure 2.1b, in which the red contours correspond to the superball fits.

To determine the parameters that uniquely characterize the shape of our synthetic particles, we took as a starting point transmission electron microscopy (TEM) images, such as the ones shown in Figure 2.1b-c. We then used a standard algorithm to find the edges of the particle, and subsequently fitted the edges with equation:

$$\left(\frac{x}{a}\right)^m + \left(\frac{y}{b}\right)^m = 1, \tag{2.2}$$

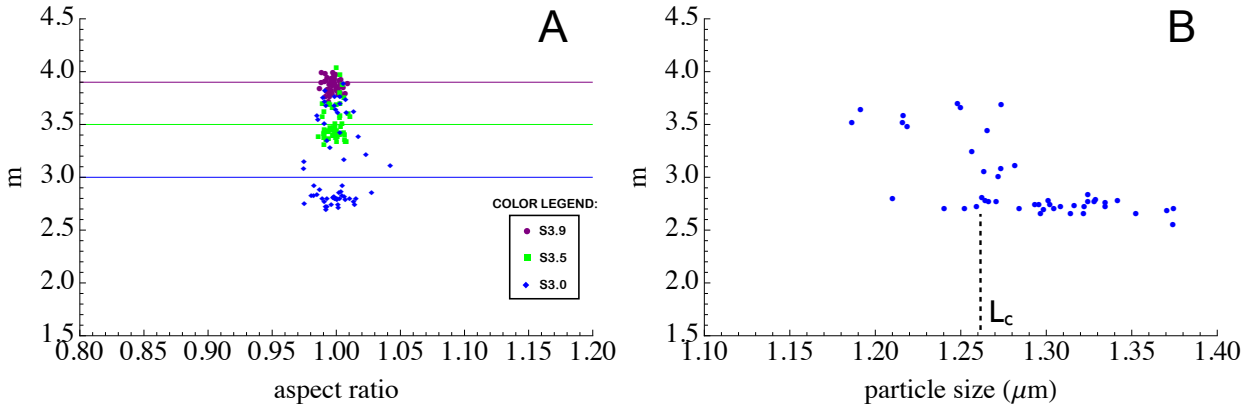

Figure 2.2: (a) The points of this graph represent the shape parameters m of the silica superballs measured by fitting the shape of 80-100 particles. Different colors correspond to different samples as indicated in the color legend. The average values are indicated with the horizontal lines interpolating the y-axis in their corresponding mean values. (b) For sample S3.0 the shape parameter (m) of the particle is plotted against the particle size (L). A sharp transition is visible around a critical value $L_c = 1.26\ \mu m$ which shows a rapid decay in shape polydispersity after the transition.

where a and b are the semi-axes of the particles. This equation differs from Equation 2.1 because the analysis is done on TEM images, which are essentially two-dimensional projections of the superballs and also because the equation should account for deviations in the particle aspect ratio (a/b) that, by definition, is 1 for a superball. A typical fit is shown in Figure 2.1b while a plot of the results obtained by fitting an ensemble of images (about 100 fits) for different m values is shown in Figure 2.2. The average value of m obtained for each superball sample can therefore be used to characterize the roundness of the shape and consequently how much the shape deviates from the cubic shape.

The dense cloud of data for the superballs with highest m (sample S3.9, purple points in Figure 2.2) indicates that particles are highly monodisperse in shape. The data spread out more for decreasing shape parameter, which is apparently related to the (still poorly understood) mechanism of silica growth on a superball surface. The plot in Figure 2.2b exhibits for sample S3.0 a curious relation between particle size and shape. The graph shows that for small particle size the sample is monodisperse in shape until a critical particle length is reached (L_c, in this case corresponding to 1.26 μm) at which the shape polydispersity

increases. Upon further silica growth beyond the critical length, the shape becomes again monodisperse. The nature of this growth behavior remains to be clarified; the important point here is that despite the polydispersity of samples S3.0 and S3.5, the average position of the data points in Figure 2.2 clearly demonstrates that the various superball samples have significantly different average shape parameters.

Fig. 2.1 shows SEM and TEM images of the silica superballs used for the experiments. Although the particles still possess a distinct cubic symmetry, they have rounded edges whose curvatures are consistent with superballs of shape parameters $m = 2.0$, $m = 3.0$, $m = 3.5$, and $m = 3.9$. The spherical particles with shape parameters $m = 2$ were purchased from Bangs Laboratories. Inc.

2.3 Shape-driven colloidal superball phases

To perform the experiments, silica superballs were dispersed in slightly alkaline water (pH = 9) and were stabilized against aggregation by surface charges. Sodium chloride (10 mM, final concentration) was added to the dispersion to screen the charges and lower the Debye length down to a thickness of about 3 nm, small enough to allow the particles to fully experience their anisotropic shape. Attractive forces between superballs arise by addition of depletion agents with gyration radii of $R_g = 57$ nm, 65 nm, 70 nm, 210 nm, 228 nm, and 329 nm. Flat optical capillaries were filled with aqueous mixtures of superballs and depletants and were monitored in time with bright-field microscopy.

At low particle concentration, the superballs first sediment to the bottom of the capillary where they feel attracted to the glass wall by depletion forces. While diffusing in the plane, the particles cluster together into monolayers. The samples were allowed to equilibrate for about 20 minutes before time lapsed images are collected. The images show the appearance of several qualitatively distinct phases (Figure 2.3). The particles are found to arrange into crystallite islands, often possessing grain boundaries, which we separate by orientation and analyze independently. We do not exclude a priori the possibility that a cluster does not

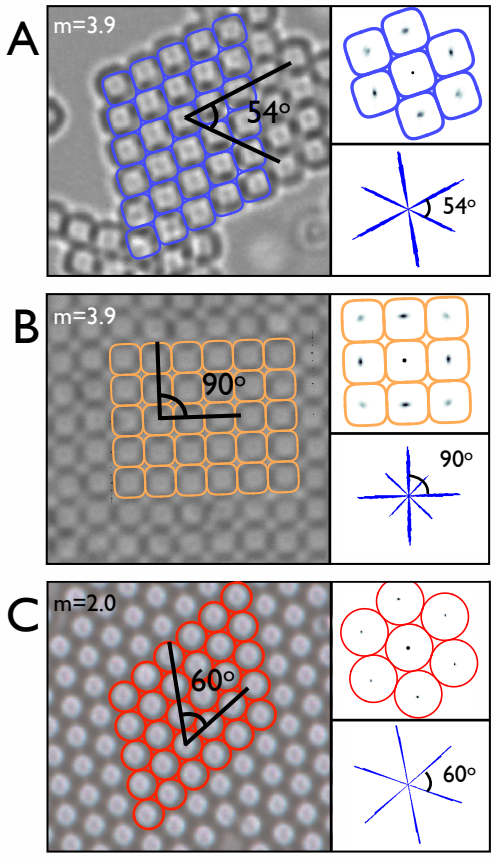

Figure 2.3: Representative optical microscope images showing three different ordered structures found in superball samples. To the right of each image is a histogram of the relative positions of nearest neighbors for each particle in a crystallite (top) and a histogram of the inter particle bond angles (bottom). The structures of the crystallites are characterized by bond angels of 54° (a), 90° (b), and 60° (c). Note that the superballs in (a) and (b) have the same shape. The different lattice structures in these two samples result from different depletant sizes.

have a coherent crystal structure.

To characterize the structure of each cluster, the positions of the constituent particles are identified for every time lapsed image. The particles are identified using an algorithm based on circular Hough transforms. After identifying the positions, we cluster the particles and separate the clusters based on their apparent orientation. For each particle within a cluster, we compute the angles between adjacent nearest-neighbor bonds. An ensemble of bond-angles are collected over time and over each particle within a cluster. The bond angle distributions are used to identify which of the lattice type of interest are statistically

most similar to the experimental structures. This is accomplished by comparing the resulting distributions to the values of the bond angles expected for the square, Λ_0, and Λ_1 lattices for the particular value of m. Figure 2.4a shows the distribution of bond angles for experimental data corresponding to a variety of shape parameters. For experiments characterized by broad distributions of bond angles (see Fig. 2.4c-d), a clear identification may not be possible.

The relative positions of nearest neighbors are then computed for each particle. For spherical superballs the distribution of these positions are found to be consistent with triangular lattices (Fig. 2.3c). For superballs with intermediate shape parameters ($2 < m < \infty$), however, the behavior becomes more interesting. Experimentally, we observe that the particles often form canted structures (Fig. 2.3a) characterized by inter-particle bond angles distinct from 60°, indicative of triangular lattices, and 90°, which are characteristic of square lattices. Recently, the densest packings of superdisks with these intermediate shape parameters were predicted to fall into two families of lattices, referred to as Λ_0 and Λ_1 packings [39]. Testing the distribution of relative nearest neighbor positions in the experiment for consistency with the lattice vectors of these structures confirms, for the first time, the observation of an equilibrium Λ_1 lattice of superballs in experiments (see Fig. 2.3). We also find that, for superballs with these same intermediate shape parameters ($m = 3.5$ and $m = 3.9$), the equilibrium structure transitions to a square lattice as the depletant size is decreased, suggesting that the resulting phases are determined by an interplay between the shape of the particle and the size ratio $q = 2R_g/L$ between the depletant and the superball.

To understand this interplay, we look at the depletion interactions between the superballs. Each superball is surrounded by an exclusion zone of thickness R_g that is unavailable for the centers of the depletants to occupy. Superball configurations which minimize the volume excluded from the depletants by overlapping exclusion zones increase the overall entropy of the system.

In order to understand the favorability of the three lattices for a given choice of parameters, we compute the free energy of a depletion-stabilized bound state of a particle for each

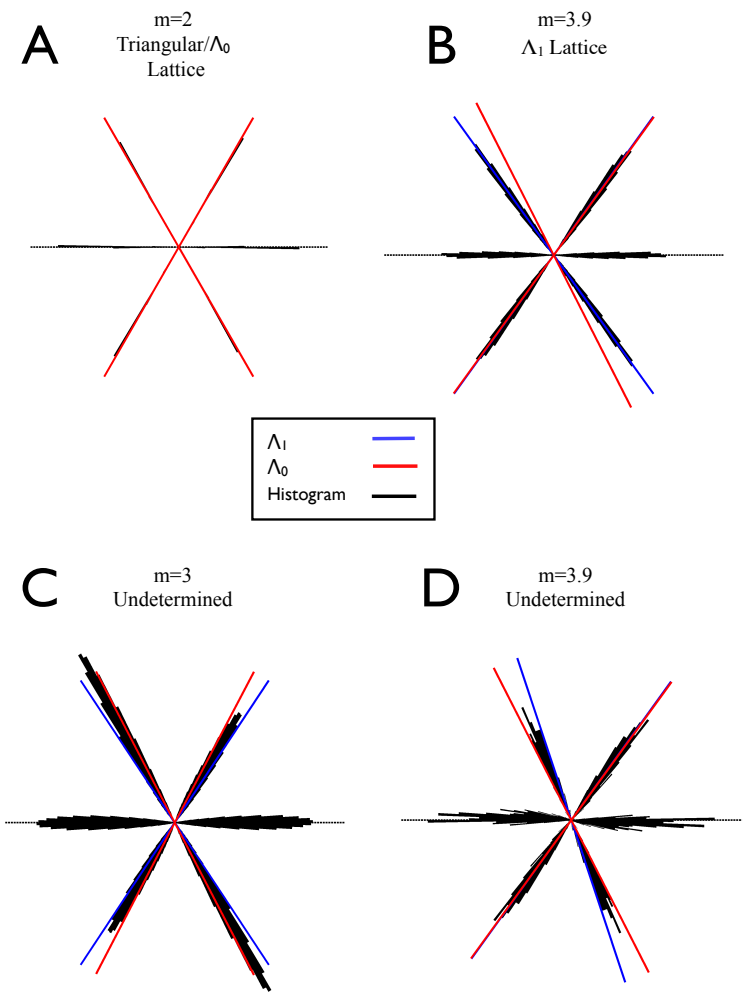

Figure 2.4: Angular histograms of experimental data. (a) Angular histograms for spherical particles show sharp peaks indicating 60 degree bondangles between particles, as expected for a triangular lattice, which is consistent with both the Λ_0 and Λ_1 lattices for $m = 2$. (b) Example angular histogram from which a Λ_1 lattice is identified. (c) and (d) show examples of distributions in which a clear identification is not possible.

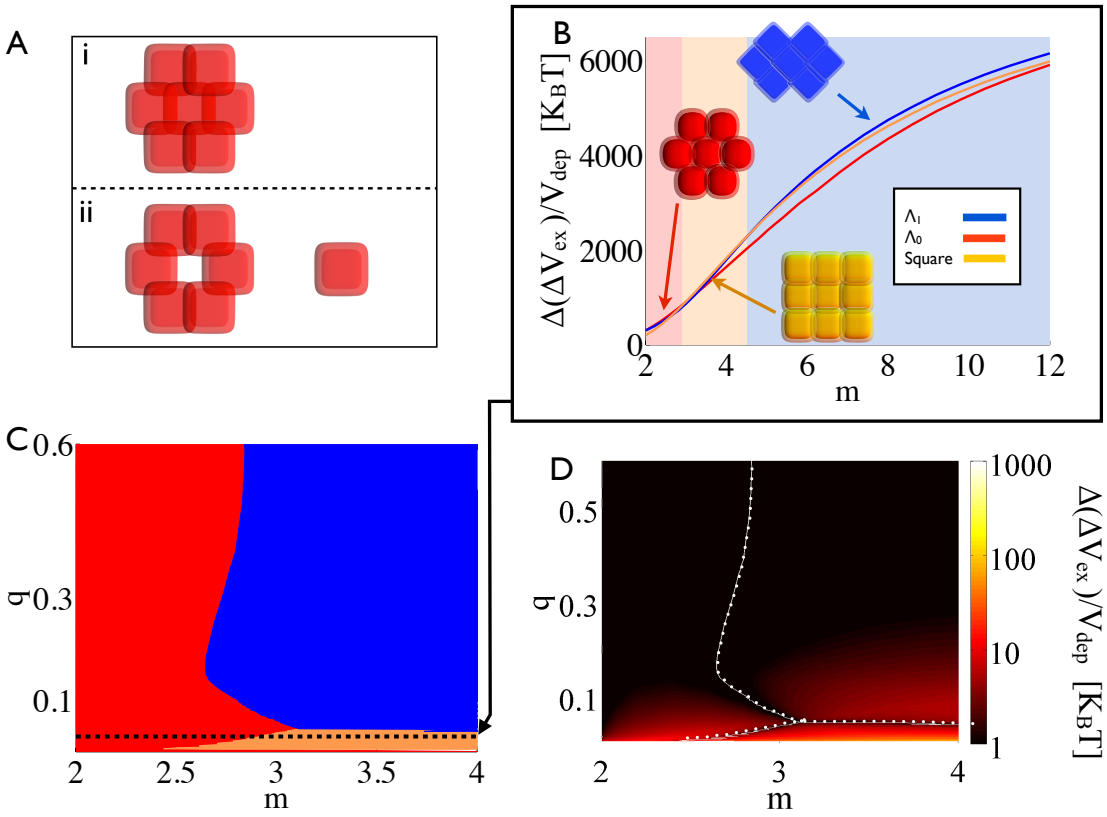

Figure 2.5: Two dimensional predicted diagram for depletion stabilized superball phases. The favorability of each lattice type is determined by calculating the bound state energy of a particle. (a) Operationally, the bound state energy is found by computing the difference in the excluded volume for a particular lattice (i) and the excluded volume of that lattice when a particle is removed from the interior (ii). (b) Change in excluded volume for each lattice type with varying m but fixed q. To illustrate the behavior of ΔV_{ex}, the range of m used in this plot is larger than the experimentally investigated range. Background color indicates the preferred phase. (c) Two dimensional phase diagram for experimental range of q and m. (d) Difference in ΔV_{ex} between two most favorable lattice types. Near phase boundaries, the phases become degenerate. In addition, for large depletants, the benefit of choosing a particular phase is small. Recent molecular dynamics simulations [39] of convex superdisks have shown that the critical value of m when the densest packings change from Λ_1 to Λ_0 is at $m \approx 2.572$.

crystal type. For a number density n of depletants, this energy is given by $U = -nK_BT\Delta V_{ex}$, where ΔV_{ex} is the change in volume excluded when a particle is removed from the interior of an otherwise filled lattice. This volume change is computed by first constructing a finely pixelated binary image of an arrangement of filled outlines of superballs of length $L + R_g$ placed at the lattice sites corresponding to square, Λ_0, and Λ_1 lattices for fixed L and shape parameter m. Similar images are produced corresponding to the same arrangement with one particle removed from the interior of the lattice. ΔV_{ex} is computed by subtracting the total number of nonzero pixels for the full lattice by the lattice with one particle missing, and then subsequently subtracting the number of nonzero pixels for an isolated superball of length $L + R_g$.

By computing and comparing ΔV_{ex} for the Λ_0, Λ_1, and square lattices, we estimate which lattice is energetically favorable for a particular value of m (Figure 2.6a,c). We note that in this model, the magnitude of ΔV_{ex}, and thus the overall bound state energy, will generally scale with R_g. We also note that this model neglects the entropy of the superballs. It has been suggested that the role of rotational entropy of the particles can be significant in stabilizing canted phases [50], though the relative importance of this effect is debated [40]. Figure 2.5b shows that, for fixed-sized depletants and superballs, ΔV_{ex} varies smoothly for each lattice type as m is varied. For a particular combination of m and q, the lattice with the highest value of ΔV_{ex} represents the preferred phase. Using this principle, a two-dimensional phase diagram is approximated in Figure 2.5c. The interplay between the particle shape and the size ratio q suggested by this diagram is qualitatively apparent in the experimentally realized structures (Fig. 2.7).

In order to quantify how energetically favorable a particular lattice is for a particular m and q, we also compute the difference in energy between the two lattices that have the lowest values. This difference characterizes the energetic benefit of choosing one particular lattice. When the difference is zero, the most favorable lattices becomes degenerate.

To compare the energetics in different regions of the phase diagram, however, a consis-

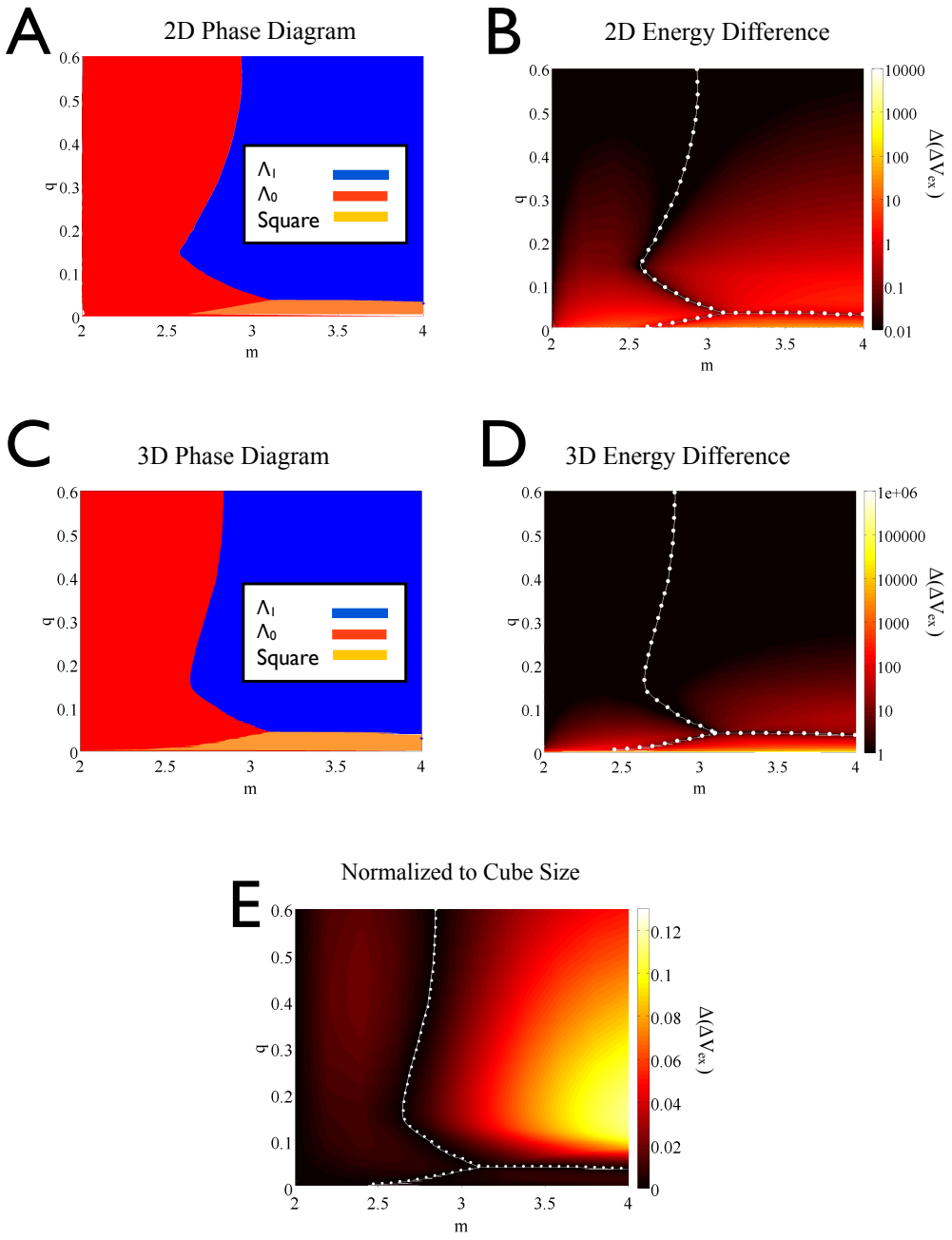

Figure 2.6: Phase diagrams and energetic characterization of superball lattices. (a) The phase diagram of two dimensional superdisks is computed by computing ΔV_{ex} of each lattice type for each value of m and q. (b) The energetic benefit of choosing a particular lattice type for two dimensional superdisks is computed for each m and q by finding the difference the energy of the two most energetically favorable lattices. (c) and (d) Phase diagram for 3D superballs arranged in two dimensional lattices. The structure of the diagrams are qualitatively similar to the 2D diagrams. (e) The energy difference between the two most favorable lattices computed using a constant number density of depletants.

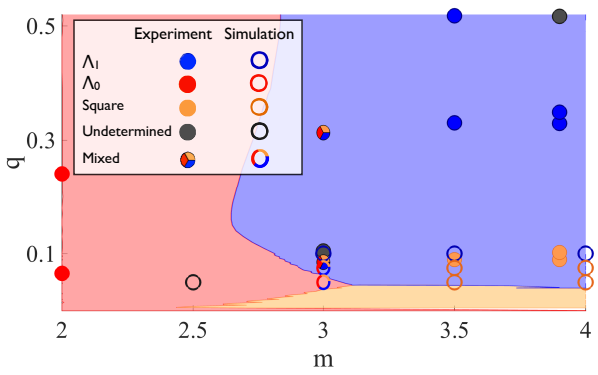

Figure 2.7: Comparison between experimental observations, bulk crystal simulations, and calculated phase diagram for superballs at different m and q values. Circles indicate the experimental results, hollow circles indicate simulation results, while the background color indicates the predicted phase. The approximated phase diagram qualitatively agrees with our experimental and simulation results.

tent definition of the number density of depletants n must to be used. Figure 2.6e shows the diagram computed using a constant depletant density between experiments. In our experiments, the depletant concentration is typically on the order of C^*, where C^* is maximum density in which the depletants can maintain their radius of gyration. We thus use $n \propto \frac{1}{V_{dep}}$ where V_{dep} is the volume of the depletant. Figures 2.6b,d show the resulting diagram, which corresponds to normalizing the difference in ΔV_{ex} by the volume of the depletant. We note that this simple model neglects to account for the rotational and vibrational entropy of the superballs.

Figures 2.6c-d correspond to diagrams computed for 2D arrangements of 3D superballs. The complementary diagrams for purely 2D superdisks is shown in Figure 2.6 a and b. The qualitative similarity reflects the *quasi*-2D nature of the system.

Indeed, the calculations agree with the experimental result that for sufficiently small depletants and sufficiently large m, square lattices, though they are not the densest packings for any finite value of m, are preferred. Square lattices occur when m is large enough such that the overlap in exclusion zones resulting from face-to-face contact is considerable and for q small enough such that depletants are able to fit into the inter-particle pores made where the rounded edges of the superballs meet. When the osmotic pressure exerted by a

depletant within an inter particle pore is substantial, the cubic phase is stabilized. However, when intermediate-sized depletants, which can no longer fit into the spaces within the lattice, are dispersed with superballs possessing these larger values of m (3.5 and 3.9), the densely-packed Λ_1 phase emerges. As the size ratio gets larger, we notice the distribution of bond angles within a crystallite begin to broaden. In the case of $m = 3.9$, for the highest size ratio q we tested, the distribution was too broad to identify the experimental structure with one of the three lattices, leaving the structure undetermined. While our calculations suggest that the Λ_1 phase is energetically favorable, Figure 2.5d shows that the difference in ΔV_{ex} between the lattices with the two highest values becomes negligible for large q. This suggests that the energetic benefit of choosing a particular phase decreases, which is consistent with our observation that the variance in experimental bond angle distributions increase for high q.

As mentioned previously, spherical superballs form triangular lattices, which are equivalent to the Λ_0 lattice for $m = 2$. For small deviations from spheres, our calculations suggest that the Λ_0 lattice also tends to maximize ΔV_{ex}. As the deformation parameter is increased, however, the value of ΔV_{ex} for a different lattice, depending on q, surpasses that of the Λ_0 lattice. This can be seen, for example, in Figure 2.5b where the curve representing the square lattice intersects the curve representing the Λ_0 lattice. At this intersection point, the lowest energy state becomes degenerate. Near these regions, the difference in energy between the most favorable lattices is small (see Fig. 2.5d). As a result, we find experimental structures near phase boundaries fail to conform to a single coherent crystal type. Again, here we find some experimental structures are characterized by broad variances in bond angle distributions, which disallow the identification of a particular crystal type. Often, however, although there is insufficient statistical data to make a precise classification, we find the appearance of mixed assortments of crystallites of both cubic structures and undetermined, non-cubic structures within a single sample cell.

In order to more carefully probe the stability of our observed lattices, we perform ideal-

ized simulations of superballs and depletants. We first simulate finite crystallites and find the results qualitatively agree with experiments. A particular choice of initial conditions, however, may influence the vulnerability of the resulting assembly to fall into kinetic traps. In order to probe the true stability of our candidate lattices, and to remove surface effects which exist in finite crystallites, we perform bulk crystal simulations using periodic boundary conditions of each candidate lattice. Figure 2.7 shows the resulting stable lattices determined from these simulations. The results qualitatively agree with our excluded volume calculations. It is interesting to note that near phase boundaries both Λ_1 and square lattices often can be stable for the same parameters, as suggested by the appearance of mixed crystallites in experimental structures. In addition, we find that, for m values between 2 and 3, particles often assemble with irregular orientations with respect to their neighbors, consistent with the observation of indeterminate experimental structures.

2.4 Crystal-crystal phase transitions

It is particularly interesting to notice that for both experiment and simulation, we identify different crystalline structures as q is varied for $m \geq 3.5$. In principle, it is thus experimentally possible to use size-variable depletants to reversibly switch the lattice structure within a single sample. To explore this possibility, we use thermosensitive pNIPAM microgel spheres as depletants.

Using pNIPAM depletants alone to induce a crystal-crystal transition poses challenges due to the narrow parameter range which supports suitable inter particle interactions. As the particles shrink at high temperatures, the overall interaction energies decrease considerably, often melting the resulting crystals. Moreover, increasing the number density of the depletant to compensate for the energy loss, results in too strong interactions between particles when the depletant is in the expanded state. As a result, it is difficult to achieve the proper conditions for assembly at both the shrunken and expanded states for pNIPAM alone. However, we find that, using a bidepletant mixture, we are able to entropically drive a solid-

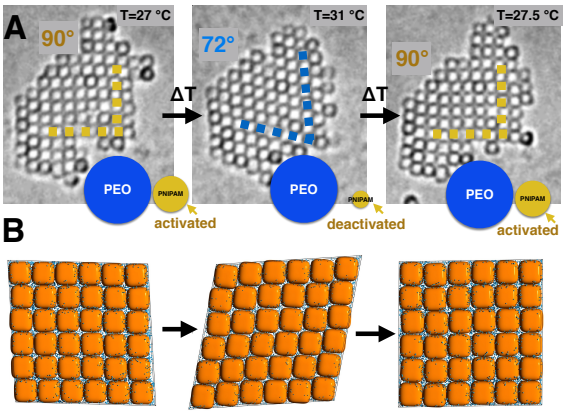

Figure 2.8: Demonstration of reversible solid-solid phase transition of superballs. (a) Colloidal superballs with shape parameter m=3.9 dispersed in depletant mixture of PEO and pNIPAM. At 27.5°C, superballs assemble into a square lattice. At 31°C, energetic contribution of PNIPAM becomes negligible, while that of PEO stays fixed, resulting in the transition into a Λ_1 lattice. (b) Simulated phase transition in a bulk crystal of superballs and depletants. A periodic lattice of superballs is simulated along with a mixture of two species of depletants, one with fixed size ratio of $q_1 = 0.35$ (which favors a Λ_1 lattice) and a smaller depletant (which favors a square lattice) of size ratio varying from $q_2 = 0.04$ to 0.032. As the smaller depletant is reduced in size, its overall energetic contribution decreases and the lattice transitions to a Λ_1 structure. When the size of the smaller depletant is once again increased, the square lattice once again emerges.

solid transition. This transition demonstrates a powerful mechanism in which leveraging different geometric features of individual particles enables one to controllably and reversibly tune their assembly.

We use superballs with shape parameter $m = 3.9$ and a mixture of Polyethylene oxide (PEO) and pNIPAM as depletant. Using the pNIPAM alone, the superballs form into square lattices at 25°C. When heated to 29°C, we find the overall superball interactions induced by pNIPAM decrease sufficiently to melt this square lattice. Moreover, when the superballs are dispersed with PEO (molecular weight of 8M) alone as depletant, we find we are able to stabilize a Λ_1 lattice of superballs.

Using a *mixture* of the two depletants, however, we are able to reversibly switch between the two lattice types by varying the temperature. At room temperature, the interactions induced by the pNIPAM are activated, and the superballs once again favor a square lattice.

As the temperature is increased, the relative energetic contribution of the pNIPAM depletant decreases, while the contribution of the PEO remains the same. Because the PEO dominates the overall energy at high temperatures, the Λ_1 lattice emerges. Figure 2.8 demonstrates this reversible solid-solid phase transition.

By performing simulations of bidepletant superball dispersions we provide further evidence of the simple entropic nature of the geometric mechanism that induces this solid-solid transition. Again we perform both periodic simulations of a bulk crystal as well as simulations of finite crystallites. Superballs are dispersed with two species of depletant, one with fixed size ratio $q_1 = 0.35$, which is found to stabilize a Λ_1 lattice, and a variable size depletant with initial size ratio $q_2 = 0.04$, which is found to stabilize a square lattice. When dispersed in a mixture with number densities $n_1 = 24.9L^{-3}$ and $n_2 = 596.8L^{-3}$ for the large and small depletant respectively, superballs with shape parameter $m = 4$ arrange into a square lattice. Here L is the diameter of the superball. As the smaller depletant is shrunk by 20% at fixed number density, its induced pressure remains fixed while its overall energetic contribution is lowered. We find, consistent with our experimental observations, the lattice becomes canted. Upon increasing q_2 once again, we find the square lattice is restored.

2.5 Conclusion

In this article we have demonstrated the reversible assembly of the same superball-shaped colloidal particles into both a square phases and the recently predicted Λ_1 phase. We show depletant size can be used to tune inter-particle interactions. As a result, both particle shape and depletant size are used to determine the resulting phases. By mixing large depletants and small thermo-sensitive depletants we demonstrate a fully reversible solid-to-solid transition between square and Λ_1 superball phases. The sensitivity of the assembled phase to a fine feature of the particle shape, combined with a mechanism to reversibly activate a depletant on that scale, demonstrates that depletants can be used to *tune* interactions. These results create new opportunities for controlling the reversible self assembly of colloidal particles and

controlling phases, for example through solid-to-solid phase transitions.

CHAPTER 3

EMERGENT GEOMETRY OF INHOMOGENEOUS PLANAR CRYSTALS

In this chapter we focus on systems where the geometry at the smallest scales is simple. In particular, the systems we will consider consist of spherically symmetric particles that locally form uniform triangular crystals. Such crystals are the ground state for particles that interact isotropically in two dimensions. However, we will see the emergence of nontrivial geometry as we immerse the particles into an external potential, for example one arising from an electric field, a flow field, or gravity. The resulting phases are significantly distorted in a way reminiscent of conformal transformations of planar lattices. We study these 'conformal crystals' using colloidal experiments and molecular dynamics simulations. By establishing a projection from these self-assembled inhomogeneous crystals to homogeneous crystals on curved surfaces, we are able to both predict the distribution of defects and establish that defects are an almost inevitable part of the ground state. We determine how the inherent geometry emerges from an interplay between the confining potential and the interparticle interactions. Using molecular dynamics simulations, we demonstrate the generic behavior of this emergent geometry and the resulting defect structures throughout a variety of physical systems.

3.1 Introduction

The work of M.C. Escher is often built on curiously distorted grids [53] (Fig.3.1(a)). Similarly, repulsive particles confined by an external potential form distorted lattice-like structures (Fig.3.1(c)) with large variations in size and orientation of identifiable local unit cells. This type of assembly occurs naturally in a diverse range of systems including electrons on the surface of liquid helium, quantum dots, one-component plasmas, and dusty plasmas [54, 55, 56, 57, 58, 59, 60, 61, 62], and has also found applicability in type-II superconductors [63,

64, 65]. Despite their ubiquity, understanding the principles that govern these structures has remained challenging because the large variations in scale and orientation are incompatible with typical treatments of condensed matter that rely on uniformity of the condensed phase.

Early theoretical studies of these structures leveraged the same mathematical transformations found in the works of Escher: conformal maps on the plane. These maps have the property of preserving angles so that perpendicular gridlines map to perpendicular gridlines. Applying these transformations to uniform triangular lattices produces 'conformal crystals' (Fig.3.1(b)), that closely resemble the inhomogeneous self-assembled structures formed by repulsive particles in a potential, and also foams, and phyllotactic patterns found in plants. This resemblance has stimulated the use of conformal maps to model such systems[66, 67, 68].

However, since conformal maps preserve angles, the resulting distorted crystals are everywhere locally six-fold coordinated. In contrast, inhomogeneous crystals found in self-assembled physical systems typically contain topological defects[56, 55, 69, 70, 71, 72, 73]. Moreover, theoretical and computational studies of electrons confined in rotationally symmetric potentials show that topological defects are directly related to the generation of density variations in the resulting structures[56, 55, 70], raising the question of whether such systems can ever self-assemble into a perfect conformal crystal. Furthermore, while defects in ordinary crystals have proven crucial in understanding the material's order, mechanics, and phase transitions[3, 74], the physics of topological defects in inhomogeneous systems remain far less understood.

Recent computational work on Coulomb interacting particles suggests that the total number of defects in inhomogenous crystals can be related to that of crystals frustrated by Gaussian curvature [70]. In this work, we generalize this concept to show that relating non-uniformity to Gaussian curvature can be used to understand how defects are distributed throughout a variety of inhomogeneous systems. Using colloidal experiments and molecular dynamics simulations, we confine repulsive particles in spatially varying potentials. We find that the particles generically form defected, inhomogeneous crystals. Instead of starting

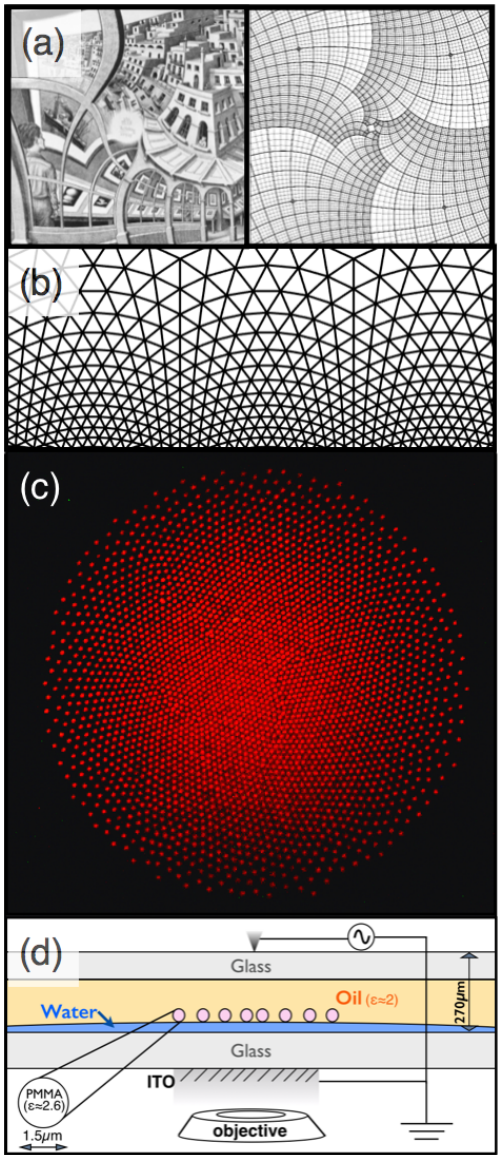

Figure 3.1: Inhomogeneous Crystals. (a) M.C. Escher's "The Print Gallery". To the right of the artwork is the conformal grid which bears striking similarity to the distorted grid used by Escher to create his piece (Image from [53]). (b) Perfectly conformal lattice used in [66] to model repulsive particles in a gravitational field. (c) Inhomogeneous crystal of repulsive colloidal particles. (d) Experimental setup. Micron-sized PMMA colloids are confined at an oil water interface. An external potential is created by applying an alternating voltage to a needle-shaped electrode above the sample. The voltage is grounded on a transparent indium tin oxide coverslip below the sample. The particles are flourescently labeled and imaged from below.

from a perfect crystal in a plane, and distorting it using a conformal map, we gain insight by carrying out the inverse process: we conformally transform our nonuniform experimental structures into lattices of uniform density. We find that, unlike the transformations demonstrated in Fig.3.1(a) and (b), which map one planar structure to another, making our experimental structures uniform requires that we map them onto a *curved* surface, where the physics of defects have been studied extensively [75, 3, 76, 77, 78, 79, 80, 81, 82].

Taking advantage of the inherent connection between inhomogeneity, defects, and curvature has recently fostered unexpected insights in seemingly unrelated systems, such as twisted bundles of filaments and nonuniformly growing elastic sheets [83, 84, 85, 86, 87]. Similarly, we find that by viewing our flat, nonuniform structures as projections of uniform crystals on curved surfaces, we are able to predict the resulting defect distributions and gain insight on their geometric function and generic behavior.

3.2 Experimental System

Colloidal experiments are conducted in glass capillary channels (height $\approx$110 μm, width $\approx$3 mm, length $\approx$22 mm) as follows. First, water-glycerol droplets (50/50 wt%) are prepared in channels while in contact with air. All glassware is first base washed in order to remove any coatings and reduce the droplet contact angles. Next, fluorescent PMMA particles (diameter $\approx$1.5 μm), prepared using the methods of Refs.[88, 89] and suspended in dodecane are filled into channel, leaving a monolayer of particles confined to the fluid-fluid interfaces. We estimate that the total integrated curvature of the region the particles are confined is on the order of 10^{-3} and, thus, any interactions with the substrate curvature are negligible. The particles are viewed from below in fluorescence with an inverted microscope.

A needle-shaped electrode is next placed on top of capillary channel above a desired water-glycerol droplet (see Fig. 3.1(d)). Alternating voltages between 1-5 kV are then applied at 100 Hz on the electrode using a high voltage amplifier. A transparent indium-tin-oxide coated coverslip is placed below the capillary and acts as the ground. After voltage is

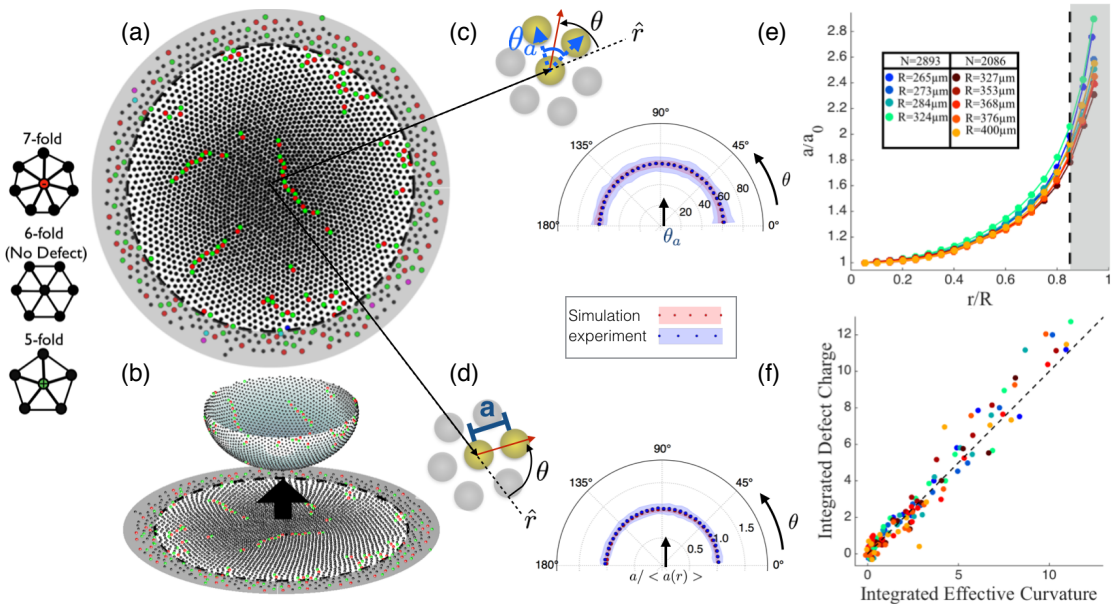

Figure 3.2: Conformal Geometry and Defects. (a) After collecting microscope images of the equilibrated system, each particle is identified and the resulting structure is triangulated. Here, 5-fold and 7-fold defects are colored green and red respectively, while black particles are un-defected. The shaded gray area represents the boundary region, which is not used for the analysis. In this region, the net defect charge drops to +6, as demanded by topological constraints. (b) Conformal transformation between inhomogeneous and homogeneous structures. Above the flat, experimental structure is the corresponding transformed, curved crystal. (c) Average angle between bonds vs. orientation of bisect. The angle between adjacent bonds is plotted against the orientation of the bisect of those two bonds with respect to the radial direction. We find that the angle of bonds is the value expected for a triangular lattice, irrespective of the orientation. In other words, adjacent bonds that are oriented in the azimuthal direction and those oriented in the radial direction both are separated by 60 degrees. (d) Average bond length vs. orientation of bond. The length of bonds, normalized by the average local lattice spacing at that distance from the structure's center, is plotted against the orientation with respect to the radial direction. We find that bond lengths are uniform, irrespective of their orientation. (e) Lattice spacing plotted against radial position in the crystal. Two sets of experiments are shown, each with a different number of particles. Each color represents a different experimental run. By changing the confinement strength, the resulting crystal sizes, R, are varied. (f) Integrated defect charge versus integrated effective curvature. The effective integrated curvature is plotted against the net defect charge for varying positions within the resulting structures. The colors shown correspond to those in (e) The dotted line represents a line with slope 1.

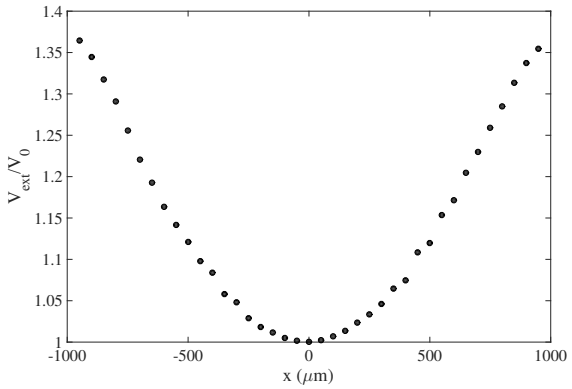

Figure 3.3: Approximate external potential for particles in colloidal experiments. Using the geometry of the experimental setup, the radial electric field profile is numerically calculated and used to model the external potential felt by the particles $V_{ext} \propto |E^2(r)|$. Note the particles in the experiment are confined to a radius $R < 500\mu m$.

initially applied, the sample is left to equilibrate for at least a day before running experiments. After varying voltage during an experimental run, the sample is left to re-equilibrate for 1-2 hours.

In order to approximately characterize the potential in which the particles are confined, the electric field profiles are numerically calculated. The calculation includes the glass boundary walls, electrode, ground, and each fluid phase with dielectric constants of each. The resulting external potential arises from a dielectrophoretic force $F \propto \nabla|E(r)|^2$. Thus, the external potential is given by $V_{ext} \propto |E(r)|^2$ (Fig.3.3). By varying the applied potential, we can easily tune the confinement strength of the system. In this confinement, as shown in Fig.3.1(c), the equilibrium particle distribution is inhomogeneous, but appears to locally maintain a triangular crystal structure.

3.3 Geometric Frustration

In the absence of a spatially varying confining potential, the particles in our experiment will form a uniform triangular (Wigner) crystal everywhere. If confined by a wall, the lattice spacing will be determined by the number of particles and the area of the box or, equivalently, the pressure supported by the edges of the box. Once the reference state is

established, deviations from the crystalline reference state, resulting in compression, shear, or topological defects, can be treated with elasticity theory [90, 91]. A spatially varying confining force produced by an external potential will give rise to a spatially varying internal pressure and thus reference lattice spacing. The body may therefore in principle possess a non-uniform lattice spacing while maintaining vanishing elastic energy.

Analysis of our crystals, however, reveals many defect patterns, including 'scars'– chains of alternating five–fold(positive topological charge) and seven–fold(negative topological charge) disclinations terminating in the bulk of the crystal (Fig.3.2(a)). This is indicative of an incompatibility between our lattice spacing variation and the triangular structure. Since it is possible to have a defect-free structure in which locally triangular patches of lattice, each with their own lattice spacing, are stitched together seamlessly (see Fig.3.1(b)), this incompatibility is not an inevitable consequence of the fact that there is a large variation in lattice spacing, rather a consequence of *how* it varies globally.

This is analogous to the frustration encountered when attempting to tile a curved surface with a uniform triangular crystal. In this case too, the frustration is not an inevitable consequence of curvature – a cylinder can be seamlessly tiled – rather a consequence of how it is curved. If Gaussian curvature is present, frustration is inevitable. This is because placing a uniform crystal on a surface with Gaussian curvature will cause lattice lines, which would otherwise be parallel, to converge or diverge, distorting the structure from the crystalline reference state. The presence of topological defects allows these rows to terminate, enabling a uniform density crystal to conform to the surface[75, 3, 76, 77, 78, 80].

3.4 Conformal Geometry, Curvature, And Defects

In inhomogeneous crystals, the lattice lines also converge and diverge. However, certain density variations can cause the lattice lines to converge or diverge in ways that do not result in frustration and thus do not require defects. How then can the presence of frustration be visualized? We first note that despite the density variation, the local structure in our

experiment is still conformal to a triangular crystal everywhere. This is can be seen in Fig.3.2(c) and (d), which shows the average angle between bonds and the local length of bonds are uniform, irrespective of their orientations. Therefore, there exists a conformal map which can transform our structure into a more crystalline one while preserving the local geometry. We use this map to create a clearer picture of the angular frustration intrinsic to the system.

Conformal transformations locally scale area elements by a factor $\Lambda^2(r, \phi)$. Two sufficiently close points which are initially spaced by ds are separated approximately by Λds after the transformation. Here, we want the spacing between particles to be uniform throughout the system. By measuring the experimental lattice spacing variation $a(r)$ we can thus deduce $\Lambda(r)$ as $\Lambda = \frac{a_0}{a(r)}$ where a_0 is an arbitrary target uniform lattice spacing.

The metric of a sufficiently smooth surface can also be expressed as $\Lambda^2 ds^2$, where $ds^2 = (dr^2 + r^2 d\phi^2)$ corresponds to a flat metric [92]. When written in this form, the Gaussian curvature, K, of the surface can be computed in terms of Λ:

$$K(r) = \frac{1}{\Lambda^2(r)} \Delta \ln(\frac{1}{\Lambda(r)}). \tag{3.1}$$

Note that the spatial variations in lattice spacing do not automatically produce an underlying non-zero Gaussian curvature. Variations that satisfy a laplacian $\Delta \ln(\Lambda(r)) = 0$ such as those found in Fig.3.1 (a) and (b) are intrinsically flat.

By determining the appropriate scaling factor Λ (Fig.3.2(b)), one can establish the presence or absence of an underlying Gaussian curvature of the transformed, uniform crystal. We find that our experimental structures are always curved and Fig.3.2(c) shows the curved surface corresponding to a typical experimental structure. Note that there is an additional freedom in choosing the embedding of our curved surface, however, only the Gaussian curvature itself, and not the particular embedding, is used in our analysis.

Thus, such self-assembled inhomogeneous crystals are naturally modeled, not by maps from the plane to the plane, but from a curved surface to the plane, like stereographic

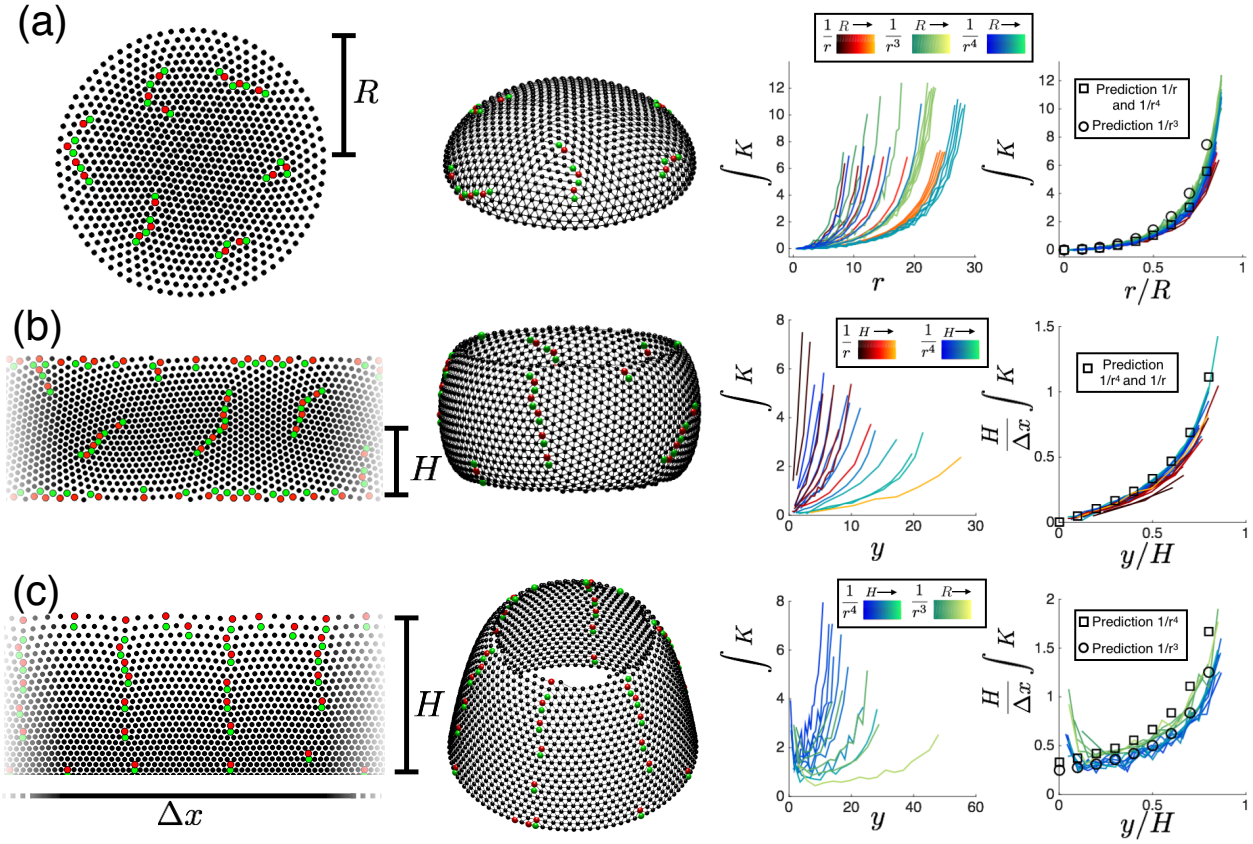

Figure 3.4: Structures of simulated confined crystals. (a) Rotationally symmetric potentials. An example low energy configuration of Coulomb-repusive particles confined inside the potential $V_{ext} \propto r^2$ is shown on the left next to the corresponding uniform curved crystal. On the right of the crystal is a plot of the integrated curvature for particles in rotationally symmetric parabolic potentials interacting via various inverse power-law potentials and the result after scaling by the overall system size. (b) Results for translationally symmetric potentials. An example low-energy configuration of $\frac{1}{r^4}$ interacting particles inside of the potential $V_{ext} \propto y^2$ next to the corresponding uniform curved structures. The simulated system is carried out with periodic boundary conditions. Note, the entire crystal is not shown. Shown on the right is the integrated curvature profile for various inverse power law interactions and the result after scaling by the overall system size. In this case, the integrated curvature scales linearly by the lateral system size, and thus the integrated curvature must be scaled by crystal aspect ratio. (c) Result for particles in a constant force field ($V_{ext} \propto y$)in the presence of a wall at the bottom of crystal. Again, the simulated system is carried out with periodic boundary conditions and the entire crystal is not shown.

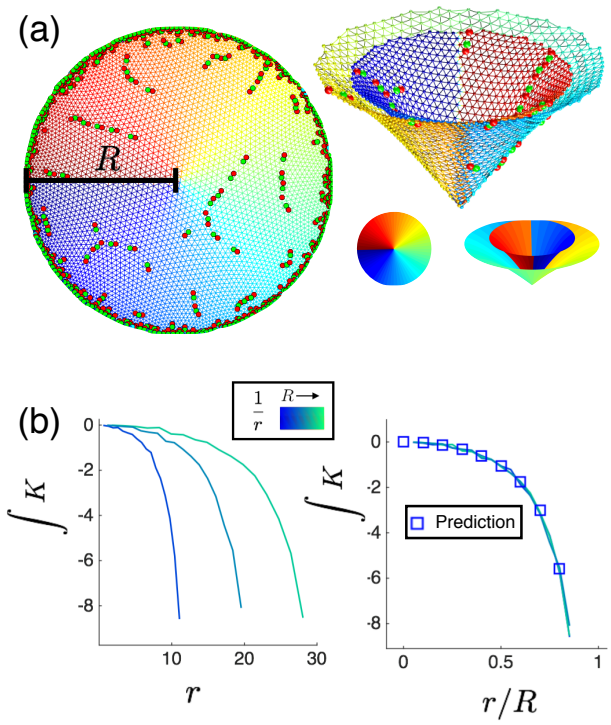

Figure 3.5: Simulated hard wall confined crystal with corresponding negatively curved surface. (a) Circular wall boundary. An example low energy configuration of Coulomb-repusive particles confined inside a circular hard wall boundary is shown next to the corresponding uniform curved crystal. Embedding the entire structure requires covering the surface multiple times (see Appendix A). In order to separate the different coverings, the surface is slightly distorted. (b) Integrated curvature, which collapse when rescaled by the system radius.

projections used to make maps of the earth. This makes curved space crystallography the natural starting point for modeling the defect structures that are observed in self-assembled inhomogeneous crystals and provides a natural explanation for the presence of defect structures, such as scars and pleats, which enable the relief of angular strain induced by Gaussian curvature.

Eq.3.1 is identical to a quantity found in Ref.[93] known as the amount of "extra matter" in an elastic body. This quantity is derived from the non-metricity tensor, the covariant derivative of the relaxed state's metric. Eq.3.1 is also identical to the relationship for disclination charge in confined one-component plasmas derived in [56]. This relationship is derived from a counting argument for the burgers vector density resulting from the lattice spacing variation. Using our mapping to a curved surface, we can understand the relationship between the disclination density and the frustration caused by lattice variation using known results from curved space crystallography. On a curved surface, the sum of the internal angles in a geodesic triangle will differ from the flat space value by the amount of integrated Gaussian curvature in the interior of the triangle. This angular mismatch is accounted for by the presence of disclinations in the crystal. In particular, within a patch of smoothly curved surface, the integrated Gaussian curvature will be approximately proportional to the net defect charge[80].

To demonstrate this relationship for our inhomogeneous crystals, we integrate the effective Gaussian curvature within increasing radii from the center of the structure, and compare the result to the net topological charge within that radii. Fig.3.2(f) shows the relationship between the effective Gaussian curvature extracted from the experiment and the topological defect charge for a range of external potential strengths. We find the quantity shown in Eq.3.1 effectively predicts the distribution of topological defects induced by density inhomogeneities in our experiment.

We note that the overall number of excess defects in the system will be fixed by topological constraints. In particular, our planar experimental structures must have an excess topological

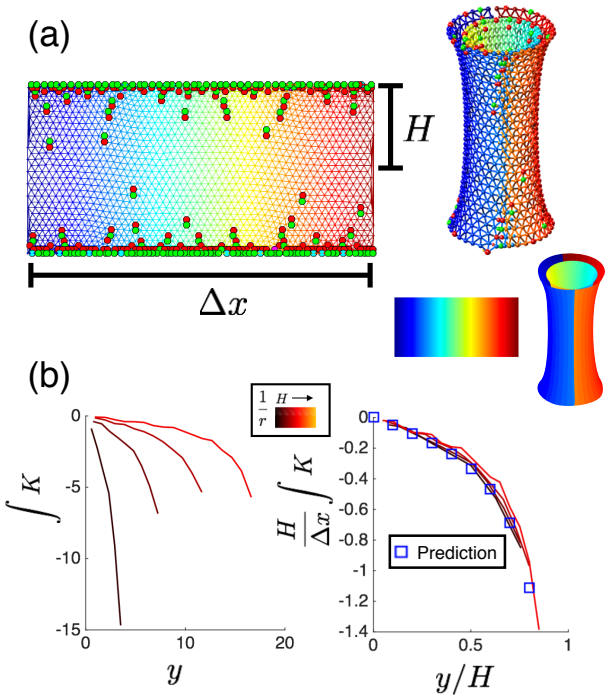

Figure 3.6: Simulated hard wall confined crystal with corresponding negatively curved surface. (a) Translationally symmetric hard wall boundary. An example low energy configuration of Coulomb-repusive particles confined inside a hard wall boundary is shown next to the corresponding uniform curved crystal. Embedding the entire structure requires covering the surface multiple times (see Appendix A). In order to separate the different coverings, the surface is slightly distorted. (b) Integrated curvature, which collapse when rescaled by the system radius.

charge of +6. We find that, while the integrated topological charge within the bulk of our system can exceed this amount by more than a factor of two, the total charge meets the topological constraint due to disclinations located near the boundary.

3.5 Scaling of integrated curvature

The distribution of defects are predicted purely from geometric arguments. Thus, the analysis we have presented can easily be applied to a wide range of physical systems. To demonstrate the generality of these results we perform molecular dynamics simulations [1][94, 95]

1. Simulations performed using HOOMD-blue: http://codeblue.umich.edu/hoomd-blue

of particles interacting through a variety of interaction potentials within external confining potentials.

3.5.1 Simulation details

Molecular Dynamics simulations are performed using HOOMD-Blue [2][94, 95] at constant volume. Particles were annealed from a disordered state by gradually lowering the system temperature until particles are no longer able to rearrange. Temperature ramping parameters vary between systems and need to be chosen independently between runs in order to ensure simulation stability and proper assembly. After this annealing procedure, the resulting configurations are relaxed using the Fast Inertial Relaxation Engine (FIRE) in order to obtain the final structures. Note that the result is thus a zero temperature, approximately energy minimized structure. Thus, other techniques, such as Monte Carlo methods, could also have been used.

We explore external potentials with rotational symmetry as well as potentials with translational symmetry, as shown in Fig.3.4. In the case of rotationally symmetric external potentials, the simulation box size is chosen to be much larger than the resulting structures. In the case of translationally symmetric potentials, the lateral dimension of the simulation is treated with periodic boundary conditions, while the vertical direction is chosen to be much larger than the size of the resulting structures. Potentials which do not have their minimum in the interior of the simulation box need to include walls to prevent particles from escaping. In addition, walls are needed for cases where no other confinement potential is present, as is the case for the negative effective curvature systems studied here. Walls are implemented with Lennard-Jones type forces:

$$\vec{F} = -\nabla V(r) \qquad r < r_{cut} \tag{3.2}$$

$$= 0 \qquad r \geq r_{cut} \tag{3.3}$$

where

$$V(r) = 4\epsilon \left(\left(\frac{\sigma}{r}\right)^{12} - \alpha \left(\frac{\sigma}{r}\right)^{6} \right) \tag{3.4}$$

with parameters chosen such that the simulation remains stable and the wall does not directly interact with the bulk structure. In the case of the circular boundary, the circle was discretized with 24 straight walls.

3.5.2 Ground-state Lattice Spacing

Our results indicate that the effective integrated curvature robustly predicts the defect distribution across all systems we have investigated. How is the effective curvature determined by the physical parameters of the system? By tuning interaction and confinement potentials, we observe that the resulting structures vary in overall size by factors of 3 or more. Despite this, we find that the curvature distribution, when rescaling coordinates by the respective system sizes, collapse onto each other (Fig.3.4).

To examine the generality of this scaling behavior, we relate the physical system parameters to the resulting curvature profiles. We first determine the lattice spacing variation as follows. Suppose N repulsive particles are immersed into a rotationally symmetric external potential,V_{ext}. We assume the system locally obeys the equilibrium condition:

$$\nabla P(r) + n(r)\nabla V_{ext}(r) = 0. \tag{3.5}$$

Here, $n(r)$ is the local number density. The pressure, P, is computed from the internal energy, U, by $P = -dU/dV$. Assuming local crystallinity, the lattice spacing is related to the number density as $n(r) = 1/V = \frac{2}{\sqrt{3}a^2(r)}$.

By relating the chemical potential, $\mu(r)$, to the pressure, $nd\mu = dP$, we recast the condition in Eq.3.5 as:

$$\mu(r) + V_{ext} = E, \tag{3.6}$$

where E is a constant throughout the system.

Thus, given an interaction potential V_{int}, one can compute the internal energy, and thus the pressure and chemical potential $\mu(r)$ in terms of the local density. Using Eq.3.6, the local density can then be determined as demonstrated below.

Power Law Interactions in Rotationally Symmetric Attractive Confinement

Consider interaction potentials of the form $V_{int} = \frac{1}{r^m}$ and external potentials of the form $V_{ext} = \gamma r^n$, where $m > 0$, $\gamma > 0$, and $n > 1$. If we assume the neighborhood around each particle is crystalline, we can write down the pairwise interaction energy in terms of a multiple of the lattice spacing. The internal energy of a particle is then obtained from summing over the pairwise interaction between all other particles in the system $U(r) = \frac{k}{a^m(r)}$ where

$$k = 3\sum_{i=1}\sum_{j=0}\frac{1}{\left((i+j/2)^2 + \left(\sqrt{3}j/2\right)^2\right)^{m/2}}. \tag{3.7}$$

Note this summation only converges for powers $m > 2$. Cases where $m \leq 2$ must be treated separately (see Sec.3.5.2). Moreover, due to the varying lattice constant, the expression for the interaction constant shown in Eq.3.7, which assumes perfect crystal order, is only an approximation. The approximation is valid, however, when the lattice spacing change is small in the area in which the summation sufficiently approaches the convergent value.

In this case, Eq.3.6 takes the form

$$\frac{k(m+2)}{2a^m} + \gamma r^n = \frac{k(m+2)}{2a_0^m}. \tag{3.8}$$

Therefore,

$$a(r) = \frac{a_0}{\left(1 - \left(\frac{r}{R}\right)^n\right)^{\frac{1}{m}}} \tag{3.9}$$

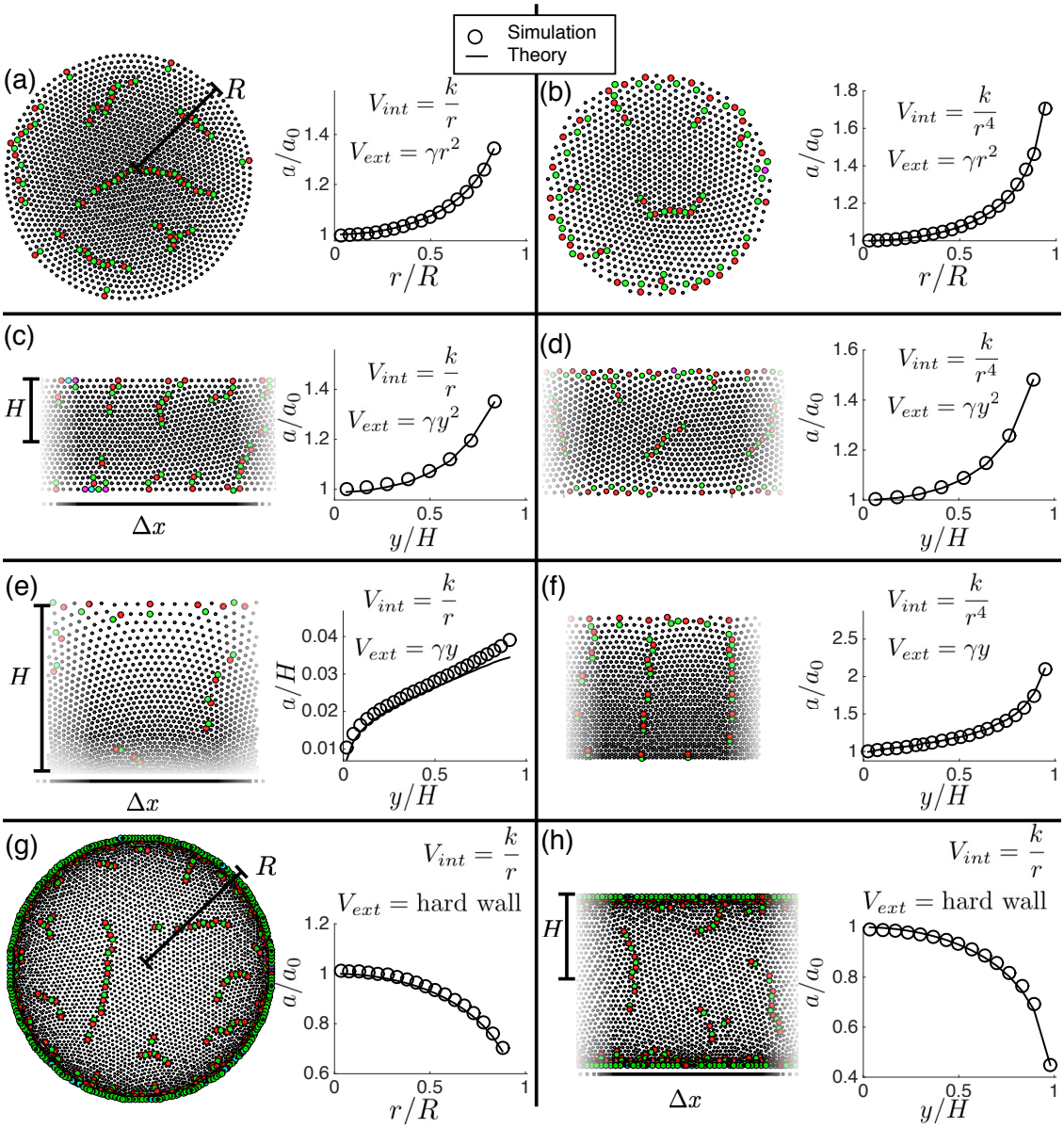

Figure 3.7: (a)-(h) Typical lattice spacing variation of various systems examined. To the left of the lattice spacing variation is the simulated particle configuration. Theoretical lattice spacing variations with no free parameters are plotted along with the variations measured from simulation data. Lattice spacings are scaled by predicted initial spacings a_0 and coordinates are scaled by calculated system sizes R and H. For rotationally symmetric systems, R refers to the radius of the crystal, as shown in (a) For translationally symmetric systems, Δx refers to the distance lateral size of the system, as shown in (c) and (e). Note that configurations (c)-(f) and (h) are cropped at the edges and thus only partially shown, so the actual lateral sizes are larger than what is pictured. For systems with $V_{ext} = \gamma y$, H refers to the width of the system in the y-direction, as shown in (e). For systems with $V_{ext} = \gamma y^2$, H refers to half the width in the y direction, as shown in (c).

where $R = \left(\frac{k(m+2)}{2\gamma a_0^m}\right)^{\frac{1}{n}}$ is the resulting crystal radius. The initial lattice spacing, a_0 is determined from the normalization condition:

$$N = \int n(r) d^2 r. \tag{3.10}$$

Fig.3.7(b) shows the lattice spacing variation of a typical simulation compared to this calculation.

Power Law Interactions in a Translationally Symmetric Attractive Confinement

The above arguments can easily be applied to systems with translational symmetry. Consider, for example, potentials of the form $V_{ext} = \gamma|y|^n$ and $V_{int} = \frac{1}{r^m}$, where $m > 2$, $\gamma > 0$, and $n \geq 1$. The arguments in the previous section once again hold, resulting in the lattice spacing variation:

$$a(r) = \frac{a_0}{\left(1 - \left(\frac{y}{H}\right)^n\right)^{\frac{1}{m}}} \tag{3.11}$$

where $H = \left(\frac{k(m+2)}{2\gamma a_0^m}\right)^{\frac{1}{n}}$. Fig.3.7(d) and (f) show example simulation lattice spacing variations compared to this calculation.

The Coulomb Interaction

The approximation shown in Eq.3.7 is not valid in cases where $m \leq 2$. In this case, the summation used to compute the interaction constant is not convergent. Therefore, in the case of Coulomb repulsion between particles, the local internal energy must take into account density variations over the entire system:

$$U(r) = \int d^2 r' \frac{n(r')}{|r^2 - r'^2|} \tag{3.12}$$

In the case of rotationally symmetric parabolic external potentials, $V_{ext} = \gamma r^2$, the resulting lattice spacing variation can be shown[54, 55, 56] to be

$$a(r) = \frac{a_0}{\left(1 - \left(\frac{r}{R}\right)^2\right)^{\frac{1}{4}}} \tag{3.13}$$

where $a_0 = \sqrt{\frac{2\pi^2}{4\sqrt{3}\gamma R}}$ and $R = \left(\frac{3\pi N}{8\gamma}\right)^{\frac{1}{3}}$ are again given by the normalization condition Eq.3.10 (see Fig.3.7(a)).

In the presence of only a hard wall confinement, the distribution of particles also becomes inhomogeneous as a result of the long range nature of the interactions. In this case, the resulting lattice spacing can be shown[56] to be:

$$a(r) = a_0 \left(1 - \left(\frac{r}{R}\right)^2\right)^{\frac{1}{4}} \tag{3.14}$$

where $a_0 = \sqrt{\frac{4\pi R^2}{\sqrt{3}N}}$ is given by normalization Eq.3.10 (see Fig.3.7(g)).

The distribution of particles can also be calculated in the case of 1-D (translationally symmetric) confinements. For hard-wall confinements, the particle density has the form of the charge density on a conducting strip[96]:

$$\rho(y) = \frac{\lambda}{\pi} \frac{1}{\left(1 - \left(\frac{y}{H}\right)^2\right)^{\frac{1}{2}}}, \tag{3.15}$$

where y is the distance from the center of the strip in the finite dimension, H is the width of the strip, λ is the charge per unit length in the lateral dimension, and the lattice spacing $a(y) = \sqrt{\frac{2}{\sqrt{3}\rho}}$ (see Fig.3.7(h)).

In the case of 1-D parabolic confinement, $V_{ext} = \gamma y^2$, the density variation has the form:

$$\rho(y) = \rho_0 \left(1 - \left(\frac{y}{H}\right)^2\right)^{\frac{1}{2}}, \tag{3.16}$$

where $\rho_0 = \frac{\gamma H}{\pi}$, $H = \sqrt{\frac{2\lambda}{\gamma}}$, and λ is the charge per unit length in the lateral dimension[97, 98]. See Fig.3.7(c).

Finally, for linearly varying potentials in the presence of a hard wall, such as in the case of charged particles in a uniform electric field with a barrier or massive particles under the influence of gravity, the density takes the form of a charged conducting strip in a uniform external field:

$$\rho(y) = \frac{\frac{N}{\pi\Delta x} - \frac{\gamma}{2\pi}(y - \frac{H}{2})}{\sqrt{\left(\frac{H}{2}\right)^2 - (y - \frac{H}{2})^2}}, \tag{3.17}$$

where $H = \frac{4N}{\gamma\Delta x}$ is given by the condition that the density vanishes at H (see Fig.3.7(e)). This result is derived from the solution for the potential near a charged conducting cylinder placed in a uniform electric field. Using the Juokowski transformation, the solution for the cylindrical case can be mapped to the case of a conducting strip of charge in a uniform field, giving Eq.3.17.

3.5.3 Integrated Gaussian Curvature

Rotational Symmetry

The effective Gaussian curvature can be computed using

$$K_{eff}(r) = \frac{a^2(r)}{a_0^2}\Delta \ln\left(\frac{a(r)}{a_0}\right). \tag{3.18}$$

Integrating this expression, assuming rotational symmetry of the lattice spacing variation, we have

$$\int K dA = \frac{2\pi}{a}\frac{da}{dr}. \tag{3.19}$$

In cases where, a(r) has the form shown in Eq.3.9, we have

$$\int K dA = 2\pi\left(\frac{r}{R}\right)\frac{n}{m}\frac{\left(\frac{r}{R}\right)^{n-1}}{1 - \left(\frac{r}{R}\right)^n}. \tag{3.20}$$

For Coulomb interacting systems, the lattice spacings are given by Eq.3.13 and 3.14. Using 3.19 results in the same form of the integrated curvature as Eq.3.20, but with the parameters n and m redefined.

Translational Symmetry

For translationally symmetric density variations, the integrated curvature takes the form:

$$\int K dA = \frac{\Delta x}{a}\frac{da}{dy}. \tag{3.21}$$

Here, Δx is the lateral size of the system. In the simulations presented here, periodic boundary conditions are used in the lateral dimension and Δx is the distance between periodic boundaries.

For the lattice spacing variation shown in Eq.3.11, the integrated curvature takes the form:

$$\int K dA = \frac{\Delta x}{H}\frac{n}{m}\frac{\left(\frac{y}{H}\right)^{n-1}}{1-\left(\frac{y}{H}\right)^{n}}. \tag{3.22}$$

Here Coulomb interacting systems must again be treated separately. The lattice spacings are given by Eq.3.15–3.17. For all cases except Eq.3.17, using 3.21 results in the same form of the integrated curvature as equation 3.22, but with the parameters n and m redefined.

For the case of Coulomb particles in a uniform field, given by Eq.3.17, the integrated curvature takes the form:

$$\int K dA = \frac{\Delta x\left(4HN - 8Ny + \Delta x H^2\gamma\right)}{4y(H-y)(4N + \Delta x(H-2y)\gamma)} \tag{3.23}$$

3.5.4 Scaling of Defect Distributions

For all systems obeying integrated curvatures of the forms in Eqs.3.20 and 3.22, rescaling coordinates by the crystal size reveals that the curvature distributions collapse onto single curves which are determined solely by the powers of the internal and external potentials.

In particular, all prefactors of the interaction and external potentials are absorbed into the system sizes R and H. This result suggests that the relative distribution of curvature in these systems is robust against physical parameters. In particular, changing the relative strengths of the external and interaction potentials modifies the crystal size, but has little effect on the relative distribution of topological defects. We also explore the effect of modifying the interaction potential through the explicit addition of a length scale using a Yukawa potential. We observe that while this length scale may disrupt the above scaling, the relation between curvature and defect charge still holds.

These results reveal the extent to which the distribution of curvature and, thus, defects in confined systems may be manipulated. Examining Eq.3.1 also reveals that the curvature can be tuned to change sign. A change in sign occurs when the derivative of the lattice spacing changes sign. Qualitatively, this will change the direction of polarization of dislocations and will cause the system to favor a net of seven-fold defects instead of five-fold defects(or vice-versa). This can be seen for example, by comparing coulomb repulsive particles confined by hard walls (shown in Fig.3.5 and 3.6) [56, 72, 73, 70] with the structures shown thus far. In this case, the long range interactions themselves create density inhomogeneities in the resulting wigner crystal [56]. Again, we find Eq.3.20 and 3.22 predict the effective integrated curvatures, and thus the defect distributions. Fig.3.5 and 3.6 show the resulting structures and negatively curved surfaces.

In order to stabilize a defect-free structure, our results suggest that the integrated curvature must vanish everywhere in the domain. Eq.3.1 thus suggests that defects should be expected for all lattice spacing variations which do not have the form of a power law. In all the structures we have observed, the lattice spacings diverge at finite length scales, and thus do not take on a power-law form. This suggests that, for potentials we have explored, topological defects should be present for all interaction and confinement strengths.

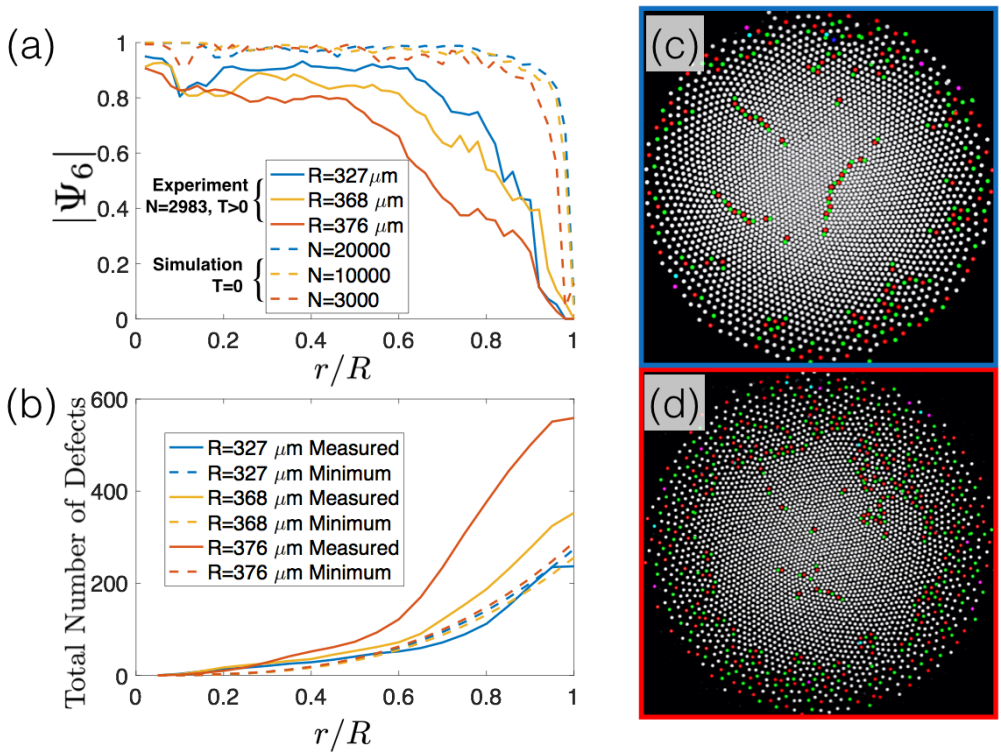

Figure 3.8: Inhomogeneous onset of melting. (a) Order parameter variation. Magnitude of orientational order parameter $|\Psi_6|$. We find that the onset of melting occurs further into the bulk as the confinement strength is reduced, an effect absent in the simulated zero temperature configurations. (b) Total number of defects. Total number of defects are compared to the approximate minimum number needed. Here, confinement strength is characterized by the resulting crystal size. Experimental crystal representing stronger confinement is shown in (c) and weaker confinement in (d)

3.6 Finite Temperature

The simulated results discussed above have informed our understanding of the minimum energy defect configurations of inhomogeneous crystals. In real assembly processes however, the effects of temperature can also influence the excitation of defects [99]. This is the case, for example, in our experimental system.

In particular, we observe that as we reduce the confinement strength, the experimental structures are characterized by a growing disordered region at the edge, as shown in Fig.3.8(d). To characterize this disorder, we use magnitude of the orientational order parameter, $|\Psi_6(r_m)| = \frac{1}{N_b}|\sum_{n=1}^{N_b} e^{6i\theta_{nm}}|$, where, N_b is the number of bonds of a particle m located at r_m, and θ_{nm} is the angle of the bond joining particles m and n. Fig.3.8(a) shows that the disordered region grows in from the edge as the confinement strength is reduced. We observe that this effect is absent in zero-temperature simulated structures, irrespective of tuning.

What consequences will the observed inhomogeneous melting have on the distribution of curvature, and thus, defects? Surprisingly, we observe that the relationship between net defect charge and curvature persists, as shown in Fig.3.2(d). This suggests that the notion of effective curvature may be applicable even in the melted, or partially melted state.

While the balancing of net defect charge and curvature is robust against the effects of temperature, partial melting does have consequences for the overall number of defects in the system. In particular, in figure 3.8B, we show the minimum number of defects required to balance the curvature and the measured number of defects. The minimum number of defects is calculated by relating the observed lattice variation to the dislocation density [56]. To approximate the minimum number of defects, we calculate the dislocation density needed to support the observed lattice variation [100]. This done by first computing the Burgers vector density [56]

$$\vec{b}(r) = a(\vec{r})\hat{z} \times \nabla a^{-1}(\vec{r}) \tag{3.24}$$

Dividing the Burger's vector density by the distance between lattice lines ($a\sqrt{3}/2$), we obtain the density of dislocations. We then multiply this number by 2, and compare to the number of particles with coordination number not equal to 6 to obtain Fig.3.8(b). We find that the total number of defects grows away from the minimum required number as the confinement strength is reduced, a further characteristic of melting.

3.7 Conclusion

We have used the inherent connection between topological defects and curvature to reveal generic behavior in confined crystalline systems. In particular, we show that inhomogeneity in density can frustrate a crystal in a manner similar to out of plane Gaussian curvature. For structures self-assembled in external potentials like the ones explored here, we find this frustration is generic, suggesting they always have defects. Thus, our results suggest that it may not be possible for perfect conformal crystals to self-assemble. An interesting extension of these concepts may be the use of defects to engineer density variations, much like their use in engineering curvature [101, 102, 103].

CHAPTER 4

FREE SURFACE DYNAMICS IN A CHIRAL COLLOIDAL FLUID

In this final chapter, we will move away from systems composed of static build blocks, and instead activate the underlying 'atoms' of a material by spinning them. Interesting hydrodynamics will emerge in the resulting material, called a chiral fluid. We will fully describe these hydrodynamics by studying how the surface of the fluid evolves in time.

Hydrodynamic theories describe the flow of systems as diverse as water, quantum electronic states [104], and galaxies [105] over decades in scale [106]. Since hydrodynamic equations are built on symmetry principles and conservation laws alone, systems with similar symmetries have similar descriptions and flow in the same way.

For example, symmetry under parity and time reversal – conditions met by all conventional fluids at thermal equilibrium – constrains both the stress and viscosity tensors to be symmetric. These constraints are in principle alleviated in collections of interacting units that are driven to rotate [107, 108, 109, 110, 111, 112, 113, 26, 114]. This seemingly innocent twist on an otherwise structureless fluid represents, however, an elemental change with rich hydrodynamic consequences common to quantum Hall fluids, vortex fluids, and chiral condensed matter. Collections of spinning particles offer a natural opportunity to engineer and study the properties of such chiral fluids; experimental examples include rotating bacteria [115], colloidal and millimeter-scale magnets [116, 117, 118, 119, 120, 121, 122], ferrofluids in rotating magnetic fields [123, 124], and shaken chiral grains [107, 125]. Such systems have been shown to have non-trivial dynamics. For example, ferrofluids driven by AC fields can flow against external pressure [126] and small numbers of spinning particles self-assemble into dynamic crystalline clusters [116, 117, 118, 119, 127, 121, 122].

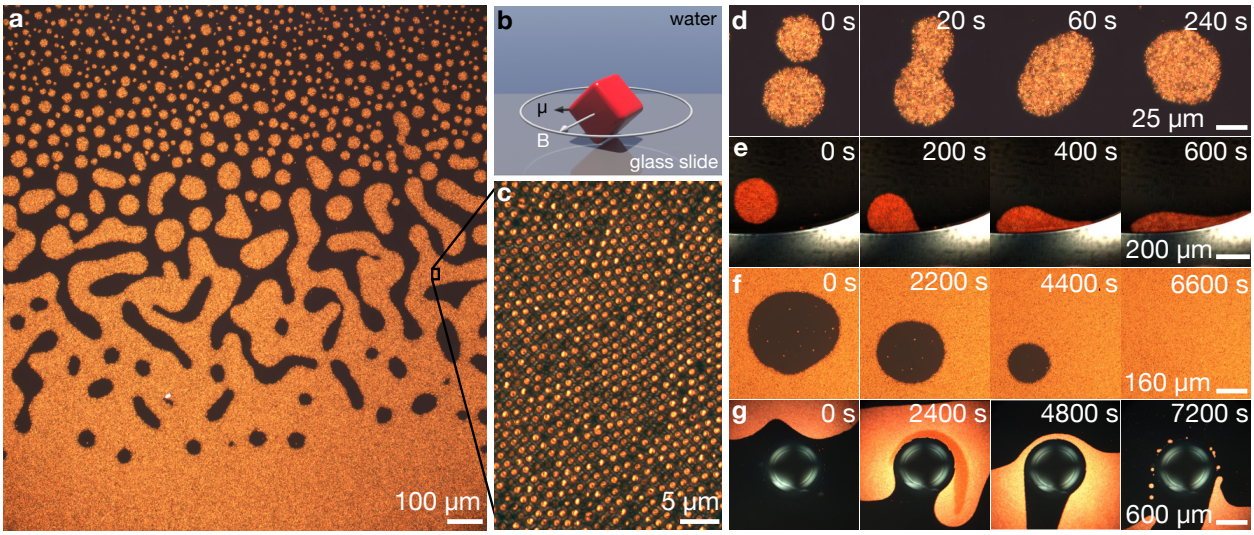

Figure 4.1: **A chiral fluid of spinning colloidal magnets.** (a) Optical micrograph of the colloidal magnets in bulk, after a few minutes of spinning. (b) Schematic of one colloidal particle. The $\sim$1.6 μm hematite colloidal cubes have a permanent magnetic moment (μ, black arrow). They are suspended in water, sedimented onto a glass slide, and spun by a rotating magnetic field (B, white arrow tracing the white circle). (c) Optical micrograph of the bulk colloidal magnets at increased magnification. **d-g,** The particles attract and form a cohesive material with an apparent surface tension that, over timescales from minutes to hours, behaves like a fluid: **d**, clusters coalesce and **e** spread like liquid droplets when sedimented against a hard wall; **f** void bubbles collapse; and **g** when driven past an obstacle, the fluid flows around it, thinning and eventually revealing an instability to droplet formation. All images were taken through crossed polarizers.

4.1 A colloidal chiral fluid

We report the creation of a millimeter-scale cohesive chiral fluid (Fig. 4.1a) by spinning millions of colloidal magnets with a magnetic field (Figs. 4.1b, 4.1c). As explained below, we then observe and its flows over hours.

4.1.1 Creating colloidal chiral fluids

We synthesize hematite cubes following the method described by Sugimoto et al in [128], and subsequently coat them in a thin silica shell using a Stöber method described in [129]. We suspend the cubes in water and, unless otherwise noted, we enclose the suspension in a glass chamber (see Figure 4.2a).

Low-friction experiments

Low-friction experiments are performed by placing the particles at a fluid-fluid interface between water and either oil or air. In these experiments the particles are suspended in a water mixture with 15 wt% glycerol to mediate evaporation. In addition, we add a surfactant (4 mM Sodium dodecyl sulfate , Sigma-Aldrich), to prevent the particles from breaching the interface. We pipette a small amount of the particle suspension ($\sim 0.7\,\mu$L) on a glass slide and enclose it in a glass chamber. The remainder of the chamber is either left empty (air interface experiments) or filled with pure silicone fluid (Clearco Products) of variable viscosity (oil interface experiments). The entire sample is then held such that the cubes sediment with gravity to the water/air (oil) interface. A typical sample geometry is illustrated in Figure 4.2b. The typical radius of curvature is $R \sim 10^5\,\mu$m. For a typical droplet of fluid $R \sim 100\,\mu$m, this amount of curvature varies the particle rotation axis by an angle $\theta \sim 0.2^\circ$ with respect to the substrate, resulting in negligible amounts of rolling motion (see Figure 4.3c).

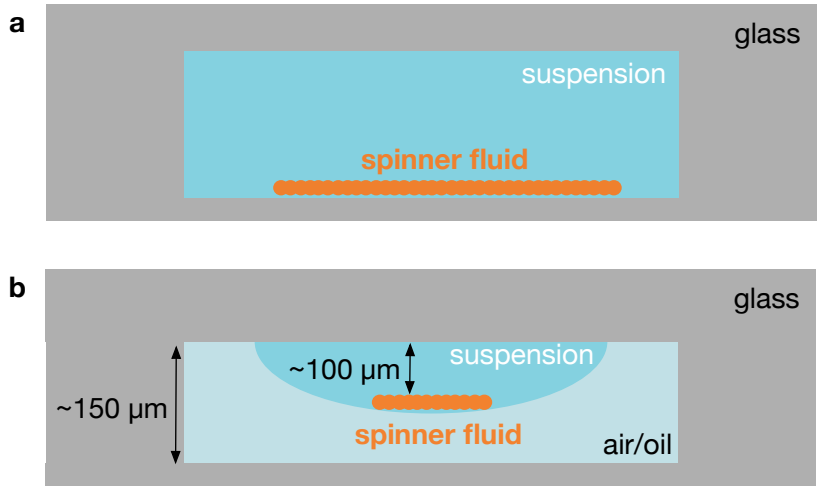

Figure 4.2: **Colloids at interfaces of variable friction.** (a) In the conventional geometry cubes are sedimented onto a glass substrate. (b) By contrast, to achieve lower substrate friction, a droplet of colloidal suspension is enclosed in glass chamber otherwise filled with either oil or air, allowing the colloids to sediment onto a fluid-fluid interface.

Driving

Colloids are then spun using a magnetic field we generate using three pairs of coils. In all experiments we control the magnitude ($B = 1.3$ mT) and orientation of the magnetic field with a computer. We program the field parameters in a Python script and send them to a National Instruments DAQ card (PCIe-6363) via the PyDAQmx Python driver. We then amplify the DAQ output voltage by a custom voltage-to-current amplifier that powers each coil pair. We record the currents through all coils continuously, so the orientation of the magnetic field at every moment in time is known.

Roll and drift compensation In order to observe dynamics at long timescales, care must be taken to minimize particle drift. Drift can occur either due to a tilt of the experimental setup with respect to gravity, which will cause sedimentation; or due to a misalignment of the spinning axis of the magnetic field, which will cause rolling (see Figure 4.3a, b). In the case of low-friction experiments, particles naturally collect in a locally flat region due to

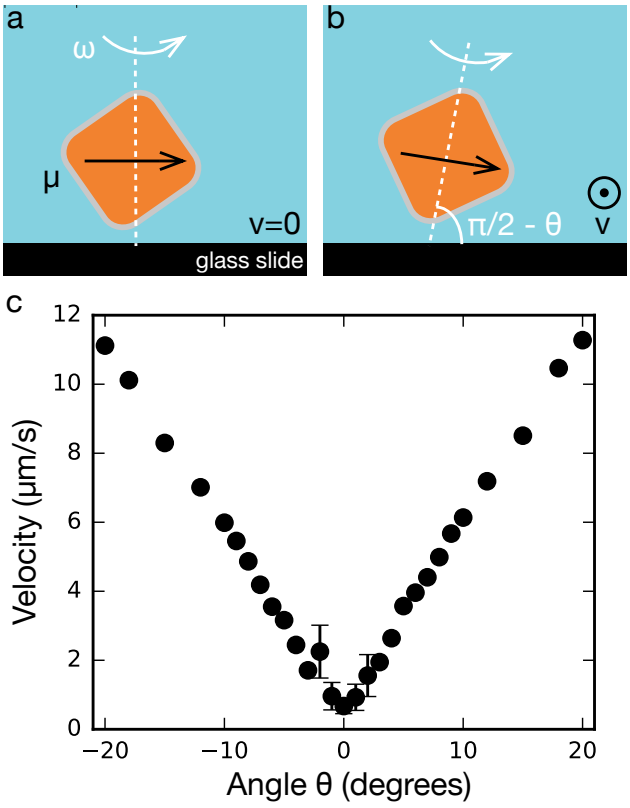

Figure 4.3: **Rolling motion.** (a) If the rotation axis of the magnetic field is perpendicular to the substrate, the particle spins in place without rolling. Its translational velocity vanishes, $v = 0$. (b) If the rotation axis of the magnetic field is not perpendicular to the substrate and deviates from the normal by an angle θ, the particle will roll as it spins and $v \neq 0$. (c) The rolling speed depends linearly on the tilt angle θ for angles at least up to 20 degrees.

gravity, eliminating sedimentation. Meanwhile, for high-friction experiments, we minimize sedimentation by adjusting the tilt of the sample with the magnetic field off. As shown in Figure 4.3c, the rolling velocity is linearly proportional to the angle between the spinning axis and the normal to the substrate for a wide range of angles. We minimize rolling by adjusting the relative amplitudes of the currents through all three coil pairs until particle clusters do not move by more than a couple of pixels within a couple of minutes.

Our setup allows arbitrary control of the magnetic field axis, which enables rolling the particles in any desirable direction. This feature is very useful for the preparation of the initial state in many of our experiments.

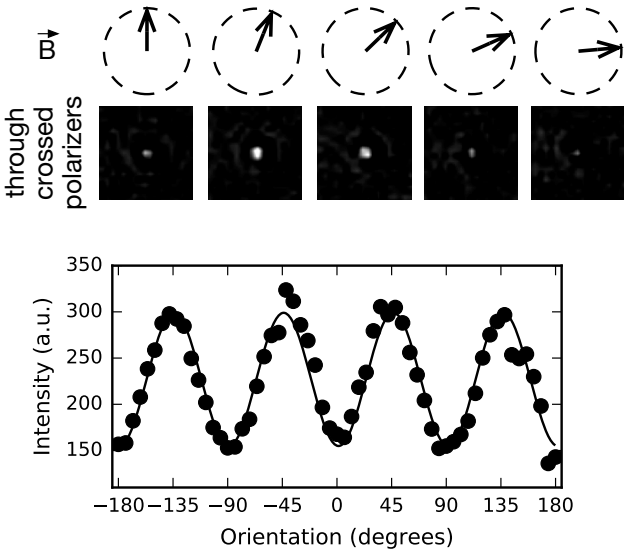

Figure 4.4: **Measuring the particles' spinning frequency.** (a) When viewed through crossed polarizers, a hematite cube blinks four times during one full rotation. This allows us to confirm that, in our experiments, the particles spin at the frequency set by the rotating magnetic field. (b) We hold several isolated particles (∼15) at fixed angles and we record their mean intensity. All particles blink four times in one full rotation of the magnetic field.

4.1.2 Observing the fluid

We observe the individual colloidal particles and the macroscopic flows of spinner fluids either with a Nikon Eclipse TE2000-U microscope and 10x-100x objectives, or with a Zeiss Axio Zoom.V16 microscope and a 2.3x objective that allows continuous magnification from 16.1x to 258x. We record slow dynamics ($\leq$5 fps) with a color camera (Grasshopper2 GS2-GE-20S4C-C, Grasshopper3 GS3-U3-123S6C-C) and fast dynamics (∼1000 fps) with a black-and-white camera (Phantom v12, Phantom v2512, Phantom VEO 640S).

Our the colloidal particles are birefringent: when imaged through crossed polarizers, their intensity depends on their orientation. In particular, they blink four times during one full rotation as illustrated in Figure 4.4. Thus, by monitoring the intensity of the spinner fluid with a camera triggered in synchrony with the magnetic field, we confirm that the particles rotate at the rotating frequency of the driving magnetic field up to 15 Hz.

After confirming that the particles rotate at the same rate Ω, we measure the instanta-

neous particle positions. We first average frames over one intensity oscillation, in order to avoid brightness fluctuations. We then identify particle positions and track their trajectories using the free python package trackpy [130].

4.1.3 Lively dynamics in a chiral colloidal fluid

The macroscopic flow of our chiral fluid is reminiscent of free surface flows of Newtonian fluids: nearby droplets merge (Fig. 4.1d), fluid spreads on a surface under the influence of gravity (Fig. 4.1e), voids collapse (Fig. 4.1f), and thin streams go unstable, as revealed by flowing fluid past a solid object (Fig. 4.1g). We demonstrate that these seemingly familiar features are accompanied by unique free surface flows. We then exploit the odd interfacial dynamics of this prototypical chiral liquid to infer its material constants, which remain out of reach of conventional rheology. In contrast to Newtonian fluids, the surface of our fluid supports a spontaneous unidirectional edge flow in its rest state, as well as unusual morphological dynamics such as the rotation of asymmetric droplets.

To investigate these lively surface flows, we first look at surface excitations in a simple slab geometry, as shown in Fig. 4.5a. We measure the spectrum of surface fluctuations, $|h(k,\omega)|^2$, by tracing the height profile, $h(x,t)$, of the surface and Fourier-transforming it in space and time. We observe the spectrum to be peaked along a curve $\omega(k)$, revealing the existence of dispersive waves (see Fig. 4.5b). The curve has only one branch with odd parity, meaning that the waves are unidirectional. This behavior contrasts that of conventional surface waves that propagate in all directions.

4.2 Hydrodynamics of a chiral colloidal fluid

These surface waves beg a hydrodynamic description. Building on previous work [131, 132, 133, 107, 134, 113, 109, 110],we describe our system with a continuum hydrodynamic theory. The hydrodynamic variables are the mass density of spinners $\rho(\mathbf{x},t)$, the momentum density

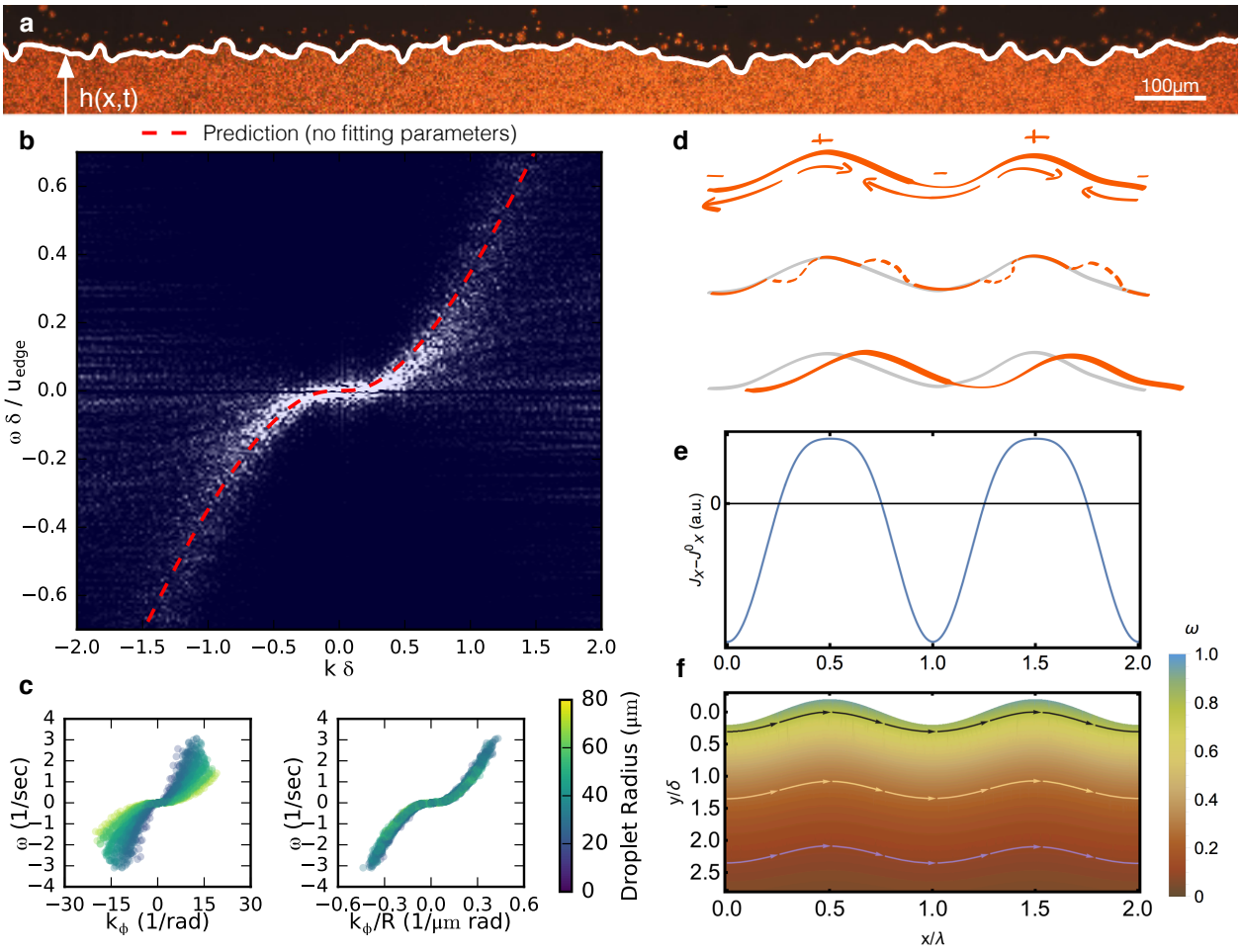

Figure 4.5: **Surface waves in a chiral spinner fluid.** (a) Surface waves are excited by perturbing a strip of the spinner fluid. To characterize them, we track the height profile of the strip in time, $h(x,t)$. (b) The resulting power spectrum from these waves $\langle|h(k,\omega)|\rangle$ is plotted versus the normalized wave vector $k\delta$ and frequency $\omega/(u_{\text{edge}}/\delta)$. The spectrum is peaked on a curve corresponding to the dispersion relation of the waves. Shown with the red dashed line is the theoretical prediction for the dispersion relation, obtained with the hydrodynamic parameters that we measure in Fig. 4.6. (c) The power spectrum $\omega(k)$ for surface waves on a perturbed circular droplet of spinner fluid (left panel) can be collapsed (right panel) by rescaling the angular wavenumber k by the droplet radius R. (d) Sketch of the mechanism for wave propagation. The propagation of waves can be understood by considering the mass flux, plotted in **e**. The chiral fluid is displaced from the high curvature to the low curvature regions. This process explicitly breaks the left-right symmetry, thereby propagating surface waves along only one direction. (e) Correction to the net mass flux along the interface due to a sinusoidal height perturbation, $J_x - J_x^o$, where J_x^o is the mass flux in a flat strip and J_x is the mass flux in the presence of a perturbation. **f,** Predicted vorticity field from the chiral-hydrodynamic model.

$\rho(\mathbf{x},t)u_i(\mathbf{x},t)$ and the angular momentum density $I_0\Omega(\mathbf{x},t)$, where I_0 is the spinner moment of inertia density. The conservation of momentum, angular momentum, and mass yields two-dimensional hydrodynamic equations. The first is conservation of mass:

$$\left(\partial_t + \mathbf{u}\cdot\nabla\right)\rho = -\rho\nabla\cdot\mathbf{u}$$

We will assume incompressibility in the following, reducing the above to

$$\nabla\cdot\mathbf{u} = 0 \tag{4.1}$$

The second is conservation of momentum. For a 2D homogeneous and isotropic fluid in contact with a solid substrate, it takes the generic form:

$$\rho\left(\partial_t + \mathbf{u}\cdot\nabla\right)u_i = \eta\nabla^2 u_i - \partial_i p + \eta_R\epsilon_{ij}\partial_j\left(2\Omega - \omega\right) - \Gamma_u u_i + \eta_o\nabla^2\epsilon_{ij}u_j,$$

where ϵ_{ij} is the Levi-Civita symbol, p is the pressure, $\omega = \hat{\mathbf{z}}\cdot(\nabla\times\mathbf{u}) = \epsilon_{ij}\partial_i u_j$ is the vorticity (which in two dimensions is a scalar), η is the shear viscosity, η_R is the rotational viscosity, η_o is a pseudo-scalar material parameter known as the Hall viscosity (or odd viscosity) [134], and $\Gamma_u u_i$ the frictional force with the substrate. η_R captures the rotational friction between neighboring particles [131, 135, 107, 112]. This odd stress builds up as the local spinning rate Ω deviates from half the local fluid vorticity $\omega = \hat{z}\cdot(\nabla\times v)$. In torque-free fluids, angular momentum conservation constrains these two quantities to be equal. As explained below, η_R and η_o are unique to chiral fluids.

We note that there is no direct appearance of the magnetic field or its stresses in this hydrodynamic description unlike in conventional ferrofluids. In this respect, our colloidal chiral fluid can be seen as a special type of driven ferrofluid in which the only role of magnetic forces is to induce chirality.

The dimensions of each quantity are: $[u] = L/T$, $[p] = M/T^2$, $[\rho] = M/L^2$, $[\omega] = 1/T =$

$[\Omega]$, $[\Gamma_u] = M/(L^2T)$, $[\eta] = [\eta_R] = [\eta_o] = M/T$.

The third is conservation of angular momentum:

$$I_0 \left(\partial_t + \mathbf{u} \cdot \nabla\right) \Omega = -I_0 \Omega \nabla \cdot \mathbf{u} - \Gamma^{\Omega} \Omega - 2\eta_R \left(2\Omega - \omega\right) + D_{\Omega} \nabla^2 \Omega + \tau,$$

where Γ^{Ω} is the rotational friction, D_{Ω} is the angular momentum diffusion constant, and τ the torque density field experienced by the spinners. The dimensions of each quantity are: $[I_0] = M$, $[D_{\Omega}] = ML^2/T$, $[\Gamma^{\Omega}] = M/T$, $[\tau] = M/T^2$.

To estimate the relative contributions of each term, we interpret its role and estimate its magnitude by dimensional analysis. η and η_R both originate in the stresses nearby particles exert on each other, principally through the lubrication layer that separates them. Their value will therefore be comparable to η_{H_20}, up to a geometric factor and the ratio of the densities of the spinner fluid and water. Our measurements confirm this. η_o also originates from the stresses nearby particles exert on each other but also depends on the extent of time-reversal symmetry breaking and is less straightforward to estimate. In theoretical studies of vortex fluids [109], electrons in magnetic fields [136, 137, 138], and fluids of chiral grains [110], $\rho\eta_o$ is proportional to the angular momentum per particle but we are not aware of a similar estimate in over-damped systems. We find from our measurement that η_o at typical frequencies of $\sim 10\,\mathrm{Hz}$ is comparable in magnitude to η. $(\Gamma_u/\rho)^{-1}$ corresponds to the time required to damp the linear motion of an individual colloid. From the sedimentation measurements this is $< 10^{-6}\,\mathrm{s}$. γ is estimated by U_{int}/a, where U_{int} is the time-averaged interaction potential between the hematite magnetic dipoles, $U_{\mathrm{int}} \sim \mu_0 \mu^2/a^3$, a is the typical particle spacing, and μ is the dipole moment. This approximation yields $\gamma \sim 10^{-13}\,\mathrm{N}$, which is consistent with measurements.

If we take as a characteristic velocity $\Omega\delta$ and characteristic gradient $1/\delta$, we find that the ratio of the material derivative term on the LHS to terms on the RHS is $< 10^{-2}$. We thus neglect the material derivative terms on the LHS of the momentum and angular momentum

equations.

Because our colloids are birefringent, we are able to measure their individual spinning rate by imaging through crossed polarizers. We find that all particles rotate at the same rate, Ω, which is set by the rotating magnetic field (see Fig. 4.6a). From this it follows that the particles' rotational inertia is negligible; the torque exerted on each particle by the magnetic field instantly adjusts to balance the frictional torques exerted by the neighboring particles and the solid substrate. This fast response enables the decoupling of the angular momentum equation from the momentum equation. Assuming constant spinning frequency $\Omega \equiv \Omega_0$, together with constant density $\rho \equiv \rho_0$, simplifies the problem considerably. The momentum equation becomes:

$$\eta \nabla^2 u_i - \partial_i \tilde{p} + \eta_R \epsilon_{ij} \partial_j \left(2\Omega - \omega\right) - \Gamma_u u_i = 0 \tag{4.2}$$

where $\tilde{p} = p + \eta_o \omega$ absorbs the bulk effects of Hall viscosity in an incompressible fluid. The bulk momentum equation is thus simply a Brinkman equation, as arises in modeling porous medium flow, with forcing by an anti-symmetric stress. The angular momentum equation (using $\nabla \cdot \mathbf{u} = 0$) reduces to:

$$\frac{1}{2}\Gamma^{\Omega}\Omega + \eta_R \left(2\Omega - \omega\right) = \frac{\tau}{2} \tag{4.3}$$

In this system of equations the pressure instantly adjusts to maintain the divergence-free condition, while the torque τ adjusts to enforce constant rate of rotation. Hence, only the momentum equation, with the divergence-free condition, is required to compute the bulk flow. Given a constant 2Ω, and using that $-\epsilon_{ij}\partial_j \omega = \nabla^2 u_i$, yields

$$\delta^2 \nabla^2 \mathbf{u} - \nabla \bar{p} - \mathbf{u} = \mathbf{0} \tag{4.4}$$

or an (apparently) unforced Brinkman equation, where $\delta = ((\eta + \eta_R)/\Gamma_u)^{1/2}$ is the so-called

hydrodynamic length, and $\bar{p} = \tilde{p}/(\Gamma_u)$. Note that the pressure satisfies $\nabla^2\tilde{p} = 0$. Taking the curl and using the divergence-free condition yields

$$\delta^2\nabla^2\omega - \omega = 0. \tag{4.5}$$

This Helmholtz equation indicates that the vorticity generated at the surface decays exponentially into the fluid, with a characteristic penetration depth δ (see Figs. 4.6c, d, g). In this model, the absence of substrate friction causes the penetration depth to diverge, resulting in rigid-body rotation of the entire fluid, as observed in ferrofluid droplets [139]. Both the Brinkman and Yukawa equations are solved as boundary value problems.

To consider free-surface flows, let D denote the chiral fluid domain in the plane, having boundary ∂D with outward facing normal $\hat{\mathbf{n}}$. If $\mathbf{v}$ is the velocity of ∂D, then we adopt the kinematic boundary condition

$$\mathbf{v} = \mathbf{u}|_{\partial D}, \tag{4.6}$$

giving that the boundary moves with the fluid velocity. We also assume the stress balance equation:

$$\boldsymbol{\sigma}\hat{\mathbf{n}}|_{\partial D} = \gamma\kappa\hat{\mathbf{n}} \tag{4.7}$$

where γ is the surface tension and κ is the curvature of ∂D. The stress tensor $\boldsymbol{\sigma}$ is given by:

$$\sigma_{ij} = -p\delta_{ij} + \eta_R\epsilon_{ij}\left(2\Omega - \omega\right) + 2\eta\frac{1}{2}\left(\partial_i u_j + \partial_j u_i\right) + \eta_o\left(\partial_i\epsilon_{jk}u_k + \epsilon_{ik}\partial_k u_j\right) \tag{4.8}$$

$$= -\left(p - \eta_o\omega\right)\delta_{ij} + \eta_R\epsilon_{ij}\left(2\Omega - \omega\right) + 2\eta\frac{1}{2}\left(\partial_i u_j + \partial_j u_i\right) - \eta_o O_{ij} \tag{4.9}$$

where:

$$O_{ij} = \begin{pmatrix} -2\partial_y u_x & +2\partial_x u_x \\ -2\partial_y u_y & +2\partial_x u_y \end{pmatrix} \tag{4.10}$$

Eqs. (4.1, 4.4, 4.6, 4.7) are a closed set determining the dynamics of the chiral fluid domain. It is solved as a free-boundary problem, with boundary conditions Eq. (4.7) deter-

mining the instantaneous velocity field through solution of Eqs. (4.1, 4.4). The boundary is then evolved via the kinematic boundary condition Eq. (4.6).

Comments

A few comments are in order:

- While the local stress in our colloidal chiral fluid differs from the local stress in a Newtonian fluid, the resulting flow Eq. (4.4) reduces to that of a Newtonian Brinkman fluid, implying that the bulk dynamics of Newtonian fluids and odd stress fluids are indistinguishable. The difference in the flows, and in particular the presence of surface edge-flows, arises from the difference in the stress at the boundary.

- The presence of an odd stress necessitates the application of a body torque by the following argument. Consider an infinitesimal region of characteristic size ℓ; the torque τ_k on this region is proportional to $\epsilon_{kij}\sigma_{ij}\ell^3$. The moment of inertia about the axis $\hat{x}_k$ is proportional to $\rho\ell^5$. Thus angular momentum conservation implies infinite acceleration as $\ell \to 0$. This implies that in the absence of a body torque there can be no antisymmetric component to the stress.

- The presence of an odd stress in Eq. (4.4) breaks the invariance under parity transformations of the equations of motion. This can be seen by the following argument. Consider Eq. (4.4), keeping in mind that it models a 2D fluid embedded in three-dimensional space:

$$\eta\nabla^2 u_i - \partial_i p + \eta_R \hat{z}_k \epsilon_{kij} \partial_j \left(2\Omega - \hat{z}\cdot\nabla\times u_i\right) - \Gamma_u u_i = 0$$

  where u_i has no component in the $\hat{z}$ direction and is a function of (x, y) alone. Under

the parity transformation $(x, y, z) \to (x, y, -z)$ the equation becomes:

$$\eta\nabla^2 u_i - \partial_i p + \eta_R \hat{z}_k \epsilon_{kij} \partial_j \left(-2\Omega - \hat{z} \cdot \nabla \times u_i\right) - \Gamma_u u_i = 0$$

demonstrating that if one does not also reverse the direction of spin of the colloids, the equation is in general not invariant. Of course in the case of constant spinning motion in which the parity breaking term vanishes, the flow equation is parity invariant. Parity remains, however, broken by the corresponding stress boundary condition.

- The presence of a Hall viscosity η_o in Eq. (4.4) stems from the breaking of time-reversal symmetry in two dimensions [134, 113]. In theoretical studies of vortex fluids [109], electrons in magnetic fields [136, 137, 138] and fluids of chiral grains [110], $\rho\eta_o$ was shown to be proportional to the angular momentum per particle (or vortex circulation), but we are not aware of an estimate in active over-damped systems.

- In an incompressible fluid, Hall viscosity has no effect in the bulk, only on the boundary. As shown in Eqs. (4.8) and (4.9), the Hall stress tensor can be divided into a quantity with divergence that can be absorbed in the pressure and a component $-\eta_o O_{ij}$ which is divergence free: $\partial_j O_{ij} = 0$. The former has no effect in an incompressible fluid, however the latter gives rise to stresses on the boundary. In particular, using $O_{ij} n_j = -2\partial_s u_j$:

$$\sigma_o \mathbf{n} = -2\eta_o \partial_s \mathbf{u} = -2\left(\partial_s u_s - \frac{u_n}{R}\right)\hat{\mathbf{s}} - 2\left(\partial_s u_n + \frac{u_s}{R}\right)\hat{\mathbf{n}}$$

where R denotes the surface radius of curvature with the convention that a circular droplet has a positive radius of curvature. From this it can be seen that Hall viscosity acts purely on the boundary, generating boundary stresses in proportion to variations of the surface flow *along* the boundary.

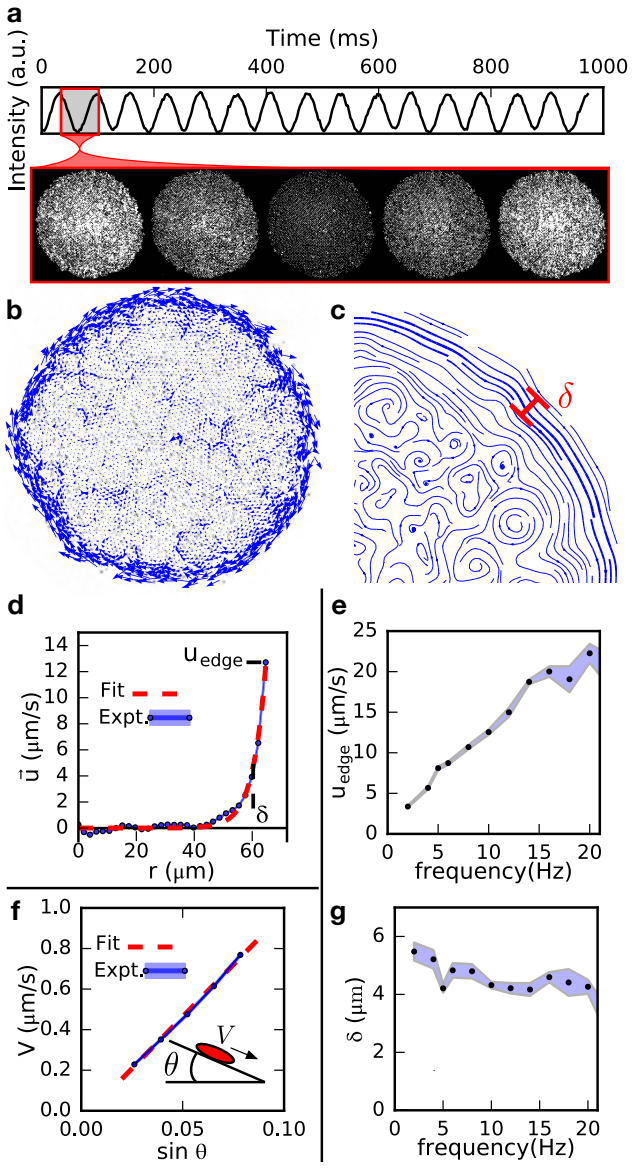

Figure 4.6: **Characterization of a droplet of chiral spinner fluid.** (a) When viewed through crossed polarizers, the particles blink as they spin. This allows us to confirm that they all spin at the same frequency, set by the rotating magnetic field. (b) By measuring the velocity of each particle within a cluster, we find a flow profile that is concentrated at the edge within a penetration layer δ shown in **c, d,** and **g**. (c) A zoomed-in view of the flow streamlines, obtained by averaging several instantaneous velocity profiles such as the one shown in **b**. (d) By measuring the flow profile, the edge current u_{edge} and penetration depth δ are extracted. **e, g,** By measuring the flow profile $u(r)$ at a range of frequencies, we extract the shear viscosity, η, and rotational viscosity, η_R, in terms of the substrate friction, Γ_u. **f,** Finally, by tilting a sample and measuring the sedimentation velocity of a droplet, we extract the substrate friction.

4.3 Characterizing the fluid

To make a quantitative comparison between our model and the flows we observe, we require a measurement of the hydrodynamic and friction coefficients η, η_{R}, η_{o}, and Γ_u. In what follows, we show that each of these coefficients can be experimentally measured.

4.3.1 Substrate friction

We measure the substrate friction, Γ_u, by observing droplets of spinner fluid sediment along a tilted substrate (see Figure 4.6**f**). The sedimentation speed v_{sed}, the tilt angle of the substrate φ, and Γ_u are simply related by the force balance equation:

$$\Gamma_u v_{\mathrm{sed}} = \rho g \sin\varphi \tag{4.11}$$

where g is the gravity acceleration and the density ρ is computed by dividing the mass of a particle by the average Voronoi cell area around a particle. We find, on a glass substrate,

$$\Gamma_{u,\mathrm{glass}} = 2.49 \pm 0.03 \times 10^3 \text{ Pa s/m}.$$

A similar experiment is performed for particles sedimented to soft interfaces. For curved droplets, we only measure v_{sed} over sufficiently small displacements such that particle trajectories are linear. This yields a substantially reduced substrate friction at air interfaces,

$$\Gamma_{u,\mathrm{air}} = 46.1 \pm 0.5 \text{ Pa s/m}.$$

At oil interfaces, we find Γ_u to increase with viscosity between $\Gamma_{u,\mathrm{air}}$ and $\Gamma_{u,\mathrm{glass}}$, as seen in Figure 4.11.

4.3.2 Velocity profile and rotational and shear viscosities

We also measure the rotational and shear viscosities of the spinner fluid. We infer them from the vorticity profile in axisymmetric droplets. Practically, these quantities can be extracted by measuring how the velocity component tangent to the edge of a droplet varies in the direction normal to the edge of the droplet. We construct the velocity field of the spinner fluid from the instantaneous velocities of the particles, using a bin size of 2–4 microns.

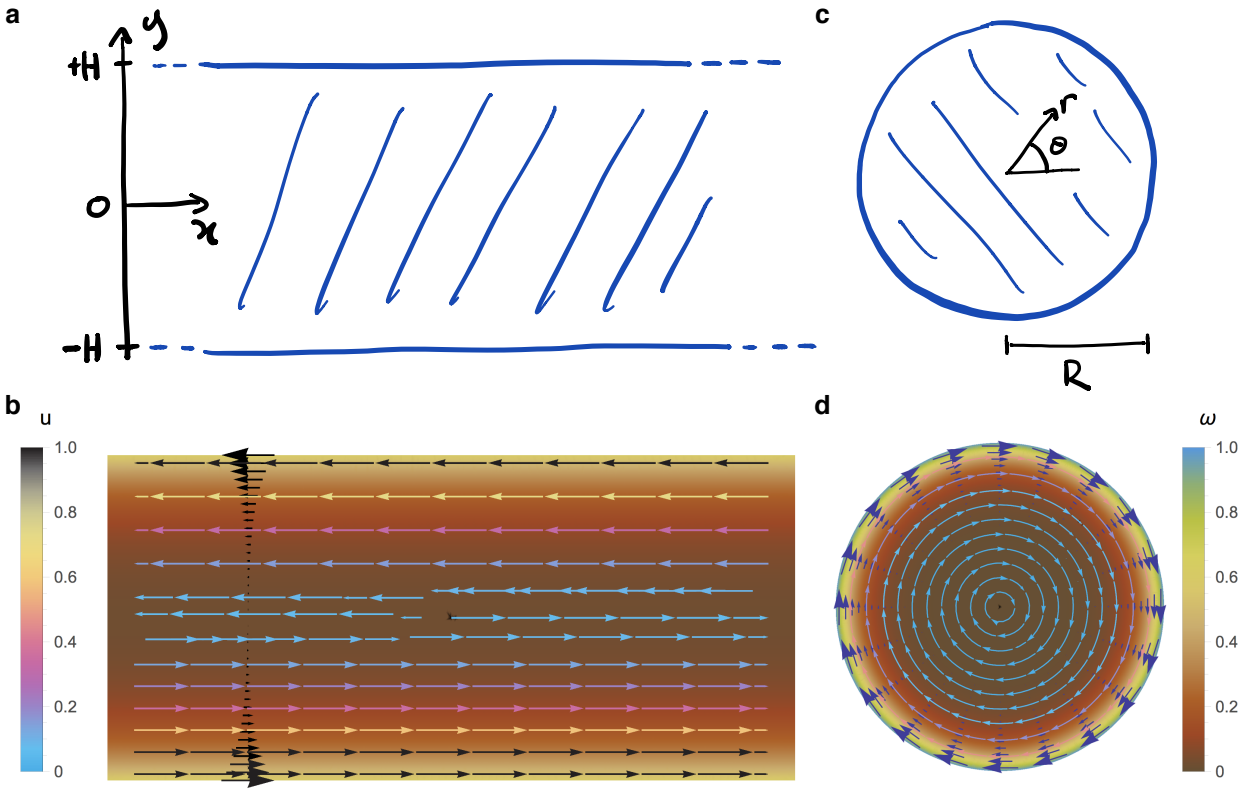

Figure 4.7: **The geometry of steady edge currents in a circular droplet and in a slab of chiral fluid. a**, Setting variables describing a chiral fluid slab of thickness $2H$. **b**, Chiral fluid flow field within the slab. **c**, Setting variables describing a circular chiral fluid droplet of radius R. **d**, Chiral fluid flow field in the droplet. In **b** and **d** the background color represents the magnitude of vorticity and the arrows represent the direction of flow, colored by the velocity magnitude. Note that in both cases, the flow speed drops exponentially to zero as we move away from the boundary.

We fit the radial velocity profile to a functional form obtained from the hydrodynamic

equations. Assuming a circular droplet of chiral fluid with radius R, as depicted in Figure 4.7c, with an azimuthally symmetric flow field $\mathbf{u} = u(r)\hat{\theta}$, we have for the radial component of the pressure: $\partial_r p(r) = 0$ and for the azimuthal component of the momentum equation:

$$r^2\partial_r^2 u + r\partial_r u - \left(1 + \frac{1}{\delta^2}r^2\right)u = 0$$

which is satisfied by $u(r) = AI_1(r/\delta)$, where I_k is a modified Bessel function of the first kind of order k. The boundary conditions $\sigma\hat{\mathbf{r}} = -\frac{\gamma}{R}\hat{\mathbf{r}}$ then fixes the constants p and A giving:

$$p = \frac{\gamma}{R} + \eta_o\frac{u(R)}{R} + p_0$$

and

$$u(r) = \frac{\eta_R I_1(r/\delta)}{\eta I_2\left(\frac{R}{\delta}\right) + \eta_R I_0\left(\frac{R}{\delta}\right)}2\Omega\delta \tag{4.12}$$

for $0 \leq r \leq R$.

We point out that ω_{edge} is directly proportional to η_R, which demonstrates the importance of odd stress for the dynamics.

A typical velocity profile, along with a best fit, is shown in Figure 4.6. From this fit we extract the shear viscosity η, and rotational viscosity η_R (see Figure 4.8). We find:

$$\eta_{\text{glass}} = 4.9 \pm 0.2 \times 10^{-8} \text{ Pa m s}$$

$$\eta_{R,\text{glass}} = 9.1 \pm 0.1 \times 10^{-10} \text{ Pa m s.}$$

Using these values above, we infer a penetration depth of

$$\delta_{\text{glass}} = 4.5 \pm 0.1\,\mu\text{m},$$

which corresponds to $\sim$2 particle layers. Figure 4.9 shows $u_{edge}/2\Omega\delta$ measured for different

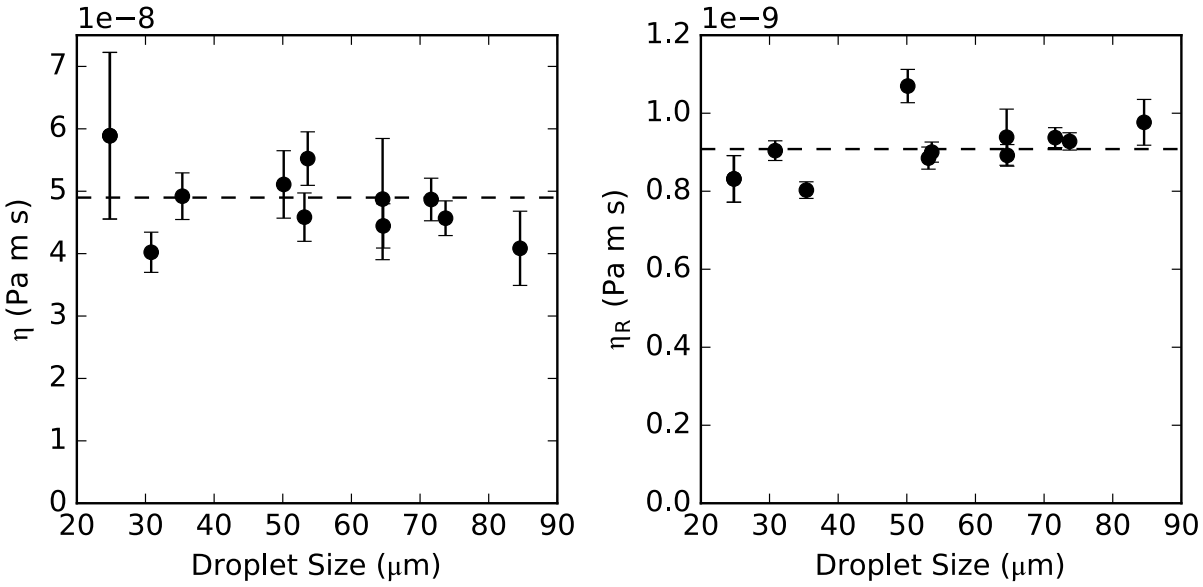

Figure 4.8: **Measurement of viscosities.** By fitting the tangential velocity profiles to Eq. (4.12), we measure the ordinary and rotational viscosities for a distribution of droplets larger than 4 penetration depths composed of particles spinning at 10 Hz. The dashed line shows the mean values.

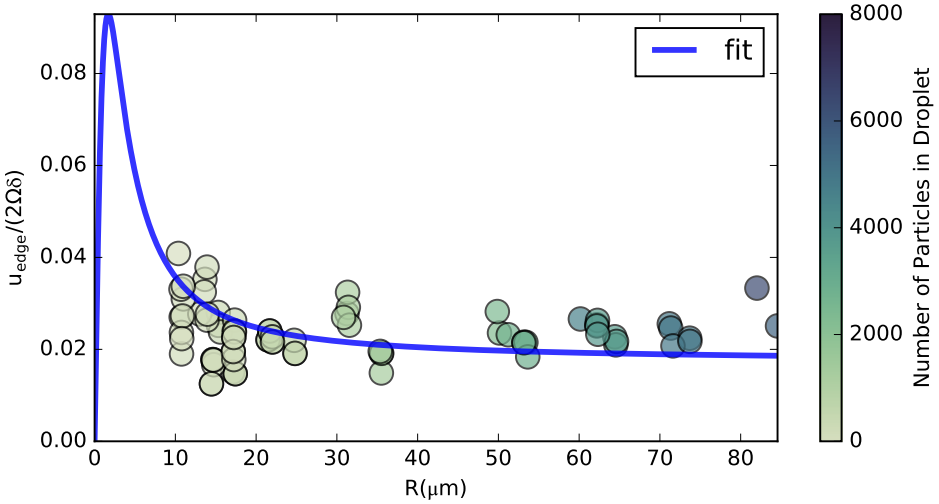

Figure 4.9: **Extracting viscosities from velocity profiles.** We collect velocity profiles from droplets of spinner fluid and we extract the edge current velocity u_{edge} and penetration depth δ. The figure shows $u_{edge}/2\Omega\delta$ plotted against the droplet radius, R, for each droplet.

droplet sizes. For a droplet of radius $R = 50\ \mu$m with particles spinning at 10 revolutions per second, we obtain an edge velocity $u_{\text{edge}} = u(R) = 11.7 \pm 0.2\,\mu$m/s.

At low-friction interfaces, the delocalized edge flow in the chiral fluid induces a background rotation by dragging the interface with it. We therefore add a rigid body rotation term of the form $\Omega_R r$ to our theoretical prediction for the tangential velocity profile. A sample fit, analogous to the profile provided for a droplet on a glass substrate (Figure 3d), demonstrates agreement to this form (see Figure 4.10a). We observe agreement between this procedure and a rigorous treatment of the flow profile incorporating the interaction of the chiral fluid with an interface, which we postpone to future work. Fitting to the form $u(r) + \Omega_R r$, we find a background rotation rate of $\Omega_R \sim 0.66\,1/$s and parameter estimates:

$$\eta_{\text{air}} = 2.5 \pm 0.4 \times 10^{-8}\ \text{Pa m s}$$

$$\eta_{R,\text{air}} = 9.5 \pm 0.1 \times 10^{-10}\ \text{Pa m s}.$$

These viscosity estimates are close to those on air, but Γ_u is significantly decreased. Accordingly, we find a penetration depth of

$$\delta_{\text{air}} = 23.8 \pm 0.2\,\mu\text{m},$$

which demonstrates the delocalization of the edge current illustrated in Figure 4b.

We perform this fitting procedure for velocity profiles at oil interfaces of variable viscosity, again finding good agreement to the theory with an additional rigid body component. As the viscosity is increased, we expect a damping of the background fluid rotation. This expectation is supported by the decrease in the fit for Ω_R with increasing viscosity, as shown in Figure 4.10b. With this fitting approach, we find edge current localization to increase with the viscosity of the oil phase, as shown in Figure 4.11.

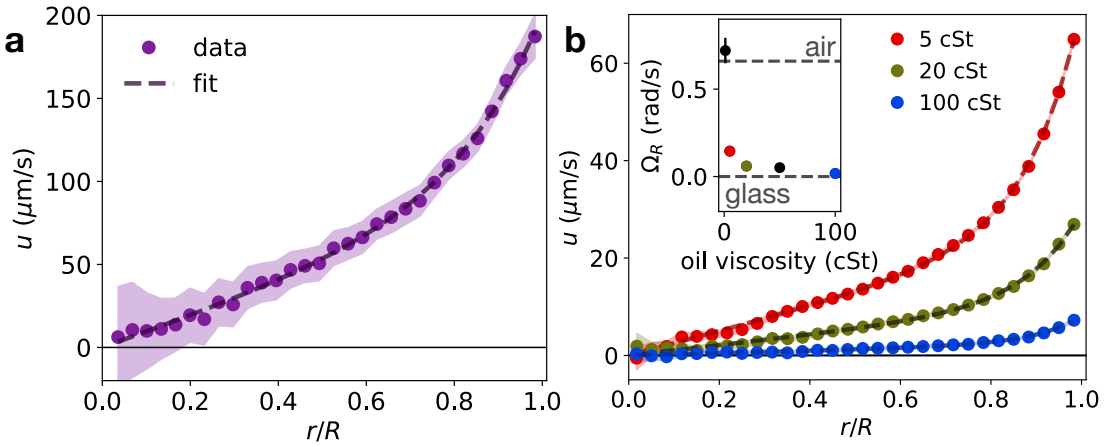

Figure 4.10: **Velocity profiles with background rotation.** (a) On a low-friction substrate, like the air-water interface, the edge current is delocalized (c.f. Figure 4b). To extract hydrodynamic parameters from the associated tangential velocity profile, $u(r)$, we fit to the radial theory (Eq. (4.12)) with an additional rigid body rotation rate, yielding a good fit. (b) A similar procedure accurately fits velocity profiles at oil interfaces, with both the velocity and the rigid body contribution decreasing with increasing viscosity.

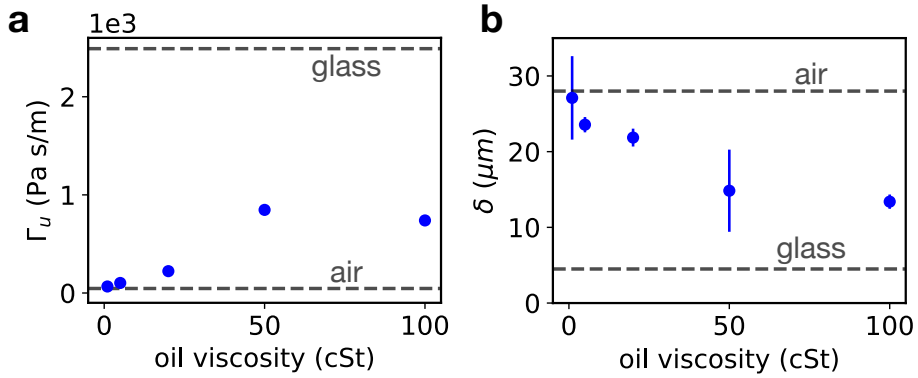

Figure 4.11: **Tuning the substrate friction.** (a) The spinner fluid sits at an interface with oil of viscosity that we can control. By increasing the viscosity, we increase the substrate friction, and (b) decrease the penetration depth, partially spanning the region between the air and glass extremes.

4.4 Chiral surface waves and 'edge pumping'

Equipped with the hydrodynamic coefficients we can now investigate the origin of the surface waves within our model. In order to do this, we perform a linear stability analysis of the hydrodynamics equations.

4.4.1 Perturbation of flow in a semi-infinite slab

In this section, we outline a calculation of the response of the otherwise flat interface of a chiral fluid that occupies the region $y \leq 0$.

Steady state solution

Consider a chiral fluid that occupies the region $y < 0$ of a plane. It is easy to verify that the following expression for ω satisfies the bulk equation (Eq. (4.5)):

$$\omega = \frac{\eta_R}{\eta + \eta_R} 2\Omega e^{y/\delta}. \tag{4.13}$$

for $|y| \leq 0$. The corresponding velocity has a non-zero component only in the $\hat{\mathbf{x}}$ direction and can be obtained by direct integration:

$$u_x = -\frac{\eta_R}{\eta + \eta_R} 2\Omega\delta e^{y/\delta}$$

The kinematic boundary condition is satisfied as there is no vertical component to the velocity. The normal stress boundary condition reduces to $\sigma_{yy} = p = p_0$ where p_0 is the pressure outside the slab which can be set to zero. The tangential stress boundary condition reduces to: $\sigma_{yx} = 2\eta_R\Omega - (\eta + \eta_R)\omega|_{y=\pm H} = 0$, which is satisfied by Eq. (4.13).

Linearization scheme

Consider a flat interface at $y = 0$ which we perturb with a zero-mean perturbation $y = h(x,t) = \varepsilon g(x,t)$ with $\varepsilon << 1$. We represent the steady-state velocity, vorticity, and stress

fields as $\bar{\mathbf{u}} = (\bar{u}, \bar{v})$, $\bar{\omega}$, and $\bar{\sigma}$, respectively, and introduce perturbations as

$$\begin{aligned} u(x,y) &= \bar{u}(y) + \varepsilon\tilde{u}(x,y) \\ v(x,y) &= \varepsilon\tilde{v}(x,y) \\ \omega &= \bar{\omega}(y) + \varepsilon\tilde{\omega}(x,y) \\ \boldsymbol{\sigma} &= \bar{\boldsymbol{\sigma}}(y) + \varepsilon\tilde{\boldsymbol{\sigma}}(x,y) \\ p &= \varepsilon q(x,y) \end{aligned}$$

Linear theory

Within this linearization scheme, the linearized equations and boundary conditions for the perturbed slab can be derived as follows.

Linearized bulk equations The linearized bulk equations are simply given by:

$$\left(\bar{\eta}\nabla^2 - \Gamma_u\right)\tilde{u}_i = \partial_i q \quad \text{and} \quad \nabla\cdot\tilde{\mathbf{u}} = 0 \tag{4.14}$$

where $\bar{\eta} = \eta + \eta_R$.

Linearized stress boundary conditions The stress boundary conditions relate the bulk fields to interfacial data. We take an upward normal $\hat{\mathbf{n}} \approx \hat{\mathbf{y}} - \varepsilon g_x\hat{\mathbf{x}}$ and the RHS of Eq. (4.7) is to linear order $\gamma\kappa\hat{\mathbf{n}} \approx \varepsilon\gamma g_{xx}\hat{\mathbf{y}}$. Expanding Eq. (4.7) to linear order, and using that $\bar{\sigma}(0)\hat{\mathbf{y}} = \mathbf{0}$ yields

$$\tilde{\boldsymbol{\sigma}}(x,0)\hat{\mathbf{y}} = \gamma g_{xx}(x)\hat{\mathbf{y}} + g_x(x)\bar{\boldsymbol{\sigma}}(0)\hat{\mathbf{x}} - g(x)\bar{\boldsymbol{\sigma}}_y(0)\hat{\mathbf{y}}$$

After some simplification we obtain:

$$\begin{aligned} &\bar{\eta}\tilde{u}_y(x,0) + (\eta - \eta_R)\tilde{v}_x(x,0) + 2\eta_o\tilde{u}_x(x,0) = \bar{\eta}\bar{\omega}_y(0)\,g(x) + 2\eta_o\bar{\omega}(0)g_x(x) \\ &2\eta\tilde{v}_y(x,0) - q(x,0) + 2\eta_o\tilde{v}_x(x,0) = \gamma g_{xx}(x) - \left[(\eta - \eta_R)\,\bar{\omega}(0) + 2\eta_R\Omega\right]g_x(x) \end{aligned} \tag{4.15}$$

Linearized kinematic boundary condition The linearized kinematic boundary condition is given by:

$$g_t + \bar{u}\,(0)\, g_x = \tilde{v}\,(x, 0) \tag{4.16}$$

Solution

To solve Eqs. (4.14, 4.15, 4.16) we make use of Fourier transforms in the x direction to take advantage of translational invariance.

Solution of the linearized bulk equations Taking the Fourier transform in x:

$$\bar{\eta}\left(\partial_{yy} - k^2\right)\tilde{\mathbf{u}} - \Gamma_u\tilde{\mathbf{u}} - \left(ik, \partial_y\right) q = \mathbf{0} \;\text{ and }\; \left(ik, \partial_y\right)\cdot\tilde{\mathbf{u}} = 0$$

Using that $\left(\partial_{yy} - k^2\right) q = 0$ we obtain:

$$\begin{aligned}
q &= Ae^{|k|y} \\
\tilde{u} &= -\frac{ik}{\bar{\eta}}\delta^2 Ae^{|k|y} + Be^{|\star|y} \\
\tilde{v} &= -\frac{|k|}{\bar{\eta}}\delta^2 Ae^{|k|y} - \frac{ik}{|\star|}Be^{|\star|y} \\
\tilde{u}_y &= -\frac{ik\,|k|}{\bar{\eta}}\delta^2 Ae^{|k|y} + |\star|\,Be^{|\star|y} \\
\tilde{v}_y &= -\frac{|k|^2}{\bar{\eta}}\delta^2 Ae^{|k|y} - ikBe^{|\star|y}
\end{aligned} \tag{4.17}$$

Where $\star^2 = k^2 + \delta^{-2}$. The coefficients A and B are to be determined from the boundary conditions.

Application of the stress boundary conditions Inserting Eq. (4.17) into the linearized stress boundary conditions, Eq. (4.15), yields:

$$\begin{aligned}\left[-2ik\,|k|\,\delta^2\frac{\eta}{\bar{\eta}}+2k^2\delta^2\frac{\eta_o}{\bar{\eta}}\right]A+\left[\frac{2\eta k^2+\bar{\eta}\delta^{-2}}{|\star|}+2ik\eta_o\right]B &= \left[\frac{\bar{\eta}}{\delta}+2ik\eta_o\right]\frac{\eta_R}{\bar{\eta}}\Omega g\\ \left[\left(1+2k^2\delta^2\frac{\eta}{\bar{\eta}}\right)+2ik|k|\delta^2\frac{\eta_o}{\eta}\right]A+\left[2ik\eta-2\eta_o\frac{k^2}{|\star|}\right]B &= \gamma k^2-2ik\eta_R\frac{\eta_R}{\bar{\eta}}\Omega g\end{aligned}$$

which is a set of two linear equations for the unknowns A, B in terms of the surface perturbation amplitude g.

Application of the kinematic boundary condition Combining this with the kinematic boundary condition:

$$g_t + ik\bar{u}g = \tilde{v}$$

and substituting $\tilde{v}$ we can then compute the time evolution of a surface perturbation. In the section that follows, we discuss this evolution in the case of a sinusoidal perturbation of the height $g \sim \mathrm{Re}\left[e^{ikx}\right]$.

Visualization and asymptotics

The evolution of the surface corresponding to an infinitesimal sinusoidal perturbation of the height $g \sim \mathrm{Re}\left[e^{ikx}\right]$ is given by $g \sim \mathrm{Re}\left[e^{i(kx+\omega t)}e^{\alpha t}\right]$ which corresponds to damped waves with dispersion $\omega(k\delta)$ and dissipation rate $\alpha(k\delta)$. Figure 4.12 shows typical wavenumber dependences $\omega(k\delta)$ and $\alpha(k\delta)$. From the anti-symmetry of the dispersion relation it can be seen that the surface waves are uni-directional. It is instructive to consider the long wavelength ($|k\delta| \ll 1$) and short wavelength ($|k\delta| \gg 1$) limits. The asymptotic expressions

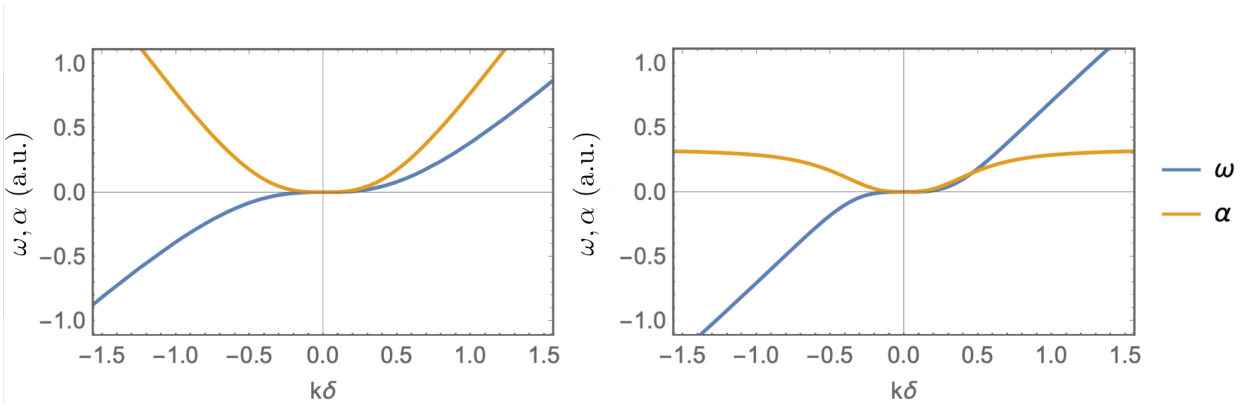

Figure 4.12: **Typical dependence of surface wave dispersion and dissipation on wavenumber** (a) The dispersion and dissipation in the absence of Hall viscosity and for finite surface tension (b) The dispersion and dissipation in the absence of surface tension in the presence of Hall viscosity. The wavenumber dependence of dispersion is generically $\propto k^n$ for odd $n \geq 3$ for small k and $\propto k$ for large k. Similarly, the wavenumber dependence of dissipation is generically $\propto |k|^n$ for odd $n \geq 3$ for small k and $\propto |k|$ for large k.

are given by:

$$\omega(k) = \begin{cases} 2u_{\text{edge}} \dfrac{\eta}{\Gamma_u} k^3 & |k\delta| \ll 1 \\ -\dfrac{2\eta_R(\eta+2\eta_R)\Omega}{\eta^2+4\eta\eta_R+\eta_o^2+4\eta_R^2} + \left[\dfrac{1}{2}\dfrac{\gamma\eta_o}{\eta^2+\eta_o^2}\dfrac{\left(\eta^2+2\eta\eta_R+\eta_o^2+2\eta_R^2\right)}{\left(\eta^2+4\eta\eta_R+\eta_o^2+4\eta_R^2\right)} + u_{\text{edge}}\right] k & |k\delta| \gg 1 \end{cases}$$

$$\alpha(k) = \begin{cases} \left[\dfrac{\gamma}{\Gamma_u} + \dfrac{2\eta_o u_{\text{edge}}}{\Gamma_u}\right] |k|^3 & |k\delta| \ll 1 \\ \dfrac{2\eta_o\eta_R\Omega}{(\eta+2\eta_R)^2+\eta_o^2} + \left[\dfrac{\gamma(\eta+\eta_R)}{2\left(\eta^2+\eta_o^2\right)}\dfrac{\left(\eta^2+2\eta\eta_R+\eta_o^2\right)}{\left(\eta^2+4\eta\eta_R+\eta_o^2+4\eta_R^2\right)}\right] |k| & |k\delta| \gg 1 \end{cases}$$

The dispersion relation at high wavenumbers (short wavelengths compared to δ) is generally linear, corresponding to waves with a constant speed, while at short wavenumbers (long wavelengths compared to δ) it scales with k^3. Similarly, the dissipation rate displays a transition at small wavenumbers from $|k|^3$ to a linear scaling at larger wavenumbers.

In order to gain insight on the physical origin of wave propagation and damping, it is instructive to consider the independent contributions of inter-rotor friction, odd viscosity

and surface tension to dispersion and dissipation.

$\eta_o = \gamma = 0,\ \eta_R \neq 0$ In this limit surface waves are undamped, as $\alpha(k) = 0$, and the dispersion relation is given simply by:

$$\omega(k) = \begin{cases} 2u_{\text{edge}}\dfrac{\eta}{\Gamma_u}k^3 & |k\delta| \ll 1 \\ -\dfrac{2\eta_R\Omega}{\eta + 2\eta_R} + u_{\text{edge}}k & |k\delta| \gg 1 \end{cases}$$

The physical origin of these freely propagating waves can be understood, in the long wavelength limit, in terms of a curvature-dependent resistance to the flow of the surface boundary layer, as discussed in Section 4.4.3. In the short wavelength limit, the linear dispersion corresponds to simple advection of perturbations by the edge current.

$\eta_o = 0,\ \gamma \neq 0,\ \eta_R \neq 0$ In this limit the dispersion relation is unchanged, but the surface fluctuations are now damped by surface tension:

$$\alpha(k) = \begin{cases} \dfrac{\gamma}{\Gamma_u}|k|^3 & |k\delta| \ll 1 \\ \dfrac{\gamma(\eta + \eta_R)}{2(\eta^2 + 2\eta\eta_R)}|k| & |k\delta| \gg 1 \end{cases}$$

Thus surface tension has a purely dissipative effect on surface waves. This is a consequence of the lack of inertia in our system: surface tension acts to flatten the interface which, once flattened, remains so.

$\eta_o \neq 0,\ \gamma = 0,\ \eta_R \neq 0$ As in the case for $\eta_o = 0$, the dispersion relation at large wavenumbers converges to a linear one with slope u_{edge} and only the intercept is modified to: $-\frac{2\eta_R(\eta+2\eta_R)\Omega}{\eta^2+4\eta\eta_R+\eta_o^2+4\eta_R^2}$ to reflect the dominant wave-propagating mechanism at play (edge

pumping or capillary-Hall driving). The dissipation, however, is strongly affected:

$$\alpha(k) = \begin{cases} \dfrac{2\eta_o u_{\text{edge}}}{\Gamma_u}|k|^3 & |k\delta| \ll 1 \\ \dfrac{2\eta_o \eta_R \Omega}{(\eta + 2\eta_R)^2 + \eta_o^2} & |k\delta| \gg 1 \end{cases}$$

In both limits, the Hall stress η_o in conjunction with the odd stress η_R damps the surface waves. At long wavenumbers the scaling is akin to that given by surface tension, but at large wavenumbers the scaling is wavenumber-independent. We discuss the origin of this damping in Section 4.4.3.

$\eta_o \neq 0,\ \gamma \neq 0,\ \eta_R = 0$ In this case, there is no edge current and the dynamics come from a balance of surface tension, Hall viscosity and substrate friction:

$$\omega(k) = \begin{cases} 4\dfrac{\gamma\eta_o}{\Gamma_u^2}\ k^5 & |k\delta| \ll 1 \\ \dfrac{1}{2}\dfrac{\gamma\eta_o}{\eta^2 + \eta_o^2}\ k & |k\delta| \gg 1 \end{cases}$$

and:

$$\alpha(k) = \begin{cases} \dfrac{\gamma}{\Gamma_u}|k|^3 & |k\delta| \ll 1 \\ \dfrac{1}{2}\dfrac{\gamma\eta}{\eta^2 + \eta_o^2}\ |k| & |k\delta| \gg 1 \end{cases}$$

which corresponds to damped unidirectional surface waves driven by a combination of surface tension and Hall viscosity. The driving mechanism for these waves can be understood in terms of a sequential mechanism in which surface tension drives a normal flow, and odd viscosity translates this into a propagation as discussed in Section 4.4.3.

The full dispersion is a combination of all these effects. Our unidirectional surface waves can be driven by differential drag on the boundary current or Hall viscosity acting in conjunction with surface tension. They are damped by surface tension and Hall viscosity

acting in concert with the boundary current.

4.4.2 Measurement of surface wave spectrum and dissipation

Equipped with a model for chiral surface waves, we now measure them precisely in experiment. We've seen that the wave dynamics are crucially sensitive to boundary layer flows. Therefore, we seek to vary the boundary length in order to explore its relative role. As we will show in what follows, an increase of the penetration depth of the boundary layer amplifies chiral effects and reveals the thus far experimentally inaccessible source of stress, Hall viscosity [113, 134, 140]. We thus perform experiments on glass, as well as soft substrates.

To measure the power spectrum, we excite surface waves on straight strips or nearly-circular droplets of chiral fluid, either by briefly rolling particles in the direction perpendicular to the fluid, or by letting nearby droplets merge with it. We then spin the particles for about 10 minutes and let the perturbations evolve in time. As the strip or circular droplet equilibrates, small nearby clusters may coalesce with it, resulting in additional excitations.

We identify the edges of the strip or circular droplet by thresholding the images and using Canny edge detection. For the strip geometry, we take the height profile to be the distance from a straight line which spans the strip to the strip's perturbed edge. For the circular geometry, we take the radial profile to be the distance from the circumference of the droplet to its center of mass. For high-friction experiments, we record this height or radial profile over time at a sample rate between 1 fps and 4 fps. For low-friction experiments, the dynamics are substantially faster, so we record the same profile at a rate between 25 fps and 50 fps. We then perform a fast Fourier transform (FFT) on this data. We square the absolute value of this FFT to obtain a power spectrum in frequency ω, and wavenumber k. To obtain the final power spectrum we normalize each slice in k by the average power in that slice.

The resulting power spectrum shows dissipative waves with a clear dispersion relation in both geometries, as shown in the left panel of Figure 4.13 and in Figures 2b,c and Figures

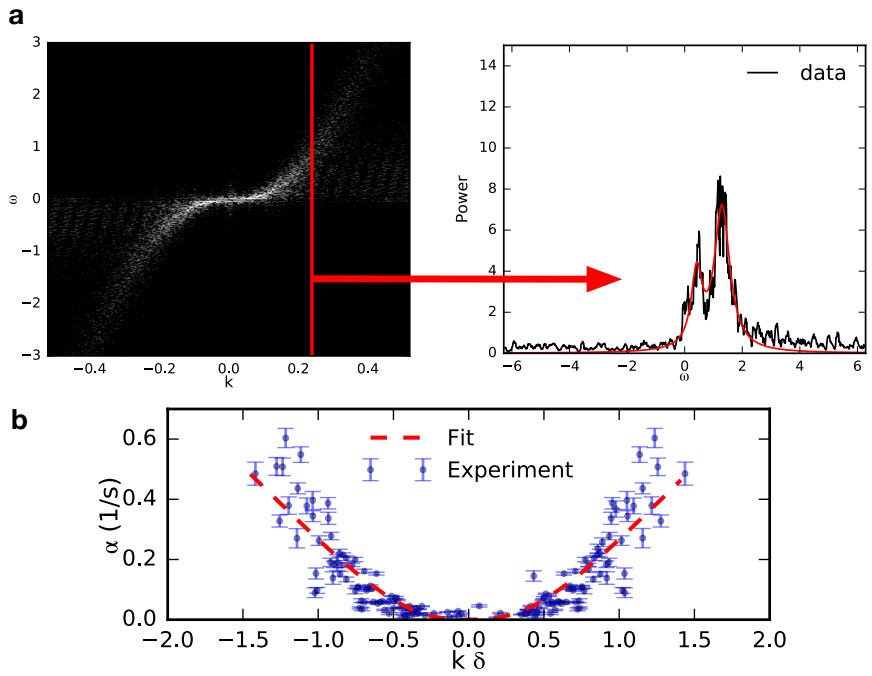

Figure 4.13: **Extracting wave dissipation rates from the power spectrum.** (a) By fitting each slice using the relation in Eq. (4.18) we obtain values for the dissipation α at each wavenumber k. (b) We fit these values to the analytical solution, to infer the fluid's surface tension. Shown with the red dashed line is a fit to the theoretical prediction for the damping rate of the chiral waves.

4a,b. Taking the form of excitations to be proportional to $e^{i\omega t-\alpha t}$, where ω characterizes the propagation of waves and α the dissipation, the power $P_k(\omega)$ at each k is given by the relation

$$P_k(\omega) \propto \frac{1}{\alpha^2 + [\omega - \omega(k)]^2}, \tag{4.18}$$

where the function $\omega(k)$ defines the dispersion relation of the linear waves.

There are often small background drifts in the chiral fluid which may result in a secondary linear feature in the power spectrum. While this additional feature varies between samples, the main dispersion curve remains unchanged. We thus fit the spectrum at each k to a sum of two peaks of the form in Eq. (4.18) (see also right panel in Figure 4.13a). By selecting the peaks closest to the dispersion curve, we obtain the value of α at each k, as shown in Figure 4.13b).

For low-friction experiments, we observe a background rotation of the chiral fluid (see Section 4.3.2). As a result, we correct $\omega(k)$ by subtracting the background rate of the interface, Ω_R, in Figure 4b. This correction does not have any effect on the dissipation of waves $\alpha(k)$ as it preserves the width of the spectra at each k.

As shown in Figs. 4.5 **b** and 4.14**a** and **b**, with no fitting parameters, our model shows excellent agreement with the experimentally measured dispersion relation.

Fitting the dissipation

By fitting $\alpha(k)$ to the full analytical solution for the dissipation ignoring contributions from η_o (see Section 4.4.1 for an asymptotic approximation in the strip geometry) we infer the surface tension of the fluid γ. At the glass interface and in the strip geometry, we find

$$\gamma_{\text{glass}} = 2.3 \pm 0.2 \times 10^{-13} \text{ N},$$

which is consistent with an estimate based on magnetic interactions between rotating dipoles (see Sec. 4.2).

We obtain the same result for a circular droplet geometry within measurement error. The fitted dissipation data are presented in Figure 4c (droplet) and Figure 4.13 (strip). When fitting to the full analytical solution for the dissipation adding contributions from η_o we obtain the same result for γ, with $\eta_{\mathrm{o,glass}} = 0.0 \pm 0.8 \times 10^{-9}$ Pa m s.

In the case of low surface friction air interfaces, however, we observe a distinct new feature in the dissipation rate: a leveling off of the dissipation rate at short wavelengths which cannot be accounted for by the hydrodynamic theory neglecting Hall viscosity. In this case, for a droplet geometry, we obtain

$$\gamma_{\mathrm{air}} = 4.69 \pm 0.07 \times 10^{-13} \text{ N},$$

$$\eta_{o,\mathrm{air}} = 1.4 \pm 0.1 \times 10^{-8} \text{ Pa m s}.$$

Disambiguating Hall viscosity and surface tension

The clearly visible decrease in slope in the damping relation is the most visible signature of Hall viscosity in our data and can be understood on dimensional grounds. In the long wavelength limit, the wave relaxation time is controlled by the competition of either surface tension or Hall stress with substrate friction. Dimensionally this implies a scaling $\alpha \sim |k|^3$ since the ratios γ/Γ_u and $\eta_o v_s/\Gamma_u$ have dimension of volume per unit time. In contrast, in the short wavelength limit, surface friction plays no role and damping stems from the competition of surface tension or Hall stress and bulk viscosities alone. In this case dimensional analysis requires linear scaling with wavenumber in the case of surface tension, and wavenumber independence in the case of Hall stress (see Sec 4.4.3). This change in wavenumber dependence brings about a visible rollover to a decreased slope in the wave damping rate.

Disentangling the relative role of Hall viscosity η_o and surface tension γ relies on observing

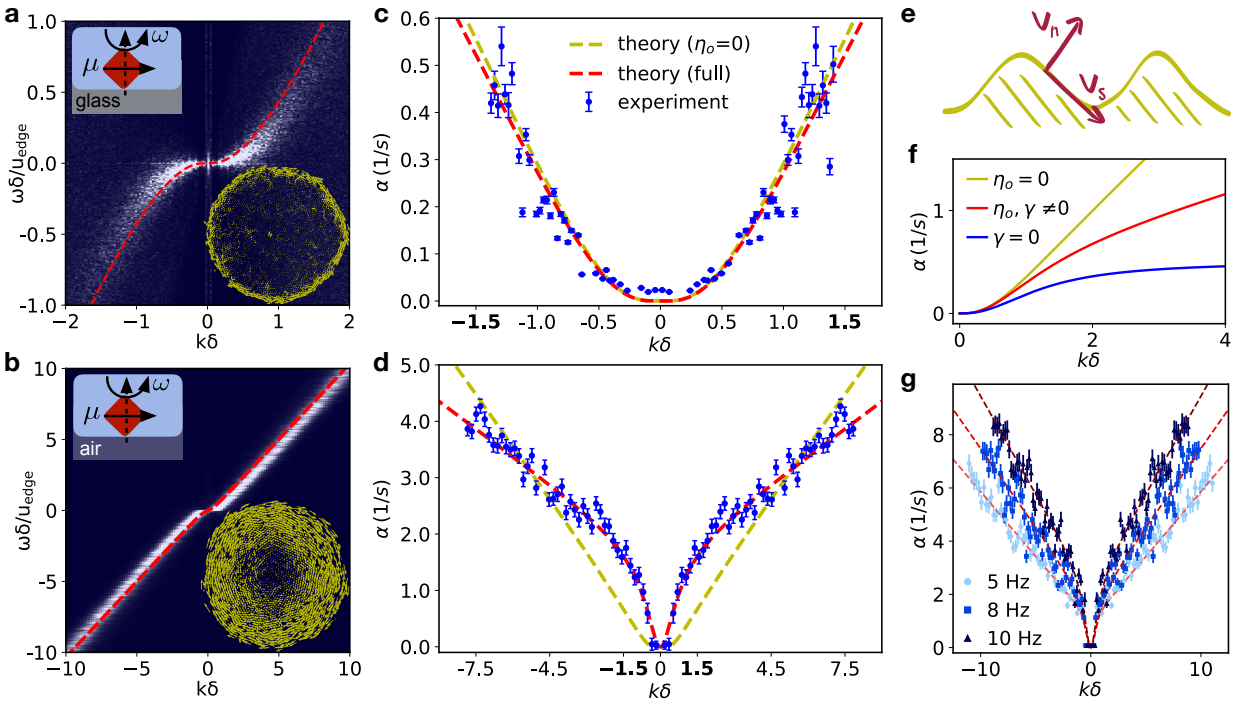

Figure 4.14: **Wave dissipation and measurement of Hall viscosity.** (a) In the circular geometry, surface waves yield power spectra $\langle|R(k,\omega)|\rangle$, plotted here versus the normalized wave vector $k\delta$ and frequency $\omega\delta/u_{\text{edge}}$ (c.f. Fig. 4.5c for a collection of spectra). (b) Power spectrum at a low friction air-water interface, for which the edge current is delocalized into the bulk when compared to a high friction interface as in **a** (see insets). (c) The dissipation rate of waves on the surface of a circular droplet can be used to extract the surface tension, and the shape of $\alpha(k)$ can be captured by a theory with no odd viscosity ($\eta_o = 0$). (d) Lowering substrate friction causes the dissipation to level-off for large $k\delta$, which can only be captured by a theory including η_o. (e) The tangential and normal components of velocity at the boundary give rise to a normal Hall stress. **f,** The dissipation for a chiral fluid with η_o in the absence of surface tension, γ, vs. the same for a fluid with γ in the absence of η_o. For small $k\delta$, the two curves are indistinguishable. For large $k\delta$, the η_o-dissipated fluid shows no k-dependence, while the γ-dissipated fluid shows linear k-dependence. Shown also for reference is the attenuation for a fluid with finite values of both γ and η_o (g) With η_o-induced attenuation, $\alpha(k)$ varies with frequency with all other parameters held constant, a trend that is not observed for γ-dissipated fluids.

wave dissipation $\alpha(k)$ over a large range of rescaled wavelengths $k\delta$. On a glass substrate, the typical range of $k\delta$ is too small to observe these features. The dispersion $\omega(k)$ is not useful in lifting this ambiguity, because it is unchanged by the inclusion of non-zero η_o, as shown in Figure 4.15a. Moreover, the dissipation can be modeled by the hydrodynamic theory incorporating non-zero η_o by compensating with γ, as can be seen from the asymptotic form of $\alpha(k)$ at small $k\delta$, $\alpha \sim k^3(\gamma + \eta_o)$ (see Section 4.4.1) and shown in Figure 4.15a.

However, we obtain a clear signature of Hall viscosity in the dissipation when we decrease the substrate friction Γ_u, by replacing the glass substrate with an oil or air interface. By changing the oil viscosity we can tune Γ_u between these two regimes and explore the emergence of this qualitative signature of Hall viscosity. This procedure regulates δ, thus controlling the range of $k\delta$ over which surface waves are observed. We plot the wave dissipation $\alpha(k)$ for representative values of oil viscosity in Figure 4.16. As the viscosity is decreased (and hence also the substrate friction), the presence of η_o is more discernible through leveling-off at large $k\delta$, and the quality of fits with $\eta_o = 0$ becomes increasingly poor. By contrast, the dissipation on a high viscosity interface can be captured using both a non-zero or zero value of η_o, just as observed for the glass substrate experiments (c.f. Figure 4c).

We note that there is also an ambiguity in distinguishing the effects of Hall viscosity and surface tension for data containing wave dissipation at $k\delta \gg 1$. To see this, we fit $\alpha(k)$ for waves measured at an air interface to the full hydrodynamic theory for γ, by imposing values of η_o $\pm 50\%$ of $\eta_{o,\mathrm{air}}$. We find that the data is fit well for a wide range of values of η_o by tuning γ to compensate, as in Figure 4.15c. To explain the correlation of η_o and γ in this regime, as presented in the right panel, we consider the large $k\delta$ asymptotic $\alpha \sim k\gamma/(1+\eta_o^2)$. The dispersion does not resolve this correlation, as $\omega(k)$ is not strongly-dependent on η_o.

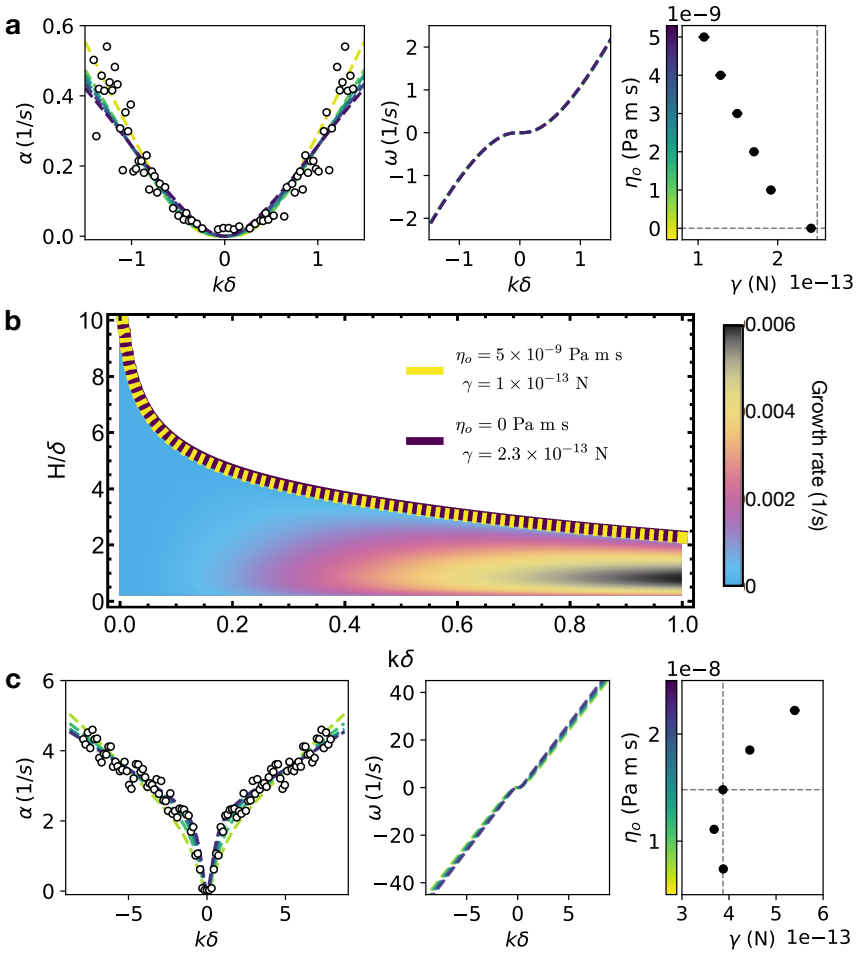

Figure 4.15: **Disambiguating Hall viscosity and surface tension.** (a) For high-friction experiments, the acquired wave dissipation data are limited to $k\delta \sim 1$, and can be fit to both zero and non-zero Hall viscosity (left), yielding no discrepancy in the dispersion (middle), by altering the apparent surface tension (right). (b) The boundary between stable and unstable modes constructed using a non-zero value of Hall viscosity is indistinguishable from the boundary for $\eta_o = 0$. Here, each boundary curve is shown over the calculated diagram for $\eta_o = 0$. (c) In the large $k\delta$ regime, similarly to **a**, we can fit the low-friction experimental data to a wide range of Hall viscosity values (left-middle), in this case finding an opposite correlation to **a** (right).

4.4.3 Physical interpretation of dynamics

We examine the roles of surface tension, shear viscosity, Hall viscosity and rotational viscosity in determining the surface dynamics of the chiral fluid.

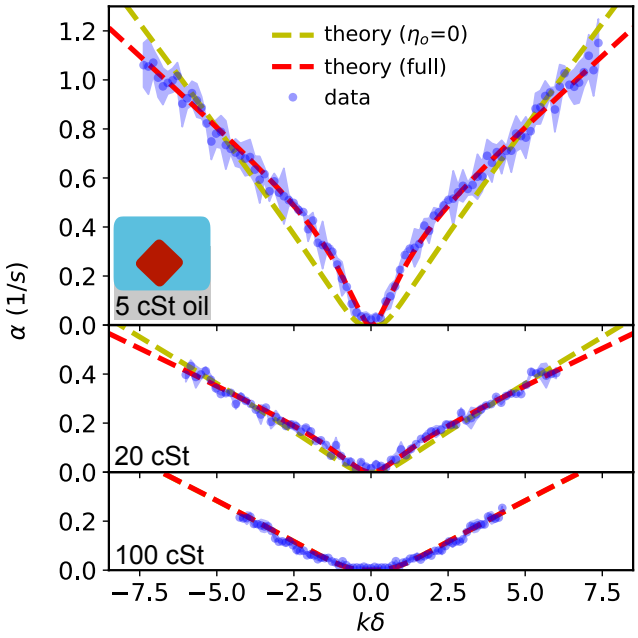

Figure 4.16: **Hall viscosity emerges for low substrate friction.** When the spinner fluid is over a water-oil interface, the wave dissipation can be measured at larger $k\delta$ for lower viscosities of oil, which lead to lower substrate friction and thus larger penetration depth δ. With this extended scope, we are better able to distinguish the effects of surface tension γ and Hall viscosity η_o, by fitting to the theory with and without η_o.

Surface waves driven by "edge-pumping"

We begin by considering the propagation of waves in the limit $\eta_o = \gamma = 0,\ \eta_R \neq 0,\ \eta \to 0$. In this limit, the surface waves are undamped ($\alpha(k) = 0$). The asymptotic dispersion relation computed in Section 4.4.1 for a semi-infinite slab:

$$\omega(k) = \begin{cases} 2u_{\text{edge}}\dfrac{\eta}{\Gamma_u}k^3 & |k\delta| \ll 1 \\ -\dfrac{2\eta_R\Omega}{\eta + 2\eta_R} + u_{\text{edge}}k & |k\delta| \gg 1 \end{cases}$$

provides a basis for discussion. The dispersion relation suggests that in the limit $\eta \to 0$, surface dynamics might be suppressed. This is indeed the case!

Consider the limit $\eta = \eta_o = 0$. The stress boundary condition, Eq. (4.7), reduces simply to $p|_{\partial D} = 0$ and $\omega|_{\partial D} = 2\Omega$. Since $\nabla^2 p = 0$ we have $p \equiv 0$ and, hence, $\nabla p \equiv 0$. This

reduces the bulk flow equations to

$$\mathbf{u} = \frac{\eta_R}{\Gamma_u}\left(-\partial_y\omega, \partial_x\omega\right). \tag{4.19}$$

Evaluating this expression on the boundary ∂D, contracting it against the normal, and applying the kinematic boundary condition yields

$$\mathbf{v}\cdot\mathbf{n} = \frac{v_s}{\Gamma_u}\frac{\partial}{\partial s}\omega|_{\partial D} \equiv 0$$

where the last equality uses that ω is constant on the boundary. Hence, the normal velocity of the boundary is zero, and ∂D is static.

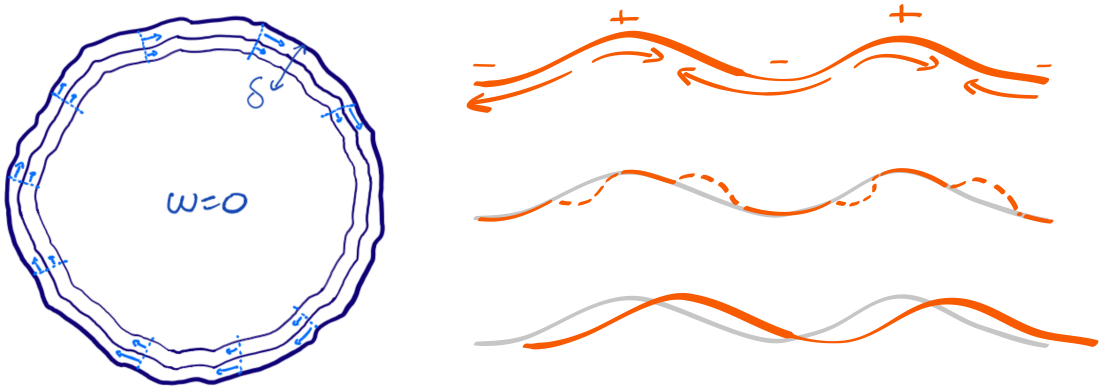

Figure 4.17: **The edge-pumping effect**. (Left:) in the absence of viscosity and surface tension, the boundaries of our chiral fluid droplets do not move; they simply have an exponentially screened edge current glued to them. (Right:) In the presence of viscosity, differential mass flux in the edge current pumps fluid from one region to another, which in the case of a sinusoidal perturbation results in wave propagation.

Lack of surface dynamics does not imply a lack of edge flow; Indeed, Eq. (4.19) establishes a direct connection between a gradient in vorticity and transverse flow. As already noted, the vorticity satisfies the screened Laplace equation:

$$\left(\nabla^2 - \frac{1}{\delta^2}\right)\omega = 0$$

with the boundary condition $\omega = 2\Omega_0$ (for $\eta = \eta_o = 0$). Vorticity at the surface is thus screened on the interior, with the value dropping to zero at distances of a few δ from the boundary. Eq. (4.19) implies that a gradient of vorticity corresponds to flow perpendicular to the gradient, thus the fluid flows along the equi-vorticity lines. Since the vorticity deep in the fluid is zero, the total mass flux of the edge current – obtained by integrating the gradient of the vorticity along a line from the interior of the chiral fluid to its surface – is proportional to the value of the vorticity at the surface. In the absence of viscosity η and Hall viscosity η_o, the latter is constant and the mass flux is constant at all points along the surface. *Thus in the absence of viscosity (and surface tension), the boundary of our chiral fluid droplets does not move, and simply has an exponentially screened edge current glued to it.*

In the presence of viscosity η, however, the value of vorticity at the surface will be increased (decreased) in positively (negatively) curved regions of the boundary, giving rise to enhanced (reduced) mass flux in response to reduced (increased) viscous drag. The differential mass flux then effectively pumps fluid from one region of the surface to another, giving rise to dynamics. A sketch of the resulting flow in the case of a sinusoidal perturbation is shown in Figure 4.17. In this case the result is wave propagation. *This "edge pumping" effect is the fundamental mechanism that gives rise to free surface dynamics of our chiral fluids.*

Sidenote 1: We note that an analogy can be made between vorticity in our system and the electric potential inside a conducting medium, with penetration depth δ. The velocity at the edge depends on the curvature of the surface, roughly as $|\mathbf{u}| = (1 + C\kappa)2\Omega\delta$ for small curvature κ; in the electrostatic analogy, the latter is proportional in magnitude to the surface charge on the conductor which in turn depends on the curvature of the surface. Crucially then, the mass flux in this tangential surface flow is determined by the vorticity ω on the surface: integrating $\frac{\eta_R}{\Gamma_u}\nabla\omega$ from the center (where $\omega = 0$) to the edge is at once equal to $(\eta_R/\Gamma_u)2\Omega$, and hence proportional to the value of the vorticity at the boundary,

and equal to the total mass flux.

Sidenote 2: For nonzero surface tension (and zero Hall viscosity), it is straightforward to show that the surface dynamics when $\eta = 0$ is curve-shortening. Consider a droplet of chiral fluid whose boundary length is $L(t)$. A standard equality is then $\dot{L} = \int_{\partial D} ds\kappa\ \mathbf{v}\cdot\mathbf{n}$. Using the bulk flow equation and that $\omega_s = 0$ on the boundary yields

$$\dot{L} = -\frac{1}{\gamma\Gamma_u}\int_{\partial D} ds\ p\ \frac{\partial p}{\partial \mathbf{n}} = -\frac{1}{\gamma\Gamma_u}\int_D dA\ |\nabla p|^2 < 0 \tag{4.20}$$

where in the last identity we used the divergence theorem and that p is harmonic. Hence, the long-time behavior is simply relaxation to a circular drop.

Effects of Hall stress

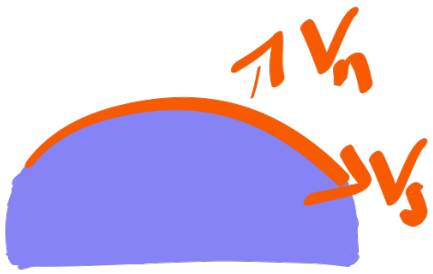

Figure 4.18: **The tangential and normal components of velocity at the boundary** give rise to a normal Hall stress $\eta_o\left(\partial_s v_n + \frac{v_s}{R}\right)$

For an incompressible fluid, the Hall viscosity has no effect on bulk flows. Its influence is instead felt on the boundary where it exerts a stress whose normal component is

$$\sigma_n^o n = \eta_o\left(\partial_s v_n + \frac{v_s}{R}\right)$$

Here, v_s and v_n are the tangential and normal components of velocity, as shown Figure 4.18. Note that in the absence of odd stress η_R and drive, or surface tension γ, there is no flow at

the surface and Hall viscosity has no effect.

Hall damping

The presence of Hall viscosity does not affect surface dynamics in the absence of surface tension and odd stress. Thus the effect that Hall viscosity has on both the propagation and damping of waves originates from the combined effect of Hall viscosity and surface tension, or Hall viscosity and the localized edge current glued to the boundary of our fluid.

In the absence of surface tension, but in the presence of odd stress, the damping of surface waves on a semi-infinite slab $\alpha(k)$ is given by:

$$\alpha(k) = \begin{cases} \dfrac{2\eta_o u_{\text{edge}}}{\Gamma_u}|k|^3 & |k\delta| \ll 1 \\ \dfrac{2\eta_o \eta_R \Omega}{(\eta + 2\eta_R)^2 + \eta_o^2} & |k\delta| \gg 1 \end{cases}$$

This damping originates from the normal component to the boundary Hall stress $\frac{\eta_o u_{\text{edge}}}{R}$, where R is the radius of curvature of the surface. This stress has identical form to the stress arising from surface tension and thus acts to reduce the curvature of the interface (see Figure 4.19).

Figure 4.19: **Hall tension.** The edge current induces a Hall stress that acts like surface tension to flatten the interface.

Dimensionally, for long waves (small wavenumbers compared to δ), a competition of Hall

surface stress and substrate friction:

$$\left[\frac{\eta_o u_{\text{edge}}}{\Gamma_u}\right] \sim \frac{L^3}{T}$$

suggests a scaling with k^3 as found by the calculation above. For short waves however (large wavenumber compared to δ), the substrate friction is no longer relevant and the relevant quantities (in the absence of surface tension) are: $\eta_o, \eta_R, \eta, \Gamma, \Omega, k$. These have dimensions:

$$[\eta_o] = [\eta_R] = [\eta] = \frac{M}{T}, \qquad [\Omega] = \frac{1}{T}, \qquad [k] = \frac{1}{L}$$

Since the viscosities η_o, η_R, η must appear as ratios, the only quantity with the required units of T^{-1} is Ω and the wavenumber k drops out of the problem. This is in contrast to the case of surface tension where the units of length associated with the surface tension $[\gamma] = ML/T^2$ give rise to a linear wavenumber dependence.

These surface stresses lead to the exponential decay of surface perturbations. This role of Hall stress in the damping of surface waves may seem unusual as Hall viscosity is a transverse, conservative stress. This arises in our case from the over-damped nature of our dynamics.

4.5 An odd instability

In much of the phenomenology we have discussed, surface dynamics are essentially boundary layer dynamics. Another natural question, then, is what happens when two boundary layers meet? Draining fluid past a curved obstacle brings about the progressive thinning of a curved strip of chiral fluid, as shown in Fig. 4.1g. The flow is smooth until the strip thickness becomes comparable to the penetration depth δ; at that point the flow goes unstable, resulting in the formation of circular droplets. Although visually reminiscent of the Rayleigh-Plateau instability of a thin fluid cylinder jet [141], this instability is fundamentally different. In our two-dimensional system, surface tension is a purely stabilizing force, as seen in the wave

analysis discussed above. Instead, the instability originates from the chiral surface dynamics of our fluid. A visual signature of this origin is the consistent offset in the phase between top and bottom perturbations at the moment the instability occurs in all strips: Fig. 4.20b shows one such example. In the following, we explore the chiral origin.

4.5.1 Experiment

We study this novel pearling mechanism in experiment by creating a sequence of strips of decreasing thickness, as shown in Fig. 4.20a. We prepare strips by accumulating particles against a straight edge, either by rolling all particles to one side (see Figure 4.3), or by tilting the sample. We control the thickness of the strips by changing the concentration of the suspension. To get strips of different thicknesses, like the ones shown in Figure 4.20, we vary the concentration of the original suspension. We characterize the thickness of a strip before it goes unstable (if it does) by measuring the thickness at various points and taking the mean. To measure the wavelength of the instability in unstable strips, we take the fast Fourier transform of the strip's outline, as described in Section 4.4.2, up to the breakup point. The unstable modes appear as fast-growing peaks in this Fourier transform.

In order to to measure the asymmetry in the outline of the breakup points, we collect the outlines at several of these break-up points, rescaling them by the strip thickness at the thinnest point and by the unstable wavelength in each case, and overlaying them, as shown in Figure 4.20. We find that over a period of 10 minutes the strips of chiral fluid are stable for thicknesses above $\sim 32\,\mu$m and unstable below.

4.5.2 Stability analysis of a finite slab

To explore the origins of this instability, we examine the response of a steady-state slab solution to small perturbations away from the bounding surfaces being flat.

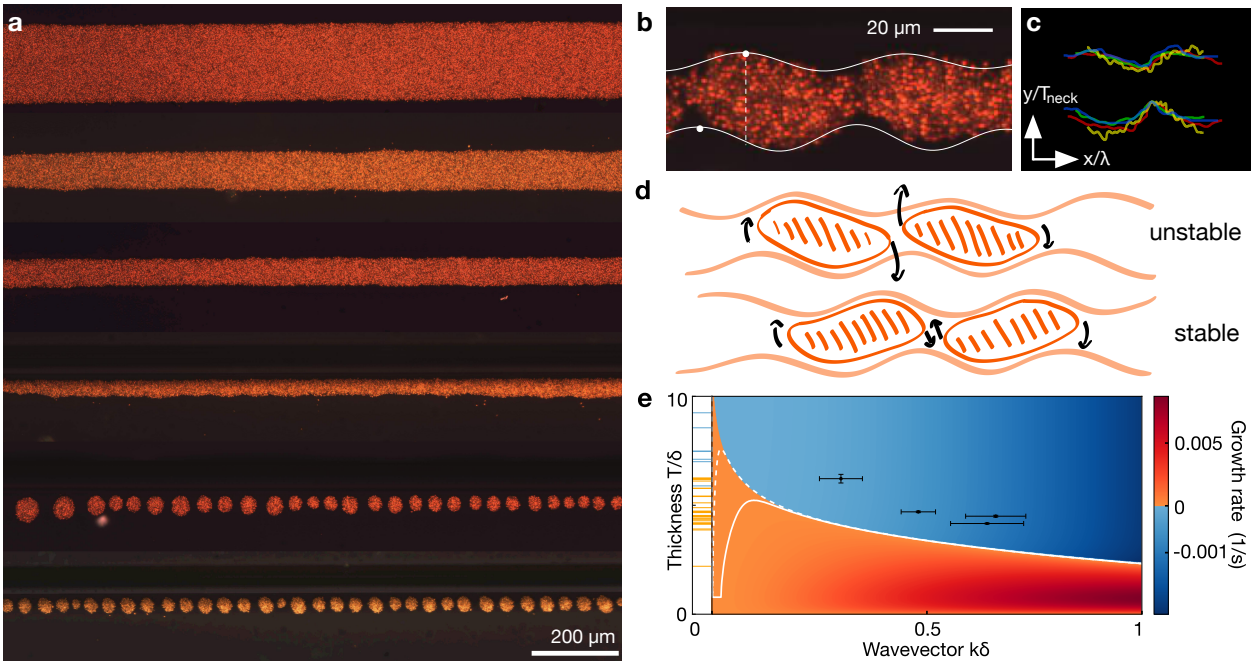

Figure 4.20: **A hydrodynamic instability.** (a) Strips of chiral fluid with different thicknesses. Above 32 μm, the strips are stable, as observed over the course of $\geq$ 10 minutes. Below 32 μm the strips break into droplets within 1 minute. (b) Chiral fluid strip approaching instability. Continuous white lines represent the sum of the most prominent Fourier modes of the strip outline. Relative phase difference between interfaces is emphasized by the two white dots and vertical dashed line. (c) Overlay of strip outlines at four breakup points; each color corresponds to a different instability occurrence. x-axis is rescaled by the most prominent wavelength, λ. y-axis is rescaled by the thickness at the narrowest point, T_{neck}. The relative phase between the top and bottom interface is consistent with theory. (d) Schematic of the instability mechanism. Thin strips of chiral fluids are like a collection of elongated droplets rotating in the direction of the edge current. This leads to the breakup (top) or stabilization (bottom) of the strip. (e) Stability diagram, calculated with linear stability analysis using our experimentally extracted values for the hydrodynamic coefficients, with $\eta_{\mathrm{o}} = 0$. The thinner the strip, the larger the range of unstable wavelengths. A surface fluctuation at an unstable wavelength will grow exponentially: orange denotes a positive growth rate and blue denotes a negative growth rate, namely damping. Contour lines mark growth rates corresponding to 10 minutes (continuous) and 1 day (dashed). Black points represent experimental data from unstable strips; wavelengths were measured by Fourier-transforming the strip outline. Error bars in thickness correspond to the standard deviation in the measurement at various points. Error bars in wavelength correspond to the half-width of the Fourier peaks. Horizontal lines on y-axis mark the recorded strip thicknesses: orange and blue lines correspond to unstable and stable strips, respectively.

Steady state solution

Consider a slab of chiral fluid with thickness H, as depicted in Figure 4.7a. It is easy to verify that the following expression for ω satisfies the bulk equation (Eq. (4.5)):

$$\omega = \frac{\eta_R}{\eta + \eta_R} 2\Omega \frac{\cosh\left(\frac{y}{\delta}\right)}{\cosh\left(\frac{H}{\delta}\right)}. \tag{4.21}$$

for $|y| \leq H$. The corresponding velocity has a non-zero component only in the $\hat{\mathbf{x}}$ direction and can be obtained by direct integration:

$$u_x = -\frac{\eta_R}{\eta + \eta_R} 2\Omega\delta \frac{\sinh\left(\frac{y}{\delta}\right)}{\sinh\left(\frac{H}{\delta}\right)}$$

As in the case of the semi-infinite slab, the kinematic boundary condition is satisfied as there is no vertical component to the velocity. The normal stress boundary condition reduces to $\sigma_{yy} = p = p_0$ where p_0 is the pressure outside the slab which can be set to zero. The tangential stress boundary condition reduces to: $\sigma_{yx} = 2\eta_R\Omega - (\eta + \eta_R)\omega|_{y=\pm H} = 0$, which is satisfied by Eq. (4.21).

Figure 4.7b depicts the flow field which consists of a left-moving, exponentially decaying current on the top surface and a right-moving, exponentially decaying current on the bottom surface.

Linearization scheme

Consider a flat interface at $y = 0$ which we perturb with a zero-mean perturbation $y = h(x,t) = \varepsilon g(x,t)$ with $\varepsilon << 1$. We will shift this result to the upper and lower surfaces when needed. We represent the steady-state velocity, vorticity, and stress fields as $\bar{\mathbf{u}} = (\bar{u}, \bar{v})$,

$\bar{\omega}$, and $\bar{\sigma}$, respectively, and introduce perturbations as

$$\begin{aligned} u(x,y) &= \bar{u}(y) + \varepsilon\tilde{u}(x,y) \\ v(x,y) &= \varepsilon\tilde{v}(x,y) \\ \omega &= \bar{\omega}(y) + \varepsilon\tilde{\omega}(x,y) \\ \boldsymbol{\sigma} &= \bar{\boldsymbol{\sigma}}(y) + \varepsilon\tilde{\boldsymbol{\sigma}}(x,y) \\ p &= \varepsilon q(x,y) \end{aligned}$$

Linear theory

In this section we derive the linearized equations for the perturbed slab.

Linearized bulk equations The linearized bulk equations are given by:

$$\left(\bar{\eta}\nabla^2 - \Gamma_u\right)\tilde{u}_i = \partial_i q \quad \text{and} \quad \nabla\cdot\tilde{\mathbf{u}} = 0 \tag{4.22}$$

where $\bar{\eta} = \eta + \eta_R$.

Linearized stress boundary conditions The stress boundary conditions relate the bulk fields to interfacial data. We take an upward normal $\hat{\mathbf{n}} \approx \hat{\mathbf{y}} - \varepsilon g_x\hat{\mathbf{x}}$ and the RHS of Eq. (4.7) is to linear order $\gamma\kappa\hat{\mathbf{n}} \approx \varepsilon\gamma g_{xx}\hat{\mathbf{y}}$. Expanding Eq. (4.7) to linear order, and using that $\bar{\sigma}(0)\hat{\mathbf{y}} = \mathbf{0}$ yields

$$\tilde{\boldsymbol{\sigma}}(x,0)\hat{\mathbf{y}} = \gamma g_{xx}(x)\hat{\mathbf{y}} + g_x(x)\bar{\boldsymbol{\sigma}}(0)\hat{\mathbf{x}} - g(x)\bar{\boldsymbol{\sigma}}_y(0)\hat{\mathbf{y}}$$

After some simplification we obtain:

$$\begin{aligned} &\bar{\eta}\tilde{u}_y(x,0) + (\eta - \eta_R)\tilde{v}_x(x,0) + 2\eta_o\tilde{u}_x(x,0) = \bar{\eta}\bar{\omega}_y(0)\,g(x) + 2\eta_o\bar{\omega}(0)g_x(x) \\ &2\eta\tilde{v}_y(x,0) - q(x,0) + 2\eta_o\tilde{v}_x(x,0) = \gamma g_{xx}(x) - \left[(\eta - \eta_R)\,\bar{\omega}(0) + 2\eta_R\Omega\right]g_x(x) \end{aligned} \tag{4.23}$$

Note: for the lower surface, where the normal points downwards, the sign of the surface tension term is reversed to maintain the right relation of curvature to normal direction.

Linearized kinematic boundary condition The linearized kinematic boundary condition is given by:

$$g_t + \bar{u}\,(0)\, g_x = \tilde{v}\,(x, 0) \tag{4.24}$$

Solution

To solve Eqs. (4.23, 4.24, 4.25) we make use of Fourier transforms in the x direction to take advantage of translational invariance.

Solution of the linearized bulk equations Taking the Fourier transform in x:

$$\bar{\eta}\left(\partial_{yy} - k^2\right)\tilde{\mathbf{u}} - \Gamma_u\tilde{\mathbf{u}} - \left(ik, \partial_y\right) q = \mathbf{0} \;\text{ and }\; \left(ik, \partial_y\right)\cdot\tilde{\mathbf{u}} = 0$$

Using that $\left(\partial_{yy} - k^2\right) q = 0$ we obtain:

$$\begin{aligned}
q &= A^+ e^{|k|y} + A^- e^{-|k|y} \\
\tilde{u} &= -\frac{ik}{\bar{\eta}}\delta^2\left(\mu_k^\pm A\right) + \left(\mu_\star^\pm B\right) \\
\tilde{v} &= -\frac{|k|}{\bar{\eta}}\delta^2\left(\Delta_k^\pm A\right) - \frac{ik}{|\star|}\left(\Delta_\star^\pm B\right) \\
\tilde{u}_y &= -\frac{ik\,|k|}{\bar{\eta}}\delta^2\left(\Delta_k^\pm A\right) + |\star|\left(\Delta_\star^\pm B\right) \\
\tilde{v}_y &= -\frac{|k|^2}{\bar{\eta}}\delta^2\left(\mu_k^\pm A\right) - ik\left(\mu_\star^\pm B\right)
\end{aligned} \tag{4.25}$$

Where $\star^2 = k^2 + \delta^{-2}$ and $\mu_k^\pm f = e^{\pm|k|H} f^+ + e^{\mp|k|H} f^-$ and $\Delta_k^\pm f = e^{\pm|k|H} f^+ - e^{\mp|k|H} f^-$. The coefficients $A^\pm$ and $B^\pm$ are to be determined from the boundary conditions.

Application of the stress boundary conditions Inserting Eq. (4.25) into the linearized stress boundary conditions Eq. (4.23) yields:

$$-2ik\left|k\right|\delta^2\frac{\eta}{\bar{\eta}}\left(\Delta^{\pm}A\right)+\frac{1}{|\star|}\left[2\eta k^2+\bar{\eta}\delta^{-2}\right]\left(\Delta_{\star}^{\pm}B\right)+2\frac{\eta_o}{\bar{\eta}}k^2\delta^2\left(\mu^{\pm}A\right)+2ik\eta_o\left(\mu_{\star}^{\pm}B\right)$$
$$=\left[\pm\eta_R\frac{2\Omega}{\delta}\tanh\left(\frac{H}{\delta}\right)+i2k\eta_o\frac{\eta_R}{\bar{\eta}}\Omega\right]g^{\pm}$$

and

$$\left[1+2\frac{\eta}{\bar{\eta}}\left|k\right|^2\delta^2\right]\left(\mu^{\pm}A\right)+2ik\eta\left(\mu_{\star}^{\pm}B\right)-2i\frac{\eta_o}{\bar{\eta}}k|k|\delta^2\left(\Delta^{\pm}A\right)+2\eta_o\frac{k^2}{|\star|}\eta\left(\Delta_{\star}^{\pm}B\right)$$
$$=\left(\pm\gamma k^2+i2k\frac{\eta\eta_R}{\bar{\eta}}2\Omega\right)g^{\pm}$$

which is a set of four linear equations for the four unknowns $A^{\pm}, B^{\pm}$ in terms of the top and bottom surface perturbations $g^{\pm}$. A very tedious calculation which we suppress here to maintain excitement yields an inversion of these relations.

Application of the kinematic boundary condition Combining this with the kinematic boundary condition:

$$g_t^{\pm}+ik\bar{u}^{\pm}g^{\pm}=\tilde{v}^{\pm}$$

and substituting $\tilde{v}^{\pm}$ we have:

$$g_t^{+}-ikUg^{+}=-\frac{|k|}{\bar{\eta}}\delta^2\Delta_k^{+}A-\frac{ik|}{|\star|}\Delta_{\star}^{+}B$$
$$g_t^{-}+ikUg^{-}=-\frac{|k|}{\bar{\eta}}\delta^2\Delta_k^{-}A-\frac{ik|}{|\star|}\Delta_{\star}^{-}B$$

These equations can be solved to yield the evolution of the surface of a perturbed slab of finite width. Explicit analytical computation of these modes becomes tedious at this point.

Visualization and asymptotics

The evolution of the surface corresponding to a sinusoidal perturbation of the height $g \sim \mathrm{Re}\left[e^{ikx}\right]$ is given by $g \sim \mathrm{Re}\left[e^{i(kx+\omega t)}e^{-\alpha t}\right]$ where $i\omega - \alpha = \sigma$, the eigenvalue of the linearized coupled evolution equations. There are, generally, two eigenvalues and associated eigenvectors. The real part of the eigenvalues $\alpha(k)$ indicates whether the wave amplitude decreases, remains the same, or grows exponentially in time.

In general, we find that for thick slabs ($|kH| \gg 1$, $H \gg \delta$), the eigenvalues and eigenvectors correspond to two copies of the semi-infinite slab problem, with damped surface waves on the bottom surface propagating in a direction opposite to those on the top surface. For thin slabs ($H \leq \delta$) we find unstable modes, whose growth rate is reduced by both surface tension and Hall viscosity.

Since the algebra can get quite tedious, we present our results by first considering the problem in the absence of Hall viscosity and subsequently considering the changes brought about by the presence of Hall viscosity. In the absence of Hall viscosity, substituting the solutions for $A^{\pm}, B^{\pm}$ in terms of Δg and μg give evolution equations of the form:

$$\begin{bmatrix} \Delta g_t \\ \mu g_t \end{bmatrix} = \mathbf{M}_k \begin{bmatrix} \Delta g \\ \mu g \end{bmatrix} = \begin{bmatrix} \gamma a_\Delta & i2\Omega b_\mu \\ i2\Omega b_\Delta & \gamma a_\mu \end{bmatrix} \begin{bmatrix} \Delta g \\ \mu g \end{bmatrix} \tag{4.26}$$

The dispersion relation and stability diagrams follow from the eigenvalues of $\mathbf{M}_k$. The coefficients $a_{\Delta,\mu}$ and $b_{\Delta,\mu}$ are complicated, but real, functions of the system parameters and wavenumber k, except for the surface tension γ and the (forcing) spinning frequency 2Ω which appears only multiplicatively in $\mathbf{M}_k$ as shown. Hence, in the absence of surface tension the eigenvalues of $\mathbf{M}_k$ are either a purely imaginary, complex conjugate pair, or a real-valued positive/negative pair.

Regions of stability and instability are depicted in Figure 4.21c in the limit of vanishing surface tension and in Figure 4.22c for finite surface tension.

Intermediate surface waves For finite wavenumber $k\delta$, above a certain thickness $2H$, the eigenvalues correspond to propagating waves that are damped in the presence of surface tension. A representative dispersion $\omega(k)$ relation and damping rate α for the waves are depicted in Figures 4.21b and 4.22b. The corresponding flow fields are depicted in Figures 4.21a and 4.22a. The two eigenvalues correspond in this case to surface waves that propagate to the left in on the top surface and to the right on the bottom surface.

Taking the limit of large thickness $|kH| \gg 1$, and long wavelength $|k\delta| \ll 1$, and restricting our attention to the upper surface, we find the following asymptotic expression:

$$i\omega + \alpha = 2iu_{\text{edge}}\frac{\eta}{\Gamma_u}k^3 + \frac{\gamma}{\Gamma_u}|k|^3$$

which corresponds to waves moving in the same direction as u_{edge}, damped by surface tension.

This reflects the intuitive expectation that for $H \gg \delta$ the problem should reduce to two copies of the semi-infinite slab problem. Adding Hall viscosity, computing the finite slab spectrum numerically and comparing it to the semi-infinite slab problem with Hall viscosity further confirms this intuition.

Short waves For finite thickness, and sufficiently large wavenumber $k\delta \gg 1$, $kH \gg 1$, Eq. (4.26) simplify to

$$\begin{bmatrix} \Delta g_t \\ \mu g_t \end{bmatrix} = \begin{bmatrix} -\tilde{\gamma}|k| & i2\frac{\eta_R}{\bar{\eta}}\delta\Omega\tanh\left(\frac{\bar{h}}{\delta}\right)|k| \\ i2\frac{\eta_R}{\bar{\eta}}\delta\Omega\tanh\left(\frac{\bar{h}}{\delta}\right)|k| & -\tilde{\gamma}|k| \end{bmatrix} \begin{bmatrix} \Delta g \\ \mu g \end{bmatrix} \tag{4.27}$$

with $\tilde{\gamma} = \frac{\gamma}{2\eta_R\left(2-\frac{\eta}{\bar{\eta}}\right)} > 0$. Seeking exponential solutions $(\Delta g, \mu g) = e^{\sigma t}(\Delta g_0, \mu g_0)$ yields

$$\sigma = -\tilde{\gamma}|k| \pm i\frac{\eta_R}{\bar{\eta}}\delta 2\Omega\tanh\left(\frac{\bar{h}}{\delta}\right)|k|$$

Hence, small length-scales are stabilized by surface tension in a manner consistent with classical results for the two-dimensional Stokes equations [142] while the gyroscopic drive produces waves.

Unstable long-wavelength modes For finite thickness slabs, $\eta_o = 0$, and long waves, $|k|H << 1$, one of the eigenvalues is always unstable, as can be seen in Figures 4.21c and 4.22c. Representative dependences on wavenumber of the growth/decay rates of the eigenvalues in this regime are shown in Figures 4.21d and 4.22d, together with the corresponding flow fields (Figures 4.21e and 4.22e). In this limit, Eq. (4.26) simplify to

$$\begin{bmatrix} \Delta g_t \\ \mu g_t \end{bmatrix} = \begin{bmatrix} -\gamma\beta_1 k^4 & i2\Omega\alpha_1 k^3 \\ -i2\Omega\alpha_2 k & -\gamma\beta_2 k^2 \end{bmatrix} \begin{bmatrix} \Delta g \\ \mu g \end{bmatrix}$$

where $\beta_1 = H\delta^2/\bar{\eta}$, $\beta_2 = \delta^2/\bar{\eta}H$, $\alpha_1 = 2\delta^3\left(\eta\eta_R/\bar{\eta}^2\right)\tanh\left(\frac{H}{\delta}\right)$, and, finally, $\alpha_2 = \left(2\delta^2/H\right)\left(\eta\eta_R/\bar{\eta}^2\right)\mathrm{sech}^2\left(\frac{\mathrm{H}}{\delta}\right)$ are all positive constants. Seeking exponential solutions $(\Delta g, \mu g) = e^{\sigma t}(\Delta g_0, \mu g_0)$ yields

$$\sigma = \frac{1}{2}\left[-\gamma\beta_2 \pm \left((\gamma\beta_2)^2 + 2\Omega^2\alpha_1\alpha_2\right)^{1/2}\right]k^2 \tag{4.28}$$

Hence, at long wavelengths, there is always both a stable and an unstable mode. In each case, both surface tension and driving scale quadratically in k in the eigenvalue, and surface tension damps both stable and unstable modes generated by activity (i.e. $2\Omega^2 > 0$).

Performing the same calculation numerically in the presence of Hall viscosity presents a similar picture. Hall viscosity, like surface tension, generally acts as a stabilizing stress, albeit with a different wavenumber dependence, as illustrated in Figure 4.23.

Fig. 4.20e shows the predicted stability diagram together with our experimental observations.

4.5.3 Intuitive picture

Here we give a simple geometric model that explains the nature of the stable and unstable modes of the slab, the latter of which leads to the formation of droplets in experiment. Consider the coupled surface modes for the slab computed above (see Eqs. (4.26, 4.28)). These consist of sinusoidal perturbations on the top and bottom surfaces, respectively, that have relative phases of either $\pi/2$ or $-\pi/2$, with their respective flow fields plotted in Figures 4.21e and 4.22e. In the unstable case the upper surface is shifted leftwards relative to the lower, and oppositely for the stable case. As depicted in Figure 4.20 the geometry of such a perturbed slab can be approximated by a collection of elongated droplets of chiral fluid, all canted in the same direction. In isolation, droplets of this kind would rotate clockwise. Because of their canted angle, the configuration shown in Figure 4.20**e** (top) would evolve into separate droplets, whereas that shown in Figure 4.20**e** (bottom) would evolve towards a flat slab-like configuration (stable). The former case is consistent with the reconstructed, unstable slab boundaries shown in Fig. 4.20**b** and **c**.

4.5.4 Conclusion

We have broken parity symmetry at the microscopic level in a colloidal chiral fluid, resulting in the emergence of an odd stress that in turn generates lively surface flows. Likewise, we have broken time reversal symmetry, giving rise to Hall viscosity, a dissipationless transport property which has thus far remained experimentally elusive. The combination of these features drives rich interfacial dynamics with no analogues in conventional fluids. These dynamics include the uni-directional propagation and anomalous attenuation of surface waves and an asymmetric pearling instability. In principle, these chiral phenomena can be tuned, for instance by altering the colloidal particles' shape and their effective interactions. Beyond enabling the study of universal aspects of a new class of hydrodynamics, colloidal chiral fluids provide a platform for engineering active materials with so far untapped, 'odd' behaviors [134, 113, 110].

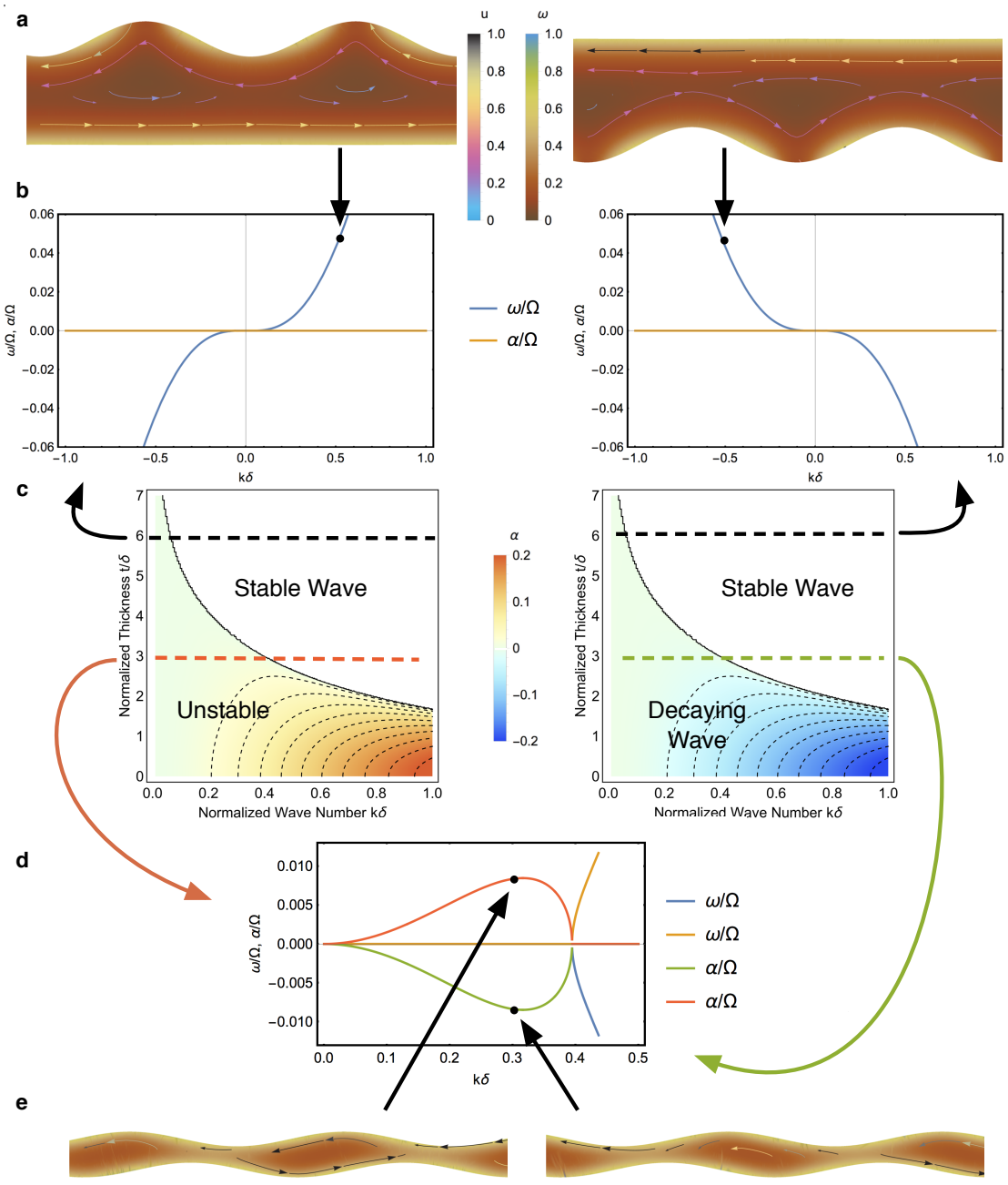

Figure 4.21: **The nature of solutions to the linearized slab dynamics, in the absence of surface tension and Hall viscosity.** (a) Flow fields for the two branches of dispersive surface waves on a large thickness slab. (b) The dispersion relation (blue) and growth/decay rate for these surface waves. While difficult to discern due to its small magnitude, the latter is nonzero (positive at left, negative at right) near $k = 0$. (c) Stability diagram, showing the growth (red) or decay (blue) rates, as a function of normalized wavenumber and slab thickness. Stable waves are purely dispersive, having zero linear growth rate. Contours are levels of constant growth/decay rate. (d) The growth (red) and decay (green) rates, as a function of normalized wavenumber, for the unstable/stable modes on a slab. (e) The associated flow fields, and surface deformations, for the unstable (left) and stable (right) modes.

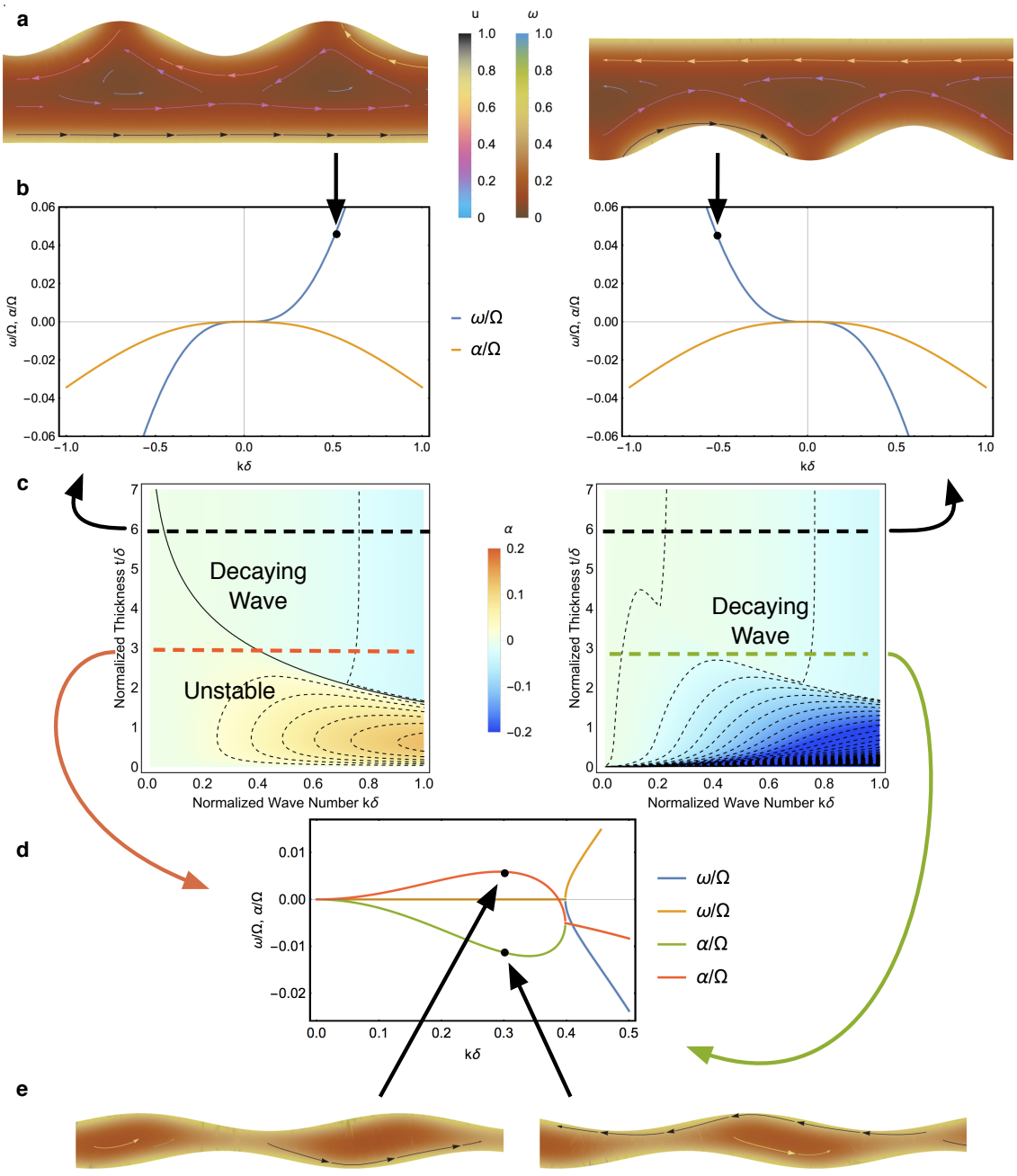

Figure 4.22: **The nature of solutions to the linearized slab dynamics, in the presence of surface tension (in the absence of Hall viscosity).** (a) Flow fields for the two branches of damped, dispersive surface waves on a large thickness slab. (b) The dispersion relation (blue) and decay rates (red) for such surface waves. (c) Stability diagram, showing the growth (shades of red) or decay (shades of blue) rates, as a function of normalized wavenumber and slab thickness. Contours are levels of constant growth/decay rate. (d) The growth (red) and decay (green) rates, as a function of normalized wavenumber, for the unstable/stable modes on an unstable slab. (e) The associated flow fields, and surface deformations, for the unstable (left) and stable (right) modes.

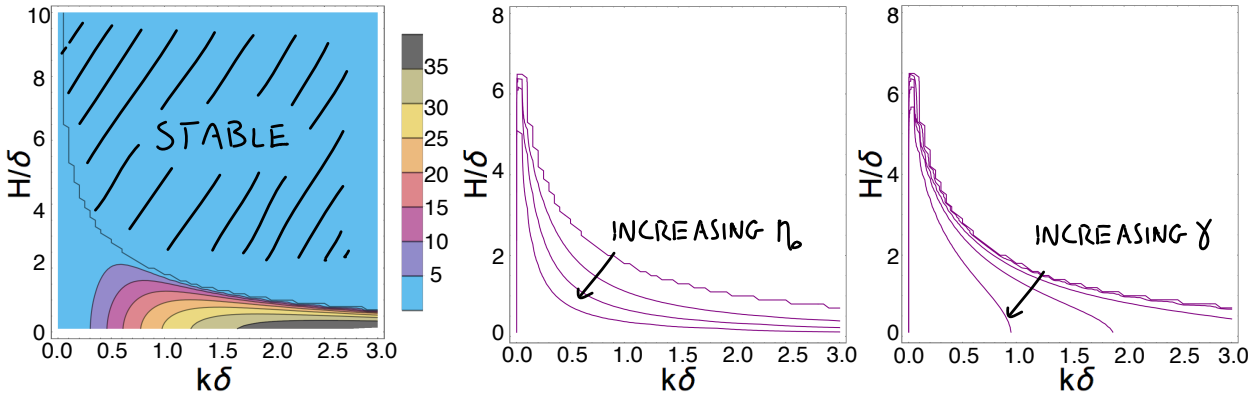

Figure 4.23: **Effect of surface tension and Hall viscosity on the stability of finite thickness slabs.** (a) The stability diagram in the absence of surface tension and Hall viscosity (c.f. Figure 4.21). (b) Increasing the Hall viscosity, η_o, moves the line separating stable from unstable modes as depicted. (c) Increasing the surface tension, γ, moves the line separating stable from unstable modes as depicted. In both cases the effect is to stabilize the interface by increasing the extent of the stable region. The large wavenumber dependence of the damping effects of surface tension and Hall viscosity accounts for the different effects they have on the stability diagram.

APPENDIX A

SURFACE RECONSTRUCTION

We can write the metric associated with the conformal transformation as $ds^2 = \Lambda^2(r)(dr^2 + d\theta^2)$. Interpreting this expression as the metric of a surface written in conformal (isothermal) coordinates, we can write the Gaussian curvature as $K(r) = \frac{1}{\Lambda^2(r)}\Delta \ln(\frac{1}{\Lambda(r)})$.

Consider a nonuniform crystal with rotationally symmetric lattice spacing $a(r)$. In order to make such a crystal uniformly spaced, the local lattice spacing must be scaled by $\Lambda(r) = a_0/a(r)$, where a_0 is an arbitrary constant. The resulting metric thus has the form $ds^2 = \frac{a_0^2}{a^2(r)}(dr^2 + r^2 d\theta^2)$. We can make a coordinate transformation by defining

$$\rho(r) = \frac{a_0 r}{a(r)}$$

and

$$dR = \frac{a_0}{a(r)}dr,$$

so that $R = \int_0^r \frac{a_0}{a(r')}dr'$. We thus have $ds^2 = dR^2 + \rho^2(R)d\theta^2$. In this coordinate system, we can parametrize the surface as

$$x = \rho(R)cos\theta$$

$$y = \rho(R)sin\theta$$

and

$$z = \int_0^R \sqrt{1 - \left(\frac{d\rho(r')}{dr'}\right)^2}\, dr'$$

Similarly, for translationally symmetric structures, we can write the transformed metric as $ds^2 = \frac{a_0^2}{a^2(r)}(dx^2 + dz^2)$. We can then make a coordinate transformation by setting

$$\frac{\theta}{2\pi} = \frac{x}{\Delta x},$$

where Δx is the width in the x direction. Thus $dx = \frac{\Delta x}{2\pi} d\theta$ and $ds^2 = \left(\frac{a_0}{a(z)} \frac{\Delta x}{2\pi}\right)^2 d\theta^2 + \left(\frac{a_0}{a(z)}\right)^2 dz^2$. We can then again define

$$\rho = \frac{a_0}{a(z)} \frac{\Delta x}{2\pi}$$

and

$$dR = \frac{a_0}{a(z)} dz.$$

Thus, $R = \int \frac{a_0}{a(z)} dz$. Thus we again have $ds^2 = dR^2 + \rho(R)^2 d\theta^2$ and we can parametrize the surface as in the rotationally symmetric case.

Embeddability of the resulting surfaces in $\mathbb{R}^3$ is not automatically guaranteed. In the case of rotationally symmetric surfaces with negative gaussian curvature everywhere, it can be shown that $\left(\frac{d\rho(r')}{dr'}\right)^2 < 1$ everywhere, and thus the z coordinate is complex throughout the structure. In other cases, the resulting surface may only be partially embeddable. However, in these situations, the structure may be embedded by augmenting the procedure by transforming the angular variable $\theta \to \phi$, where $n\theta = \phi, n > 1$. The structure will thus cover the resulting surface n times. Fig.3.5 and 3.6 demonstrate this for the case of Coulomb interacting particles in a translationally symmetric hard-walled potential, in which the resulting surface has a catenoid-like geometry.

REFERENCES

[1] Leonard C Bruno and Lawrence W Baker. *Math and mathematicians: the history of math discoveries around the world*. U X L, Detroit, Mich., 1999. OCLC: 41497065.

[2] Paul M. Chaikin and T. C. Lubensky. *Principles of condensed matter physics*. Cambridge University Press, 1995.

[3] David R. Nelson. *Defects and Geometry in Condensed Matter Physics*. Cambridge University Press, 2002-03-18.

[4] J Kepler. *Strena seu de nive Sexangula, Frankfurt, Jos. Tampach 1611. Translation as: The Six-Cornered Snowflake: A New Years Gift (Colin Hardie, Translator)*. Clarendon Press: Oxford, 1966.

[5] W. L. Bragg. The Structure of Some Crystals as Indicated by Their Diffraction of X-rays. *Proceedings of the Royal Society of London. Series A, Containing Papers of a Mathematical and Physical Character*, 89(610):248–277, 1913.

[6] J. B. Jones. Structure of Opal. *Nature*, 204:990–991, December 1964.

[7] J. D. Bernal and I. Fankuchen. X-RAY AND CRYSTALLOGRAPHIC STUDIES OF PLANT VIRUS PREPARATIONS. *The Journal of General Physiology*, 25(1):111–146, September 1941.

[8] Bragg William Lawrence and Nye J. F. A dynamical model of a crystal structure. *Proceedings of the Royal Society of London. Series A. Mathematical and Physical Sciences*, 190(1023):474–481, September 1947.

[9] Robert Brown. XXVII. A brief account of microscopical observations made in the months of June, July and August 1827, on the particles contained in the pollen of plants; and on the general existence of active molecules in organic and inorganic bodies. *The Philosophical Magazine*, 4(21):161–173, 1828.

[10] A Einstein. INVESTIGATIONS ON THE THEORY OF THE BROWNIAN MOVEMENT. *Ann. der Physik*, 1905.

[11] Akira Kose, Masataka Ozaki, Kaoru Takano, Yoko Kobayashi, and Sei Hachisu. Direct observation of ordered latex suspension by metallurgical microscope. *Journal of Colloid and Interface Science*, 44(2):330–338, August 1973.

[12] David G. Grier and Cherry A. Murray. The microscopic dynamics of freezing in supercooled colloidal fluids. *The Journal of Chemical Physics*, 100(12):9088–9095, June 1994.

[13] Cherry A. Murray and David G. Grier. Colloidal Crystals. *American Scientist*, 83(3):238–245, 1995.

[14] Cherry A. Murray and David G. Grier. Video microscopy of monodisperse colloidal systems. *Annual Review of Physical Chemistry*, 47(1):421–462, October 1996.

[15] Pawel Pieranski. Colloidal crystals. *Contemporary Physics*, 24(1):25–73, January 1983.

[16] Pawel Pieranski. Two-Dimensional Interfacial Colloidal Crystals. *Physical Review Letters*, 45(7):569–572, August 1980.

[17] K. Zahn, R. Lenke, and G. Maret. Two-Stage Melting of Paramagnetic Colloidal Crystals in Two Dimensions. *Physical Review Letters*, 82(13):2721–2724, March 1999.

[18] Karol Miszta. Hierarchical self-assembly of suspended branched colloidal nanocrystals into superlattice structures. *Nature Materials*, 10(11):872–876, 2011-09.

[19] JCP Gabriel and P Davidson. New trends in colloidal liquid crystals based on mineral moieties. *Advanced Materials*, 12(1):9–+, 2000-09.

[20] V. Prasad, D. Semwogerere, and Eric R. Weeks. Confocal microscopy of colloids. *Journal of Physics: Condensed Matter*, 19(11):113102, February 2007.

[21] John C. Crocker and David G. Grier. Methods of Digital Video Microscopy for Colloidal Studies. *Journal of Colloid and Interface Science*, 179(1):298–310, April 1996.

[22] David G. Grier. A revolution in optical manipulation. *Nature*, 424:810–816, August 2003.

[23] ME Leunissen. *Manipulating colloids with charges and electric fields*. PhD Thesis, Utrecht University, 2007.

[24] H. Lwen. Colloidal dispersions in external fields: recent developments. *Journal of Physics: Condensed Matter*, 20(40):404201, September 2008.

[25] Igor S. Aranson. Active colloids. *Physics-Uspekhi*, 56(1):79, 2013.

[26] Alexey Snezhko. Complex collective dynamics of active torque-driven colloids at interfaces. *Current Opinion in Colloid & Interface Science*, 21:65–75, February 2016.

[27] S. J. Ebbens. Active colloids: Progress and challenges towards realising autonomous applications. *Current Opinion in Colloid & Interface Science*, 21:14–23, February 2016.

[28] Andreas Zttl and Holger Stark. Emergent behavior in active colloids. *Journal of Physics: Condensed Matter*, 28(25):253001, May 2016.

[29] Richard Zallen. *The Physics of Amorphous Solids*. John Wiley & Sons, 2008-07-11. Google-Books-ID: fHoJn0P_XwYC.

[30] Salvatore Torquato. *Random Heterogeneous Materials: Microstructure and Macroscopic Properties*. Springer Science & Business Media, 2013-04-17. Google-Books-ID: UTfoBwAAQBAJ.

[31] Robert D Batten, Frank H Stillinger, and Salvatore Torquato. Phase behavior of colloidal superballs: Shape interpolation from spheres to cubes. *Physical Review E*, 81(6):061105, 2010-09.

[32] BS John, A Stroock, and FA Escobedo. Cubatic liquid-crystalline behavior in a system of hard cuboids. *The Journal of Chemical Physics*, 120(19):9383–9389, 2004.

[33] Bettina S John, Carol Juhlin, and Fernando A Escobedo. Phase behavior of colloidal hard perfect tetragonal parallelepipeds. *The Journal of Chemical Physics*, 128(4):044909, 2008.

[34] Yuri Martinez-Raton, Szabolcs Varga, and Enrique Velasco. Biaxial nematic and smectic phases of parallel particles with different cross sections. *Physical Review E*, 78(3):031705, 2008.

[35] R Blaak, BM Mulder, and D Frenkel. Cubatic phase for tetrapods. *The Journal of Chemical Physics*, 120(11):5486–5492, 2004.

[36] Ran Ni, Anjan Prasad Gantapara, Joost de Graaf, Ren van Roij, and Marjolein Dijkstra. Phase diagram of colloidal hard superballs: from cubes via spheres to octahedra. *Soft Matter*, 8(34):8826–8834, 2012.

[37] Pablo F Damasceno, Michael Engel, and Sharon C Glotzer. Crystalline assemblies and densest packings of a family of truncated tetrahedra and the role of directional entropic forces. *ACS Nano*, 6(1):609–614, 2012-01.

[38] Oleg Gang and Yugang Zhang. Shaping phases by phasing shapes. *ACS Nano*, 5(11):8459–8465, 2011-11.

[39] Y Jiao, F H Stillinger, and S Torquato. Optimal packings of superdisks and the role of symmetry. *Physical Review Letters*, 100(24):245504, 2008.

[40] Carlos Avendao and Fernando A.Escobedo. Phase behavior of rounded hard-squares. *Soft Matter*, 8(17):4675–4681, 2012.

[41] Pablo F. Damasceno, Michael Engel, and Sharon C. Glotzer. Predictive self-assembly of polyhedra into complex structures. *Science*, 337(6093):453–457, 2012-07-27.

[42] Amir Haji-Akbari, Michael Engel, Aaron S. Keys, Xiaoyu Zheng, Rolfe G. Petschek, Peter Palffy-Muhoray, and Sharon C. Glotzer. Disordered, quasicrystalline and crystalline phases of densely packed tetrahedra. *Nature*, 462(7274):773–777, 2009-12.

[43] Aleksandar Donev, Ibrahim Cisse, David Sachs, Evan A. Variano, Frank H. Stillinger, Robert Connelly, Salvatore Torquato, and P. M. Chaikin. Improving the density of jammed disordered packings using ellipsoids. *Science*, 303(5660):990–993, 2004-02-13.

[44] Stefano Sacanna and David J Pine. Shape-anisotropic colloids: Building blocks for complex assemblies. *Current Opinion in Colloid & Interface Science*, 16(2):96–105, 2011-03.

[45] SC Glotzer and MJ Solomon. Anisotropy of building blocks and their assembly into complex structures. *Nature Materials*, 6(8):557–562, 2007.

[46] Bartosz A Grzybowski, Christopher E Wilmer, Jiwon Kim, Kevin P Browne, and Kyle J M Bishop. Self-assembly: from crystals to cells. *Soft Matter*, 5(6):1110, 2009.

[47] Orlin D Velev and S Gupta. Materials fabricated by micro-and nanoparticle assembly-the challenging path from science to engineering. *Advanced Materials*, 21:1–9, 2009.

[48] G M Whitesides and Bartosz A grzybowski. Self-assembly at all scales. *Science*, 295(5564):2418–2421, 2002-03.

[49] Kun Zhao, Robijn Bruinsma, and Thomas G Mason. Local chiral symmetry breaking in triatic liquid crystals. *Nature Communications*, 3:801–8, 2012-04.

[50] K Zhao, R. Bruinsma, and T G Mason. Entropic crystalcrystal transitions of brownian squares. *Proceedings of the National Academy of Sciences*, 108(7):2684–2687, 2011.

[51] Kun Zhao and Thomas G Mason. Frustrated rotator crystals and glasses of brownian pentagons. *Physical Review Letters*, 103(20):208302, 2009.

[52] L Rossi, S Sacanna, W T M Irvine, P M Chaikin, D J Pine, and A P Philipse. Cubic crystals from cubic colloids. *Soft Matter*, 7(9):4139–4142, 2011.

[53] B. de Smit and H. W. Lenstra Jr. The mathematical structure of eschers print gallery. *Notices of the American Mathematical Society*, 50(4):446–451, 2003.

[54] V. Shikin, S. Nazin, D. Heitmann, and T. Demel. Dynamic response of quantum dots. *Physical Review B*, 43(14):11903–11907, 1991-05-15.

[55] A. Koulakov and B. Shklovskii. Charging spectrum and configurations of a wigner crystal island. *Physical Review B*, 57(4):2352–2367, 1998-01.

[56] A. Mughal and M. Moore. Topological defects in the crystalline state of one-component plasmas of nonuniform density. *Physical Review E*, 76(1), 2007-07.

[57] H. Thomas, G. E. Morfill, V. Demmel, J. Goree, B. Feuerbacher, and D. Mhlmann. Plasma crystal: Coulomb crystallization in a dusty plasma. *Physical Review Letters*, 73(5):652–655, 1994-08-01.

[58] V. E. Fortov, A. V. Ivlev, S. A. Khrapak, A. G. Khrapak, and G. E. Morfill. Complex (dusty) plasmas: Current status, open issues, perspectives. *Physics Reports*, 421(1):1–103, 2005-12-01.

[59] Milton W. Cole. Electronic surface states of liquid helium. *Reviews of Modern Physics*, 46(3):451–464, 1974-07-01.

[60] R. S. Crandall and R. Williams. Crystallization of electrons on the surface of liquid helium. *Physics Letters A*, 34(7):404–405, 1971-04-19.

[61] C. C. Grimes and G. Adams. Evidence for a liquid-to-crystal phase transition in a classical, two-dimensional sheet of electrons. *Physical Review Letters*, 42(12):795–798, 1979-03-19.

[62] M. Mielenz, J. Brox, S. Kahra, G. Leschhorn, M. Albert, T. Schaetz, H. Landa, and B. Reznik. Trapping of topological-structural defects in coulomb crystals. *Physical Review Letters*, 110(13):133004, 2013-03-28.

[63] D. Ray, C. J. Olson Reichhardt, B. Jank, and C. Reichhardt. Strongly enhanced pinning of magnetic vortices in type-II superconductors by conformal crystal arrays. *Physical Review Letters*, 110(26):267001, 2013-06-24.

[64] S. Gunon, Y. J. Rosen, Ali C. Basaran, and Ivan K. Schuller. Highly effective superconducting vortex pinning in conformal crystals. *Applied Physics Letters*, 102(25):252602, 2013-06-24.

[65] C. Reichhardt, D. Ray, and C. J. Olson Reichhardt. Reversible ratchet effects for vortices in conformal pinning arrays. *Physical Review B*, 91(18):184502, 2015-05-04.

[66] F. Rothen, Piotr Pieranski, N. Rivier, and A. Joyet. Conformal crystal. *European Journal of Physics*, 14(5):227, 1993-09-01.

[67] W. Drenckhan, D. Weaire, and S. J. Cox. The demonstration of conformal maps with two-dimensional foams. *European Journal of Physics*, 25(3):429, 2004-05-14.

[68] Franois Rothen and Piotr Pieraski. Mechanical equilibrium of conformal crystals. *Physical Review E*, 53(3):2828–2842, 1996-03.

[69] Krzysztof W Wojciechowski and Jaroslaw Klos. On the minimum energy structure of soft, two-dimensional matter in a strong uniform field: 'gravity's rainbow' revisited. *Journal of Physics A: Mathematical and General*, 29(14):3963–3976, 1996-07-21.

[70] Zhenwei Yao and Monica Olvera de la Cruz. Topological defects in flat geometry: The role of density inhomogeneity. *Physical Review Letters*, 111(11):115503, 2013-09-13.

[71] Ying-Ju Lai and Lin I. Packings and defects of strongly coupled two-dimensional coulomb clusters: Numerical simulation. *Physical Review E*, 60(4):4743–4753, 1999-10-01.

[72] Minghui Kong, B. Partoens, and F. M. Peeters. Structural, dynamical and melting properties of two-dimensional clusters of complex plasmas. *New Journal of Physics*, 5(1):23, 2003.

[73] Minghui Kong, B. Partoens, A. Matulis, and F. M. Peeters. Structure and spectrum of two-dimensional clusters confined in a hard wall potential. *Physical Review E*, 69(3):036412, 2004-03-31.

[74] Mark J. Bowick and Luca Giomi. Two-dimensional matter: order, curvature and defects. *Advances in Physics*, 58(5):449–563, 2009-09-01.

[75] H. S. Seung and David R. Nelson. Defects in flexible membranes with crystalline order. *Physical Review A*, 38(2):1005–1018, 1988-07-01.

[76] A. Prez-Garrido, M. J. W. Dodgson, and M. A. Moore. Influence of dislocations in thomson's problem. *Physical Review B*, 56(7):3640–3643, 1997-08-15.

[77] Vincenzo Vitelli, J. B. Lucks, and D. R. Nelson. Crystallography on curved surfaces. *Proceedings of the National Academy of Sciences*, 103(33):12323–12328, 2006-08-15.

[78] A. R. Bausch, M. J. Bowick, A. Cacciuto, A. D. Dinsmore, M. F. Hsu, D. R. Nelson, M. G. Nikolaides, A. Travesset, and D. A. Weitz. Grain boundary scars and spherical crystallography. *Science*, 299(5613):1716–1718, 2003-03-14.

[79] Peter Lipowsky, Mark J. Bowick, Jan H. Meinke, David R. Nelson, and Andreas R. Bausch. Direct visualization of dislocation dynamics in grain-boundary scars. *Nature Materials*, 4(5):407–411, 2005-05.

[80] William T. M. Irvine, Vincenzo Vitelli, and Paul M. Chaikin. Pleats in crystals on curved surfaces. *Nature*, 468(7326):947–951, 2010-12-16.

[81] William T. M. Irvine, Mark J. Bowick, and Paul M. Chaikin. Fractionalization of interstitials in curved colloidal crystals. *Nature Materials*, 11(11):948–951, 2012-11.

[82] Amir Azadi and Gregory M. Grason. Emergent structure of multidislocation ground states in curved crystals. *Physical Review Letters*, 112(22):225502, 2014-06-04.

[83] Isaac R. Bruss and Gregory M. Grason. Non-euclidean geometry of twisted filament bundle packing. *Proceedings of the National Academy of Sciences*, 109(27):10781–10786, 2012-07-03.

[84] Gregory M. Grason. Perspective: Geometrically frustrated assemblies. *The Journal of Chemical Physics*, 145(11):110901, 2016-09-21.

[85] Yael Klein, Efi Efrati, and Eran Sharon. Shaping of elastic sheets by prescription of non-euclidean metrics. *Science*, 315(5815):1116–1120, 2007-02-23.

[86] Nakul P. Bende, Ryan C. Hayward, and Christian D. Santangelo. Nonuniform growth and topological defects in the shaping of elastic sheets. *Soft Matter*, 10(34):6382, 2014-06-24.

[87] Michael Moshe, Ido Levin, Hillel Aharoni, Raz Kupferman, and Eran Sharon. Geometry and mechanics of two-dimensional defects in amorphous materials. *Proceedings of the National Academy of Sciences*, page 201506531, 2015-08-10.

[88] Gilles Bosma, Chellapah Pathmamanoharan, Els H. A. de Hoog, Willem K. Kegel, Alfons van Blaaderen, and Henk N. W. Lekkerkerker. Preparation of monodisperse, fluorescent PMMAlatex colloids by dispersion polymerization. *Journal of Colloid and Interface Science*, 245(2):292–300, 2002-01-15.

[89] L. Antl, J. W. Goodwin, R. D. Hill, R. H. Ottewill, S. M. Owens, S. Papworth, and J. A. Waters. The preparation of poly(methyl methacrylate) latices in non-aqueous media. *Colloids and Surfaces*, 17(1):67–78, 1986-01-01.

[90] Lynn Bonsall and A. A. Maradudin. Some static and dynamical properties of a two-dimensional wigner crystal. *Physical Review B*, 15(4):1959–1973, 1977-02-15.

[91] V. D. Natsik and S. N. Smirnov. The mechanics of 2d crystals: A change from the atomic-lattice description to equations of the elasticity theory. *Low Temperature Physics*, 39(6):534–545, 2013-06-01.

[92] David R. Nelson and Tsvi Piran. *Statistical Mechanics of Membranes and Surfaces*. World Scientific, 2004.

[93] MirFaez Miri and Nicolas Rivier. Continuum elasticity with topological defects, including dislocations and extra-matter. *Journal of Physics A: Mathematical and General*, 35(7):1727, 2002-02-22.

[94] Joshua A. Anderson, Chris D. Lorenz, and A. Travesset. General purpose molecular dynamics simulations fully implemented on graphics processing units. *Journal of Computational Physics*, 227(10):5342–5359, 2008-05.

[95] Jens Glaser, Trung Dac Nguyen, Joshua A. Anderson, Pak Lui, Filippo Spiga, Jaime A. Millan, David C. Morse, and Sharon C. Glotzer. Strong scaling of general-purpose molecular dynamics simulations on GPUs. *Computer Physics Communications*, 192:97–107, 2015-07.

[96] David J. Griffiths and Ye Li. Charge density on a conducting needle. *American Journal of Physics*, 64(6):706–714, 1996-06-01.

[97] Michael M. Fogler. Electrostatics of two-dimensional structures: Exact solutions and approximate methods. *Physical Review B*, 69(24):245321, 2004-06-25.

[98] I. A. Larkin and V. B. Shikin. Diagnostics of individual quasi-one-dimensional electronic channels. *Physics Letters A*, 151(6):335–338, 1990-12-17.

[99] Vladimir M. Bedanov and Franois M. Peeters. Ordering and phase transitions of charged particles in a classical finite two-dimensional system. *Physical Review B*, 49(4):2667–2676, 1994-01-15.

[100] Y. V. Nazarov. Hierarchical wigner crystal at the edge of a quantum hall bar. *EPL (Europhysics Letters)*, 32(5):443, 1995.

[101] Monique Dubois, Bruno Dem, Thadde Gulik-Krzywicki, Jean-Claude Dedieu, Claire Vautrin, Sylvain Dsert, Emile Perez, and Thomas Zemb. Self-assembly of regular hollow icosahedra in salt-free catanionic solutions. *Nature*, 411(6838):672–675, 2001-06-07.

[102] Jack Lidmar, Leonid Mirny, and David R. Nelson. Virus shapes and buckling transitions in spherical shells. *Physical Review E*, 68(5):051910, 2003-11-25.

[103] Graziano Vernizzi and Monica Olvera de la Cruz. Faceting ionic shells into icosahedra via electrostatics. *Proceedings of the National Academy of Sciences*, 104(47):18382–18386, 2007-11-20.

[104] D. A. Bandurin, I. Torre, R. Krishna Kumar, M. Ben Shalom, A. Tomadin, A. Principi, G. H. Auton, E. Khestanova, K. S. Novoselov, I. V. Grigorieva, L. A. Ponomarenko, A. K. Geim, and M. Polini. Negative local resistance caused by viscous electron backflow in graphene. *Science*, 351(6277):1055–1058, March 2016.

[105] James E. Pringle and Andrew King. *Astrophysical Flows*. Cambridge University Press, 2007.

[106] Eleonora Secchi, Sophie Marbach, Antoine Nigus, Derek Stein, Alessandro Siria, and Lydric Bocquet. Massive radius-dependent flow slippage in carbon nanotubes. *Nature*, 537(7619):nature19315, September 2016.

[107] J.-C. Tsai, Fangfu Ye, Juan Rodriguez, J. P. Gollub, and T. C. Lubensky. A Chiral Granular Gas. *Physical Review Letters*, 94(21):214301, May 2005.

[108] Thomas Scaffidi, Nabhanila Nandi, Burkhard Schmidt, Andrew P. Mackenzie, and Joel E. Moore. Hydrodynamic Electron Flow and Hall Viscosity. *Physical Review Letters*, 118(22):226601, June 2017.

[109] Paul Wiegmann and Alexander G. Abanov. Anomalous Hydrodynamics of Two-Dimensional Vortex Fluids. *Physical Review Letters*, 113(3):034501, July 2014.

[110] Debarghya Banerjee, Anton Souslov, Alexander G. Abanov, and Vincenzo Vitelli. Odd viscosity in chiral active fluids. *Nature Communications*, 8(1):1573, November 2017.

[111] Benjamin C. van Zuiden, Jayson Paulose, William T. M. Irvine, Denis Bartolo, and Vincenzo Vitelli. Spatiotemporal order and emergent edge currents in active spinner materials. *Proceedings of the National Academy of Sciences*, 113(46):12919–12924, November 2016.

[112] S. Fürthauer, M. Strempel, S. W. Grill, and F. Jülicher. Active Chiral Processes in Thin Films. *Physical Review Letters*, 110(4):048103, January 2013.

[113] J. E. Avron, R. Seiler, and P. G. Zograf. Viscosity of Quantum Hall Fluids. *Physical Review Letters*, 75(4):697–700, July 1995.

[114] Gašper Kokot, Shibananda Das, Roland G Winkler, Gerhard Gompper, Igor S Aranson, and Alexey Snezhko. Active turbulence in a gas of self-assembled spinners. *Proceedings of the National Academy of Sciences*, 114(49):12870–12875, 2017.

[115] Alexander P. Petroff, Xiao-Lun Wu, and Albert Libchaber. Fast-Moving Bacteria Self-Organize into Active Two-Dimensional Crystals of Rotating Cells. *Physical Review Letters*, 114(15):158102, April 2015.

[116] Bartosz A. Grzybowski, Howard A. Stone, and George M. Whitesides. Dynamic self-assembly of magnetized, millimetre-sized objects rotating at a liquid-air interface. *Nature*, 405(6790):1033–1036, June 2000.

[117] Bartosz A. Grzybowski, Xingyu Jiang, Howard A. Stone, and George M. Whitesides. Dynamic, self-assembled aggregates of magnetized, millimeter-sized objects rotating at the liquid-air interface: Macroscopic, two-dimensional classical artificial atoms and molecules. *Physical Review E*, 64(1):011603, June 2001.

[118] Bartosz A. Grzybowski, Howard A. Stone, and George M. Whitesides. Dynamics of self assembly of magnetized disks rotating at the liquid-air interface. *Proceedings of the National Academy of Sciences*, 99(7):4147–4151, April 2002.

[119] Bartosz A. Grzybowski and George M. Whitesides. Dynamic Aggregation of Chiral Spinners. *Science*, 296(5568):718–721, April 2002.

[120] M. Belovs and A. Cēbers. Hydrodynamics with spin in bacterial suspensions. *Physical Review E*, 93(6):062404, June 2016.

[121] J. Yan, S. C. Bae, and S. Granick. Rotating crystals of magnetic Janus colloids. *Soft Matter*, 11(1):147–153, December 2014.

[122] Yan Jing, Bae Sung Chul, and Granick Steve. Colloidal Superstructures Programmed into Magnetic Janus Particles. *Advanced Materials*, 27(5):874–879, February 2015.

[123] Ronald E Rosensweig. *Ferrohydrodynamics*. Courier Corporation, 2013.

[124] I Torres-Díaz and C Rinaldi. Recent progress in ferrofluids research: novel applications of magnetically controllable and tunable fluids. *Soft matter*, 10(43):8584–8602, 2014.

[125] Christian Scholz, Michael Engel, and Thorsten Pöschel. Rotating robots move collectively and self-organize. *Nature Communications*, 9(1):931, March 2018.

[126] J.-C. Bacri, R. Perzynski, M. I. Shliomis, and G. I. Burde. "Negative-Viscosity" effect in a magnetic fluid. *Phys. Rev. Lett.*, 75:2128–2131, Sep 1995.

[127] Eric Climent, Kyongmin Yeo, Martin R. Maxey, and George E. Karniadakis. Dynamic Self-Assembly of Spinning Particles. *Journal of Fluids Engineering*, 129(4):379–387, October 2006.

[128] Tadao Sugimoto, Kazuo Sakata, and Atsushi Muramatsu. Formation Mechanism of Monodisperse Pseudocubic $\alpha - Fe_2O_3$ Particles from Condensed Ferric Hydroxide Gel. *Journal of Colloid and Interface Science*, 159(2):372–382, September 1993.

[129] Laura Rossi. *Colloidal superballs*. Utrecht University, 2012. OCLC: 6893354969.

[130] Allan, Daniel and, Caswell, Thomas and, Keim, Nathan and, and van der Wel, Casper. trackpy v0.3.2, 2016.

[131] J. S. Dahler and L. E. Scriven. Theory of Structured Continua. I. General Consideration of Angular Momentum and Polarization. *Proceedings of the Royal Society of London A: Mathematical, Physical and Engineering Sciences*, 275(1363):504–527, October 1963.

[132] S. C. Cowin. Polar Fluids. *The Physics of Fluids*, 11(9):1919–1927, September 1968.

[133] Howard Brenner and Ali Nadim. The Lorentz reciprocal theorem for micropolar fluids. *Journal of Engineering Mathematics*, 30(1-2):169–176, March 1996.

[134] J. E. Avron. Odd Viscosity. *Journal of Statistical Physics*, 92(3-4):543–557, August 1998.

[135] Douwe Jan Bonthuis, Dominik Horinek, Lydric Bocquet, and Roland R. Netz. Electrohydraulic Power Conversion in Planar Nanochannels. *Physical Review Letters*, 103(14):144503, October 2009.

[136] S. Radin. Lorentz Plasma in a Strong Magnetic Field. *The Physics of Fluids*, 15(1):91–95, January 1972.

[137] B. B Robinson and I. B Bernstein. A variational description of transport phenomena in a plasma. *Annals of Physics*, 18(1):110–169, April 1962.

[138] L. P. Pitaevskii and E. M. Lifshitz. *Physical Kinetics*. Butterworth-Heinemann, Oxford, UK, 1981.

[139] J.-C. Bacri, A. O. Cebers, and R. Perzynski. Behavior of a magnetic fluid microdrop in a rotating magnetic field. *Phys. Rev. Lett.*, 72:2705–2708, Apr 1994.

[140] N. Read. Non-Abelian adiabatic statistics and Hall viscosity in quantum Hall states and $p_x + ip_y$ paired superfluids. *Physical Review B*, 79(4):045308, 2009.

[141] Jens Eggers. Nonlinear dynamics and breakup of free-surface flows. *Reviews of Modern Physics*, 69(3):865–930, July 1997.

[142] M. C. A Kropinski. An Efficient Numerical Method for Studying Interfacial Motion in Two-Dimensional Creeping Flows. *Journal of Computational Physics*, 171(2):479–508, August 2001.